DISCLAIMER

Final Scientific/Technical Report

Durable High Power Density Fuel Cell Cathodes for Heavy-Duty Vehicles

October 6, 2024

Federal Agency	U.S. Department of Energy Hydrogen and Fuel Cells Technologies Office
Award Number	DE-EE0008822
Prime Recipient	Carnegie Mellon University
Principal Investigator and Contact Information	Shawn Litster Phone: 412-268-3050 E-mail: litster@andrew.cmu.edu
Working Partners	Ballard Power Systems, Inc., Chemours Company, M2FCT Consortium
Period Covered by the Report	October 1st, 2019 – March 31st, 2024

Disclaimer

Acknowledgments

This material is based upon work supported by the Department of Energy, Office of Energy Efficiency and Renewable Energy (EERE), under Award Number DE-EE0008822.

The project team would like first to thank the U.S. Department of Energy and Hydrogen and Fuel Cell Technologies Office for the funding and support of this project. The team is grateful for the guidance and support of the project's Technology Manager, Greg Kleen. His thoughtfulness, careful reviews, and timely assistance eased the project management and helpful directions throughout the course of the project. Finally, we'd like to thank Sunita Satyapal and Dimitrios Papageorgopoulos for their leadership of the Hydrogen and Fuel Cell Technologies Office and the Fuel Cells program.

The team also extends its thanks to the Million Mile Fuel Cell Truck (M2FCT) consortium members and the other project teams for an engaging research and development effort. Throughout the project, there were many valuable M2FCT program meetings amongst a community of engaged researchers from industry, national laboratories, and universities, working to fuel cells for heavy duty transportation. Many valuable discussions amongst the program members contributed to the advances made. The team would also like to thank reviewers from the Annual Merit Review for their suggestions and comments as well as the feedback from the DOE Fuel Cell Tech Team for their valued review and comments.

The nano-CT instrument at Carnegie Mellon University was acquired with the support of a Major Research Infrastructure (MRI) award from the National Science Foundation under Grant No. 1229090.

Portions of the electron microscopy were conducted at the Center for Nanophase Materials Sciences, which is a DOE Office of Science User Facility. X-ray scattering measurements were performed at the Advanced Photon Source, a US DOE Office of Science User Facility operated for the US DOE by Argonne National Laboratory, which is operated for the US DOE by the University of Chicago Argonne LLC under contract no. DE-AC02-06CH11357. The operation of MRCAT is supported both by DOE and the MRCAT member institutions.

Executive Summary

The aim of this project was to advance the performance and durability of proton exchange membrane fuel cells (PEMFCs) for their use in the electrification of heavy-duty vehicles (HDVs). With an emphasis on total cost of ownership for HDVs, the development of the fuel cells focuses more heavily on the efficiency and lifetime (i.e., durability) than past focus on platinum group metal (PGM) costs and power density. This project takes a unique approach to achieving these goals – using next-generation polymer electrolytes in the electrodes that yield significant improvements in performance and dramatic reductions in degradation rates.

A key outcome of the project was an ionomer/catalyst combination of a Pt catalyst on a low surface area carbon support (Pt/LSC) with a high oxygen permeability ionomer (HOPI) that met both the project's performance target (current at 0.8 V, >0.3 A/cm^2) and durability target (voltage loss at 0.8 A/cm^2, <30 mV) with the goal of projected a >4X increase in life-time.

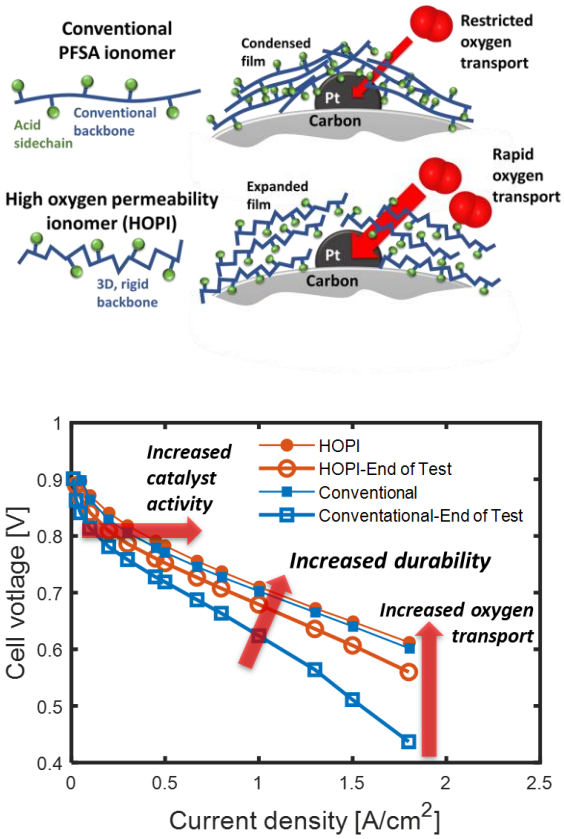

Figure 1: HOPI produces an ionomer-film that prevents compaction of a condensed film on the catalyst surface, increasing the oxygen content in the film and improving it's oxygen transport. Fuel cell testing before and after durability testing show both increased performance and durability.

The approach investigated in this project is the use of electrode-specific ionomers that are designed to mitigate the negative impacts of conventional perfluorosulfonic acid (PFSA) ionomers. Conventional PFSA ionomers have been shown to cause significant voltage losses due to the high oxygen transport resistance through the condensed films of ionomer at the catalyst surface (see Figure 1). Conventional PFSA ionomers with a long side chain chemistry also reduce efficiency due to the partial adsorption of the ionomer's anion onto the catalyst, that effectively reduces the surface activity of the catalyst. In this project, HOPI has been synthesized and optimized for cathode integration. Distinct features of this HOPI is a more rigid, 3D polymer backbone to reduce the collapse of the ionomer film on the catalyst. Furthermore, the 3D rigid backbone is combined with a short side chain chemistry for reduced anion adsorption.

The project had four primary tasks to meet these objectives. ***Task 1*** focused on the synthesis and characterization of the HOPI variants. A component of this task was scaling up the synthesis such that HOPI could be provided in large quantities to project partners and laboratories in the Million Mile Fuel Cell Truck (M3FCT) consortium ***Task 2*** revolved

around optimizing the catalyst/electrolyte interface. This was achieved through parametric studies of a wide range of electrode preparation studies as well as molecular dynamics simulation of the ionomer/catalyst interface. The fuel cell testing showed that HOPI yielded >60% in specific activity of the catalyst when properly integrated in addition to the expected reduction in mass transport losses arising from a 3X increase in oxygen permeability. ***Task 3*** focused on fabrication of HOPI-enhanced cathode using scale-able methods that can be easily translated to commercialization. This task was supported by studies on improving the electrode film coating quality, with an emphasis on reducing the degree of cracking. ***Task 4*** focused on the durability testing and lifetime estimation. This was achieved through accelerated stress tests (ASTs) for both Pt dissolution and startup/shutdown (SUSD) carbon corrosion. Using the AST results and performance models, the impact of the of the HOPI on lifetime was evaluated.

Key outcomes and findings of the project were:

- Three variants of HOPI chemistry (A, B, and C) were synthesized with variations in equivalent weight (EW) ranging from 780-1040 EW.
- HOPI synthesis was scaled up over 20X over the project to 8 L batches of dispersions
- Thin-film characterizations done in collaboration with Lawrence Berkeley National Laboratory showed that 1)HOPI was much more dimensionally stable than the conventional PFSA ionomer, with significantly less densification at low relative humidity (water content) and 2) HOPI exhibited less phase segregation when hydrated.
- Permeability measurements of HOPI films supported by a nanoporous substrate show that the ~3X increase in permeability is a bulk property and not only an interfacial phenomenon.
- Permeability measurements of HOPI membranes over a range of relative humidity show that HOPI's relative increase in permeability is greater at low relative humidity/drier conditions.
- Molecular dynamics (MD) simulations showed that backbone polymer of HOPI yielded a more amorphous, expanded ionomer layer with a lower density.
- The MD simulations showed that the increased permeability measured in the project is due primarily to the higher solubility of the HOPI versus PFSA.
- After optimizing the catalyst ink for the baseline PFSA ionomer and HOPI, it was found that cathodes with HOPIs exhibited significant higher currents at high voltages due to a higher effective specific activity due to the high oxygen solubility (confirmed by MEA modeling). The same cathodes also exhibited large reductions in the oxygen transport resistance, particularly at low relative humidity.
- Durability testing showed that HOPI also dramatically reduced degradation rate. The reason for the improved durability with HOPI relates to the higher specific activity of the ionomer/catalyst interface and reduced oxygen transport resistance. As the catalyst degrades and loses surfaces area, it is able to more effectively generate current due to improved area-specific performance across the polarization curve.
- Testing with different catalysts showed the different levels of impact that HOPI has depending on the carbon support. Catalyst with a low surface area support

(Pt/LSC) and a large amount of external catalyst in contact with ionomer shows the greatest impact. In contrast, Pt with a high surface area support has a significant amount of internal catalyst not in contact with ionomer and thus HOPI has much less impact on the specific activity of the Pt catalyst.

- The performance and durability benefits of HOPI are largest at low relative humidity conditions, which could be consistent with adverse and high power density operations (e.g., sustained high gradient driving at elevated ambient temperature).
- HOPI-based cathodes are susceptible to high levels of electrode cracking. The cracking can be reduced by coating electrodes in low relative humidity environments, with a low solids content ink with the highest allowable alcohol content in the ink.
- HOPI can be blended with PFSA to substantially reduce cracking while maintaining some of the HOPI benefits for activity and oxygen transport.
- Lifetime projections using models informed by experimental testing of performance and the AST were performed. For Pt/LSC, the estimated increase in lifetime with HOPI was 7X and for Pt/HSC, the estimated increase was 4X.

Table of Contents

1 Project Overview

1.1 Project Objective

The objective of the project is to facilitate low platinum loadings in an advanced fuel cell membrane electrode assembly (MEA) cathode catalyst layer (CCL) for heavy-duty vehicles (HDVs). This goal will be achieved via synthesis and implementation of a custom-designed ionomer where bulky backbone subunits and/or branched charged monomers permit enhanced oxygen transport to the platinum surface.

1.2 Background:

Our development of a durable, high power density cathode involves three main aspects: 1) Adopting precommercial high O2 permeability ionomers (HOPIs) from Chemours, 2) Developing an integrated strategy for combining these ionomers with catalyst, and 3) Establishing scale-able fabrication strategies for HDV electrodes with these ionomers that overcome the challenges associated with HDV electrodes. These approaches will be supported by HDV-specific accelerated stress tests (ASTs), advanced characterization and imaging, and multi-scale performance and durability modeling.

Our approach scales from the monomers used to synthesize HOPIs to scale-able fabrication methods for the commercialization of MEAs with HOPI-enhanced cathodes. Leveraging the unique talents and world-leading experience/capabilities of the project partners, we can pursue this effort through a combination of fluoropolymer synthesis, ionomer thin-film characterization, colloidal science and analytical methods for inks, molecular simulation, ultra-high resolution 3D imaging, multi-scale simulation, commercial-grade MEA fabrication, advanced performance, and durability diagnostics, and fuel cell lifetime forecasting models.

1.3 Approach

There are four 4 research tasks (Tasks 1 - 4) in addition to project management (Task 0):

Task 1: Ionomer development and synthesis

In this task, high oxygen permeability ionomers (HOPIs) for cathode catalyst layers were polymerized using bulky backbone subunits and short side chain sulfonic acid groups. HOPIs were synthesized to support the overall ionomer effort toward facile oxygen, proton, and water transport. Ionomers were chemically stabilized and dispersed into water/alcohol mixtures, then characterized for relevant properties and simulations of the ionomer in dispersion will be performed. The task's objective was to synthesize a high conductivity ionomer capable of (1) reducing local oxygen transport resistance and ionomer-based anion poisoning and (2) enabling higher catalyst activity and higher stack temperatures for high efficiency when used at the cathode in an MEA.

Task 1 Project Outcome: A wide variety of HOPI chemistries (A, B, and C) with a wide range of equivalent weights were synthesized, characterized, simulated and evaluated in fuel cells for performance and durability.

Task 2: Engineering the catalyst/ionomer interface

In this task the nano- and micro-scale interface of the HOPI and the catalyst and carbon support was optimized for performance and durability. The task addressed the simultaneous challenges of reducing the ionomer anion poisoning of catalyst and the local O2 resistance of the interface. The task will provide a fundamental understanding of the ink processing parameters that yield high performance and durability.

Task 2 Project Outcome: The catalyst ionomer interface was optimized through integrated synthesis and testing, including optimization of catalyst ink solvents, I/C ratios, and catalysts. Molecular dynamics simulations of the catalyst/ionomer provided an understanding of how additional oxygen uptake in the ionomer increased catalyst activity and improved oxygen transport when using HOPI versus traditional PFSA.

Task 3: Scale-able fabrication and testing of MEAs with HOPI-enhanced cathodes

This task focused on fabrication and evaluation of high performance and durable MEA design with HOPI materials in each budget period for enhancing oxygen transport. HOPIs will be integrated with Pt and/or PtCo catalyst utilizing advanced ink processing and electrode/MEA fabrication.

Task 3 Project Outcome: After optimization at the small 5 cm^2 scale in Task 2, a wide range of HOPI was evaluated using scale-able manufacturing approaches by the team's industrial MEA manufacturer with larger format MEAs (~50 cm^2). The result demonstrated significant increases in catalyst activity and reduced oxygen transport resistance in the scaled MEA. Approaches were developed to reduce electrode cracking when scaling up MEAs with HOPI with optimized inks.

Task BP.4: Durability of HOPI-enhanced cathodes for HDVs

This task focuses on assessing the durability of HOPI-enhanced cathodes and evaluating their suitability to HDVs. Accelerated stress tests (ASTs) will be refined and models will be used to forecast performance out to 25,000 h.

Task 4 Project Outcome: Both Pt dissolution and startup-shutdown (SUSD) ASTs were applied to fuel cell having the scaled-up HOPI cathodes. The ASTs showed significant reductions in the degradation rate with HOPI, attributed to the higher catalyst specific activity and improved local oxygen transport. Performance models combined with the AST characterizations were used for evaluating the impact of HOPI on fuel cell lifetime. The results on evaluating the impact of cathode degradation showed a >4X increase in lifetime.

1.4 Team Members and Roles

Carnegie Mellon University (CMU) [university prime award]

Shawn Litster (PI), Gerald Wang, Zachary Ulissi

Role: Electrode design, hydrophobicity treatments, electrode fabrication, fuel cell testing, X-ray imaging, multi-scale modeling, DFT/molecular dynamics modeling, project management.

The Chemours Company [industry sub-award]

Scott Blackburn (PI), Andrew Park, Austin Plymill

Role: Ionomer synthesis, characterization, and ionomer film characterization

Ballard Power Systems

Devproshad Paul (PI), Alan Young, Shanna Knights

Role: CCM fabrication, fuel cell performance and durability testing, lifetime modeling

1.5 Collaborations

Lawrence Berkeley National Laboratory (M2FCT consortium-funded collaboration)

Ahmet Kusoglu, Ashley Bird

Role: Ionomer thin film characterization, GISAXS

Argonne National Laboratory (M2FCT consortium-funded collaboration)

Debbie Myers, Nancy Kariuki, Jae Park

Role: X-ray scattering

Oak Ridge National Laboratory (M2FCT consortium-funded collaboration)

David Cullen,

Role: Electron microscopy

National Renewable Energy Laboratory (M2FCconsortium-funded collaboration)

KC Neyerlin

Role: Electrode development support

1.6 Accomplishments

Through the course of the project, it was demonstrated that HOPI yields significant improvements in performance and durability over the conventional Nafion D2020 PFSA ionomer. Table 1 lists the key figures of merit for the cathodes and the corresponding project targets for the base line D2020 material along with several variants of HOPI chemistry (A, B, and C) with variations in equivalent weight (EW). The results are listed for two types of catalysts; durable Pt on low surface area carbon (Pt/LSC) and high activity Pt on high surface area carbon (Pt/HSC). These were results were evaluated on the scaled-up MEAs evaluated at Ballard Power Systems.

In terms of a cathode with durability being the highest priority, the Pt/LSC cathode HOPI A 870 EW proved most encouraging. The performance of 0.41 A/cm^2 at 0.8 V exceeded the project goal of >0.3 A/cm^2. In comparison, the D2020 baseline yielded 0.33 A/cm^2. This combination of catalyst and ionomer was also the one the exceeded the <30 mV performance loss at 0.8 A/cm2, with just 29 mV loss. In comparison, the loss with D2020 was ~2X at 62 mV. This is a substantial reduction in the degradation rate that is supported by the modeling in the project. It is attributable to the high catalyst specific activity and oxygen transport that enables high performance even with significant losses in catalyst surface area. The one metric where the HOPI-enhance Pt/LSC did not meet the project target was the mass activity, although that is secondary to performance at 0.8 V.

In terms of high performance at BOL, the HOPI enhanced cathodes with Pt/HSC far exceeded the mass activity target with a significant increase over the D2020 PFSA baseline. For the Pt/HSC catalyst, using HOPI significantly reduced the degradation rate versus the D2020 PFSA baseline and reduced the performance loss at 0.8 A/cm2. However, the improvement did not achieve the project target. Table 2 list

Table 1: Performance and durability targets and status.

	DOE/Project Target	D2020 Baseline		HOPI A 788EW	HOPI A 870EW		HOPI B 850EW	HOPI B 876EW
		Pt/LSC	Pt/HSC	Pt/HSC	Pt/LSC	Pt/HSC	Pt/HSC	Pt/HSC
Mass activity (A/mg_{Pt})[1]	>0.44	0.16	0.30	0.46	0.23	0.48	0.45	0.45
Performance at 0.8V(A/cm^2)[2]	0.3	0.33	0.55	0.58	0.41	0.58	0.51	0.54
Performance loss at 0.8A/cm^2 (mV)[2,3,5]	<30	62	78	112	29	53	53	43
Local RO_2 (s/cm)[4]	9	16	21	-	9	4	8	-
CCL Resistance ($mOhm.cm^2$)[1,5]	N/A	110	103	51	100	93	84	98
Degradation rate (µV/cycle)[3,5]	N/A	2.1	2.3	2.5	0.8	1.3	1.5	1.5

Milestone or Go/No-Go	Milestone Description (Go/No-Go Decision Criteria)	Milestone Verification Process (What, How, Who, Where)
M1.1	Delivery of >200 mL (>10% solids) HOPI dispersion to project partners for thin-film characterization, ink studies, and MEA development	350 ml of HOPI delivered to project partners this quarter.
M1.2	Define ink processing protocol with concept level ink mixing/coating equipment for 0.05-0.20 mgPt/cm^2 cathode catalyst coated membranes (CCM).	Baseline D2020 protocol for 0.05-0.3 mg$_{Pt}$/cm^2 defined in this report
M1.3	Define baseline PFSA ionomer (D2020) capability with 0.20 mgPt/cm^2 Pt or PtCo catalyst, optimized for ionomer loading. Output will be a metrics table with full analysis of CCL transport properties.	Baseline D2020 MEA testing has been completed at Ballard and CMU.
M1.4	Selection of two HOPI dispersions for 50 cm^2 MEA fabrication and testing based on Task 1.1 and 1.2 findings	Completed and reported here.
GNG 1	Demonstrate >50% reduction of in-situ local oxygen transport resistance using HOPI versus baseline PFSA (D2020) with no increase in cathode protonic sheet resistance.	Target of 9 s/cm local O2 resistance has been met.
M2.1	Synthesis of improved HOPI scaled-up to 100 g to support expanded MEA testing	1 L (169 g) of ionomer delivered to Ballard
M2.2	Durability analysis comparing MEAs with HOPIs versus baseline Nafion D2020 for Pt and PtCo. Final output will be a report including failure mode analysis.	Durability has been evaluated for high and low activity Pt/C catalysts through Pt diss. AST. Failure mode imaging analysis is in process.
M2.3	Demonstrate single cell with HOPI-enhanced cathode with 0.2 mg Pt/cm^2 having a mass activity of 0.44 mA/mg PGM at 0.9 $V_{IR\text{-}free}$	0.48 A/mg achieved with HOPI and Pt/HSC
M2.4	Define ASTs for input into forecasting performance at 25,000 h using durability models	ASTs and results reported for Pt/LSAC and Pt/HSC
GNG 2	Demonstrate a 2X increase in forecasted lifetime hours using HOPI versus a baseline using D2020 Nafion under identical test conditions with 0.2 mg Pt/cm2 loading. The lifetimes of the HOPI and baseline D2020 cases will be defined as time until the power density at 0.7 V decreases to that when the baseline D2020 Nafion electrode had decreased by 10% and will be evaluated by AST characterization and forecasted durability modeling.	>2X lifetime enhancement with HOPI forecasted for both Pt/LSC and Pt/HSC reported.
M3.1	Synthesis of optimized HOPI scaled-up to 100 g to support expanded MEA testing	Large batches of HOPI being synthesized for MEA testing and shared with M2FCT consortium members.
M3.2	Selection of optimum operating point for performance and durability from analysis of operating temperature and pressure	Forecasting results indicate a 4X lifetime improvement with HOPI vs. D2020 for Pt/HSC with BOL 0.48 mA/mg PGM at 0.9 $V_{IR\text{-}free}$ with 0.2 mg Pt/cm^2 loading
M3.3	Demonstrate 4X increase in forecasted lifetime hours until 10% loss in maximum power density with an MEA having a mass activity of >0.44 mA/mg PGM at 0.9 $V_{IR\text{-}free}$ with 0.2 mg Pt/cm^2 loading using HOPI over baseline MEA with D2020 Nafion under identical test conditions.	Achieved with Pt/HSC and HOPI A 870 EW in combination with Ballard lifetime prediction model for an aggressive drive cycle.
M3.4	Fabrication and Delivery of >6 50 cm^2 MEAs with HOPI-enhanced cathodes in the HDV optimized configuration to DOE.	CCMs prepared for delivery.

2 Ionomer Synthesis (Task 1)

The ionomer synthesis for this project was performed by Chemours. The Chemours Company, formerly a part of DuPont, is the world's largest manufacturer of perfluorinated polymers with the biggest and most diverse supply chain of perfluorinated monomers. Over the past several decades, Chemours has leveraged this foundation to cultivate unmatched synthetic experience in perfluorinated chemistry and engineer pioneering products such as the world's first perfluorosulfonic acid (PFSA), Nafion™. Nafion™ has long been the benchmark material for PFSA proton exchange membranes (PEM) and ionomers in electrochemical devices, including their application as proton conductors in fuel cell cathode catalyst layers (CCL).

Recently, it has become apparent that further development of cathode-specific ionomers is required to minimize platinum catalyst loadings. Advanced PEM fuel cells manifest voltage losses (overpotentials) at high current density operation, which are associated with mass transport in the cathode. Around half of these voltage losses are attributed to local oxygen transport resistances at the platinum catalyst surface. New limiting current diagnostic tests have quantified the oxygen transport resistance and demonstrated that it is predominantly caused by traditional PFSA ionomers typically employed in the CCL. Recent studies have elucidated that thin film (<25 nm) PFSA ionomers in the CCL lose their typical phase separation and pack together in oxygen-blocking domains at the platinum-ionomer interface. A novel ionomer morphology is therefore likely required to disrupt the tight chain packing and improve oxygen transport to the catalyst surface.

The strategy for the HOPI in this project is to replace the typical ionomer backbone with a rigid, more three-dimensional backbone. First, a sterically bulky cyclic monomer that inherently resists CF_2 chain packing is included in the backbone. As example, backbone subunit for this work is perfluoro(2,2-dimethyl -1,3-dioxole) (PDD), shown in Figure 1. PDD comprises a 5-member ring with two methyl groups protruding both in and out of plane, giving PDD a unique combination of rigid x, y, and z-axis penetration. The inflexible ring structure prohibits the chain packing observed with traditional PFSAs by disrupting the crystallinity observed with tetrafluoroethylene (TFE) backbones in all current PFSA chemistries. Also, a perfluoro backbone containing PDD is more rigid, resisting the conformation where sulfonic acid moieties adsorb to the platinum surface. PDD is already part of Chemours' supply chain for its Teflon™ AF product.

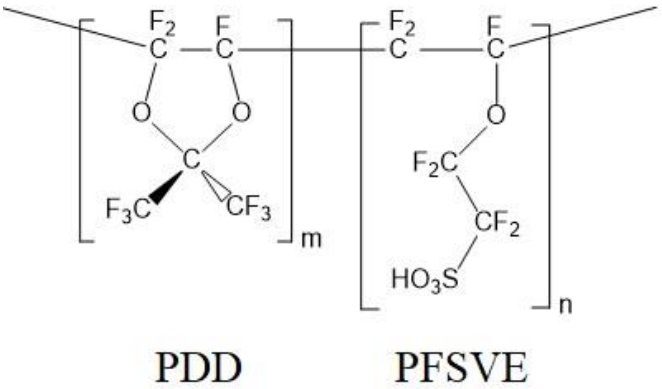

Figure 1. Example of HOPI chemistry used in this project.

Chemours' synthesis activities during the project included:

1. Optimizing the Chem-stable treatment of HOPI polymers
2. Researching alternative chemistries for improved thermal resistance during dispersion/MEA manufacturing
3. Exploring alternative chemistries for HOPI (HOPI A, HOPI B, HOPI C)
4. Synthesizing HOPIs of varying EW for cathode optimization
5. Scaling-up HOPI synthesis for distribution amongst collaborators, including the national laboratory members of the M2FCT consortium

The Chem-stable treatment is a proprietary process by which any reactive end groups in the polymer are converted to chemically inert moieties. Chem-stable Nafion™ PFSA polymers have been shown to be far more stable in membrane application and are expected to similarly manifest in improved durability in the electrode.

Chemours assembled a dedicated ~~continuous~~ reactor for HOPI polymerization (see Figure 2) that enables quicker synthesis with consistent polymer output. The monitored monomer ratio enables semi-continuous or batch polymerizations. Significant amounts of HOPI can be prepared with the reactor. The synthesis has included other proprietary processes that are included to best represent commercial polymerization while at the lab-scale. As shown in Figure 2, a new polymerization process scheme (Process B) results in ~6x faster polymerization times versus previous process (Process A). In addition, as evidenced by the absorbance data in Figure 3, the new Chemstable processing method has eliminated end groups that deteriorate the ionomer over time. Monomer composition is maintained within a tighter window for a narrower polymer EW dispersity and the ability to modify or reproducibly make target HOPI compositions. Thus far, polymer batch runs have produced of quantities >100g and finished dispersions of > 1 L volume.

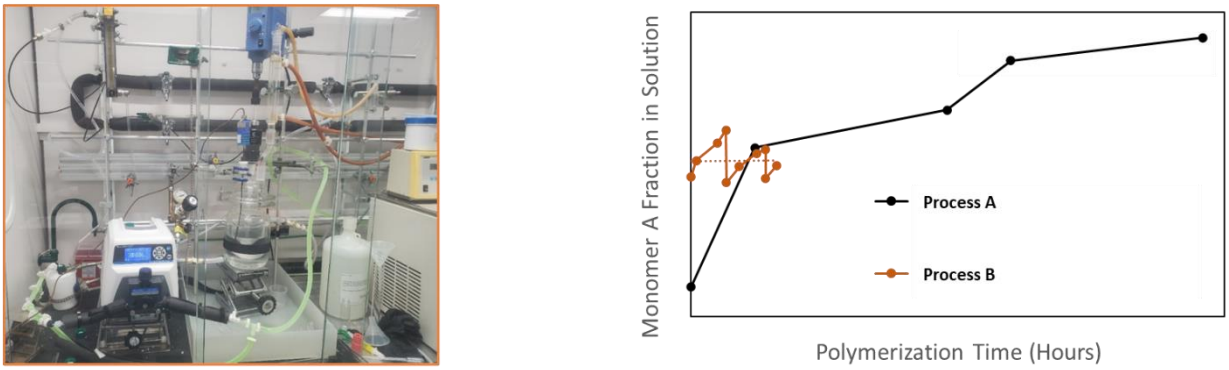

Figure 2. New modified continuous reactor for HOPI synthesis and the reduction in polymerization time with improved process.

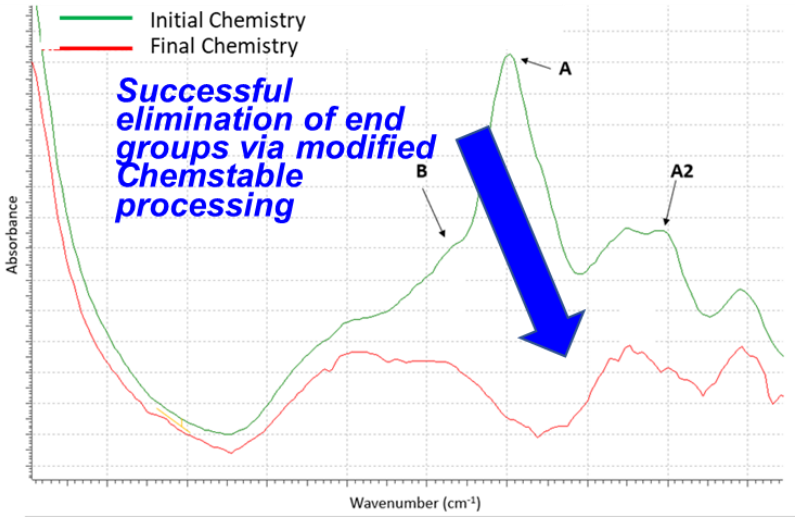

Figure 3. Absorption results showing the elimination of end groups in the Chemstable HOPI.

Chemours synthesized several new variants of HOPI, including a study on the variation of EW and an alternative chemistries (e.g., HOPI B vs. HOPI A). Figure 4 shows that both HOPI A and HOPI B were stable in solution, but HOPI B may tend to agglomerate more than HOPI A due to the lower zeta potential.

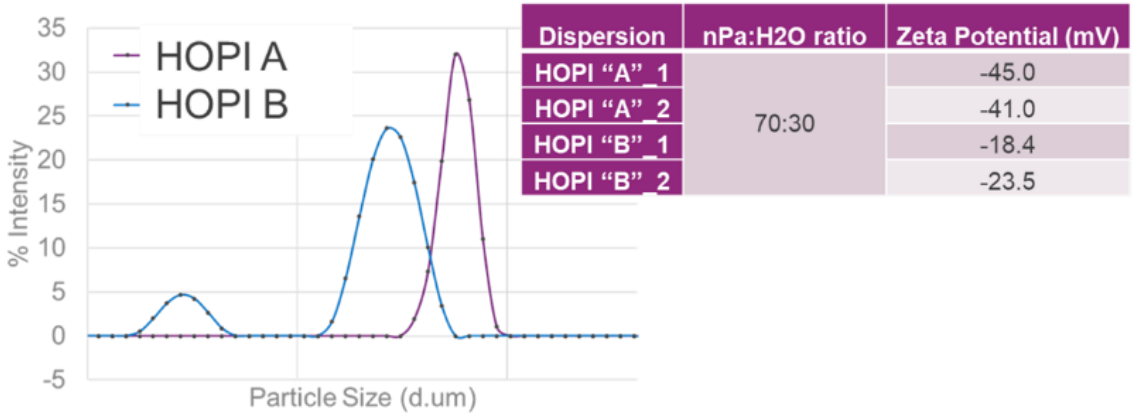

Dispersion	nPa:H2O ratio	Zeta Potential (mV)
HOPI "A"_1	70:30	-45.0
HOPI "A"_2		-41.0
HOPI "B"_1		-18.4
HOPI "B"_2		-23.5

Figure 4. Colloidal properties of HOPI A & B variants.

Chemours has synthesizeed a wide range new candidate HOPIs for this project, as described in Table 1 below. The key variants in the HOPI synthesis were the chemistry (e.g, HOPI A vs. HOPI B) and the EW.

Table 1. HOPIs produced in this project.

HOPI dispersions	Ionomer mass (g)	Chemistry	EW	Chem. Stable?	% solids	nPA:H2O	Viscosity (cp)

NDP 5001.003		HOPI A	837	No	10.3%	84:16	10.8
NDP 5006.001		HOPI A	872	Yes	10.2%	77:23	115
NDP 5006.004		HOPI A	856	Yes	10.2%	75:25	115
NDP 8004.001		HOPI B	1036	Yes	10.0%	75:25	7.9
NDP 8005.001		HOPI B	959	Yes	10.0%	75:25	9.2
NDP 8010.001		HOPI B	851	Yes	10.1%	52:48	10.8
NDP 5050.001		HOPI C	890	Yes	10.0%	50:50	16.4

3 Ionomer Dispersion and Film Characterization (Tasks 1 & 2)

3.1 HOPI Membrane Water Uptake

Chemours investigated the water uptake of cast HOPI films. Figure 1 below shows water uptake isotherms for HOPI films (as well as a cast film of D2020 at 920 EW) as a function of relative humidity. Three temperatures are surveyed. Water uptake is described as "relative mass" where the dry membrane is defined as 100% mass. The water uptake of HOPI ionomers, in general, is comparable to D2020. Lower EW ionomers, irrespective of sulfonic acid monomer, appear to have higher water uptake (as expected based on a higher density of hydrophilic sulfonic acid sites). These values will be used to optimize/finalize the EW of candidate HOPI polymers for ideal performance in the cathode catalyst layer.

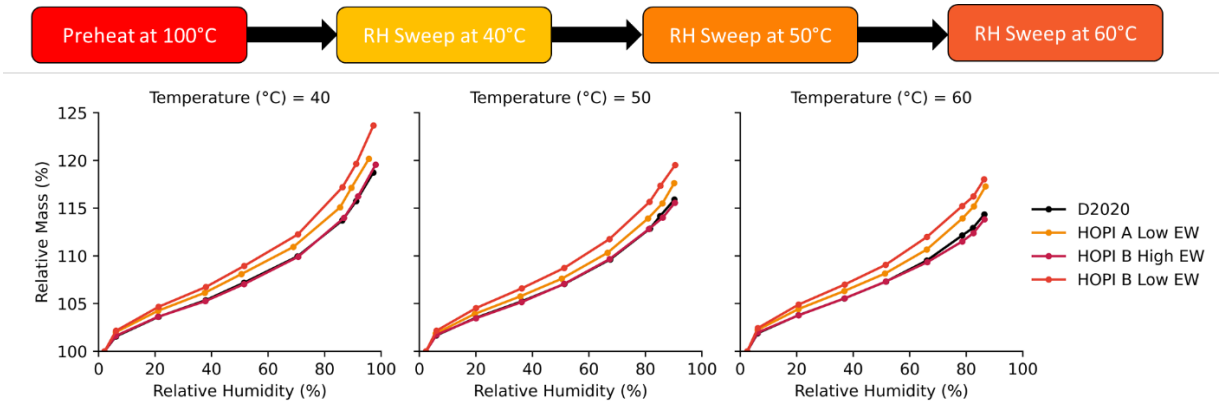

Figure 1. Water uptake of several Nafion™ baseline and HOPI films as a function temperature and relative humidity

3.2 HOPI Membrane Cracking and Burst Strength

Overall, casting HOPI from an nPa rich (nPa:H2O), 10wt% dispersion reduces crack formation in a dried film. Casting HOPI B from a nPa rich dispersion in a low, controlled relative humidity (%RH) environment significantly reduces dried film cracking. EW does not appear to play a role unless these 10wt% HOPI B dispersions are prepared in 50:50 nPa:H2O, or H2O rich environments.

A trend of crack formation with EW is tentatively observed for 50:50 nPa:H2O dispersions exclusively in HOPI B dispersions. The data suggest that 50:50 nPa:H2O or H2O rich dispersions of HOPI B should have an EW less than or around 925EW to yield a cast, dried film which lacks visual cracking. The Table 1 observations report the NDP HOPI cast dispersion only and not the catalyst ink. Table 1 reports visual observations of cracking.

Table 1. Degree of cracking as a function of HOPI B EW and solvent.

Solvent ratio nPa:H2O	HOPI B EW	
50:50	1040	Cast dispersion Film cracked
	960	
	940	
	925	
	850<x<925	Cast dispersion Unknown, not yet explored
	850	Cast dispersion Film did not crack

Solvent ratio nPa:H2O	HOPI B EW	
nPa rich, >50% nPa	1040	Film did not crack
	960	
	925	
	850	

Chemours has completed a detailed study of bulk HOPI films that are prepared by casting HOPI dispersions. Casting was done for both the HOPI A and HOPI B chemistries, both with an EW of 850. The casting done with a target thickness of 20 µm. The casting was further done with a variation of the solvent mixture with n-proponal fraction ranging from 0 to 90% as well as variation in the relative humidity from 10% to 90%. Figure 1 shows characterization of degree of cracking in the cast bulk HOPI films as a function of the HOPI chemistry, solvent composition, and relative humidity. Both HOPI A and B show a similar trend of reduced cracking with high n-proposal content and low relative humidity. These findings are consistent with previously reported studies by CMU on casting electrode films with HOPI.

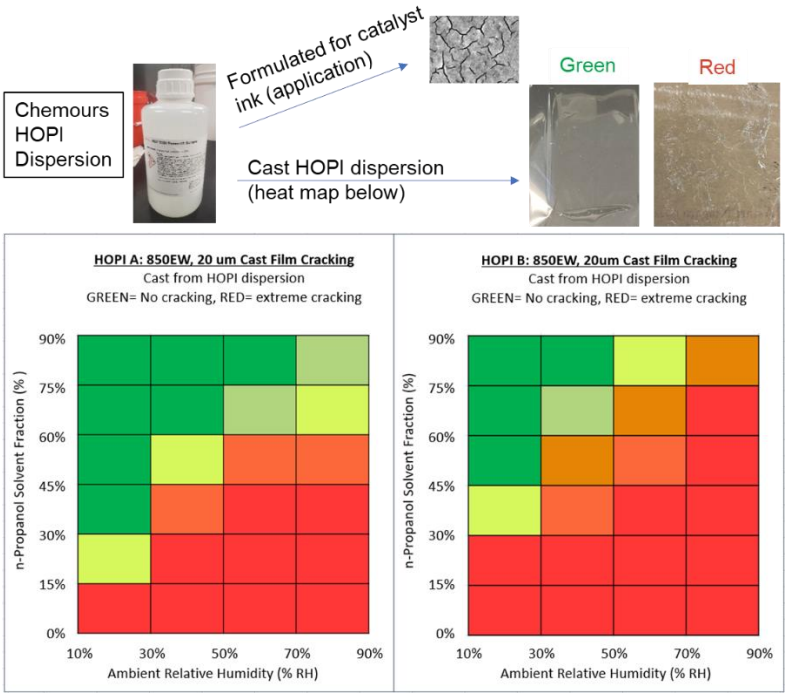

Figure 2. Results on cracking of cast films of HOPI.

The film can display cracking when cast by itself as the polymer is inherently brittle; however, this does not represent the application. In application, the catalyst ink formulation requires HOPI dispersion and catalyst. The selected catalyst and the chosen processing to prepare formulation and ultimately apply the HOPI thin film plays a crucial role in reducing or eliminating cracking. The benefit of the HOPI is the O2 permeability, which leads to higher durability and performance, which is possible due to the structure/ brittle nature of the polymer. Evaluating the various catalysts available is crucial to solving this problem.

Chemours additionally applied a burst strength test on bulk cast HOPI films (no catalyst) as well as a traditional PFSA film. The burst strength is quantified by the work (force*displacement) until the film ruptures. The results show the amorphous structure of the HOPI yields significantly lower mechanical strength. The HOPI A showed modestly higher burst strength than HOPI B.

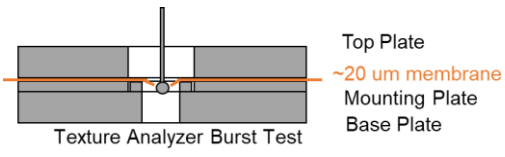

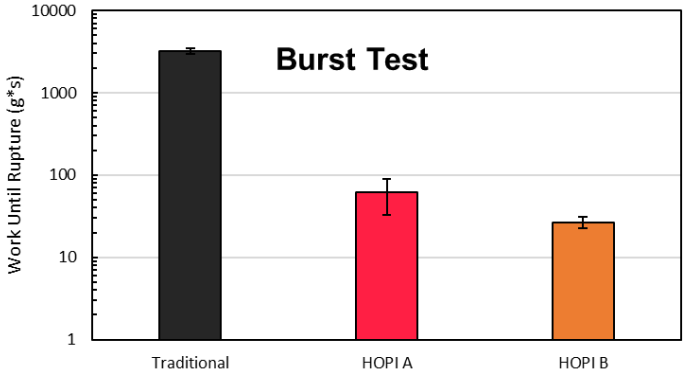

Figure 3. Burst test results for cast films of HOPI A & B versus traditional PFSA.

3.3 HOPI Membrane Permeability

In addition, oxygen permeability of bulk, dispersion cast membranes for a selection of ionomers were measured and described in Figure 4. In Figure 4a, a cartoon of the apparatus is described. Oxygen and an inert gas carrier are flowed on either side of an ionomer film of given thickness. Pressure, flow rate, and humidity of each gas is equivalent. The amount of oxygen that passes through the film at a given temperature and humidity is quantified by measuring the oxygen content in the inert gas via gas chromatograph.

Figure 4b shows the measured oxygen permeabilities for a HOPI candidate compared to traditional Nafion™ ionomers of 920 and 1000 EW. A multiplier is included to illustrate the difference between HOPI A (850 EW) and D2020 (920 EW) as a function of humidity at 80°C. The magnitude of oxygen permeability increases as humidity drops, which is consistent with previously measured data in MEA form where local oxygen transport resistance in cathode catalyst layers (CCLs) containing HOPI is more significantly improved at low RH. Further data will be taken on HOPI ionomers to describe the relationship, or lack thereof, between an ionomer's bulk film oxygen permeability and its measured local oxygen transport resistance in a CCL.

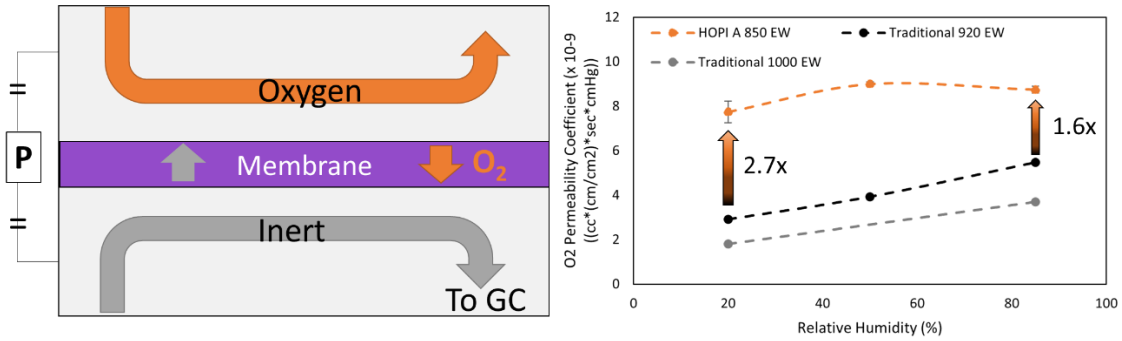

a. b.

Figure 4 a. Cartoon schematic of gas permeability cell at Chemours. b. Measured oxygen permeabilities for three films, one HOPI and two traditional Nafion™ ionomers, as a function of relative humidity at 80°C.

3.4 Oxygen Permeability Measurements

The high oxygen permeability of the ionomer in the cathode catalyst layer (CCL) of proton exchange membrane fuel cells (PEMFCs) is crucial for the efficient functioning of the fuel cell. Oxygen must be able to diffuse sufficiently to the reaction site for the fuel cell to operate optimally. In this study, we evaluate the oxygen permeability of quasi-free-standing ionomer thin films supported on a nano-porous substrate in the absence of a polarized electrode surface. The bulk film permeability of two materials, HOPI and Nafion™ D2020, was measured and reported.

3.5 Experimental

3.5.1 Ionomer Thin Film Fabrication

We used InRedox anisotropic anodic aluminum oxide (AAO) membranes (Longmont, CO), shown in Figure 5a, as nano-porous substrates to support the ionomer thin films. These AAO membranes consist of a very thin (1.5 μm) active layer and a support layer with a thickness of 60 μm, as shown in Figure 5b. The active layer contains highly uniform pores with a pore diameter of 20 nm, while the support layer has larger uniform pores with a pore diameter of 150 nm to increase the mechanical strength of the membranes [20].

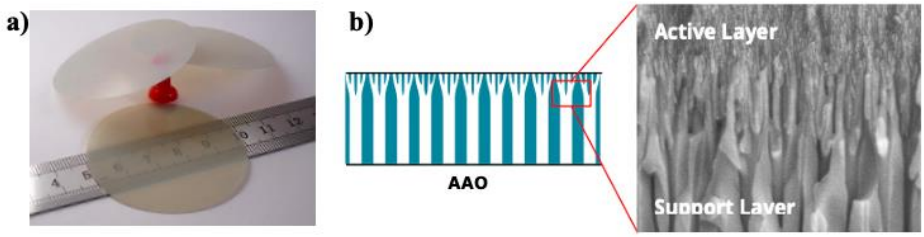

Figure 5: (a) Picture of AAO membranes, and (b) illustration of the active layer and support layer [20].

Figure 6 outlines the five-step process for fabricating ionomer thin films. We first used epoxy glue to attach the anisotropic AAO membranes onto Kapton squares with an 8 mm diameter hole in the center. We then placed the AAO-on-Kapton samples in a Yamato vacuum drying oven (Santa Clara, CA) at 80°C for 24 hours to dry the glue and evaporate any water in the AAO membranes. Next, we took the AAO-on-Kapton samples out of the oven and flipped them upside-down to keep the Kapton film side on top along with the exposed center of the AAO membranes. We then deposited the ionomer solution (Nafion™ D2020 ionomer or HOPI, diluted with DI water and n-propyl alcohol (nPA)) using a single channel pipette, drop by drop, onto the exposed area of the AAO membranes, ensuring uniform coverage. We placed the ionomer-on-AAO-on-Kapton samples back into the same vacuum oven at 80°C for an additional 24 hours to dry off the water and alcohol in the ionomer solution. We then had ionomer thin films deposited on anisotropic AAO membranes ready for testing.

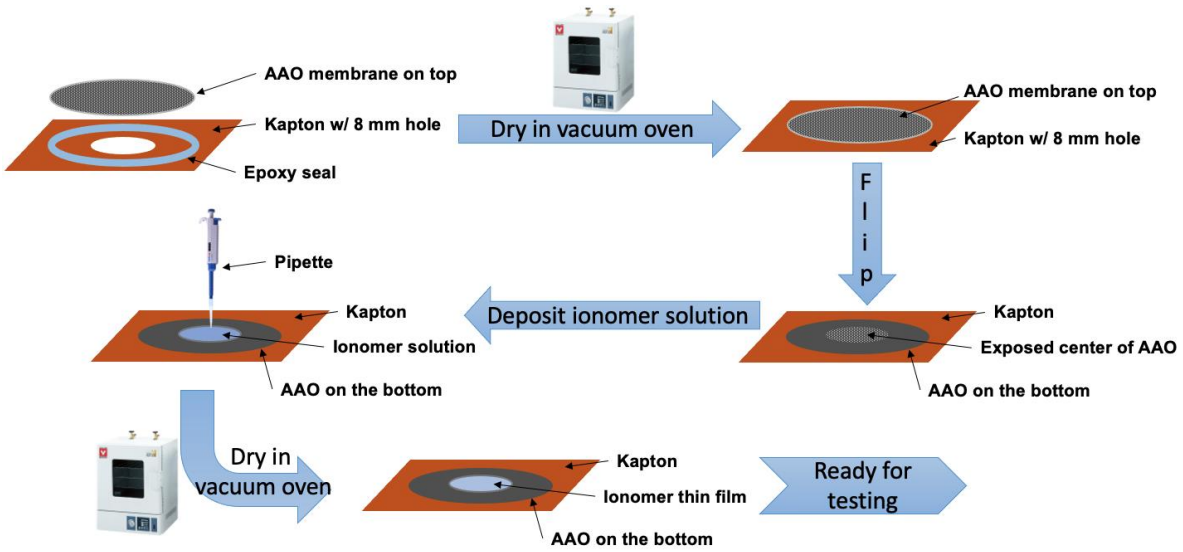

Figure 6: Illustration of the ionomer thin film fabrication process.

3.5.2 ORR Current and Oxygen Concentration Measurements

We installed an ionomer-on-AAO-on-Kapton sample in a modified Scribner dual area fuel cell fixture (Southern Pines, NC), similar to that of our prior work. As shown in Figure 7, on the cathode side of the cell, we used a modified cathode flow plate and sample holder with a freestanding, electrically isolated ionomer-on-AAO-on-Kapton sample. We integrated a PreSens oxygen sensor and temperature sensor (Regensburg, Germany) with the sample holder assembly to measure the oxygen concentration below the samples. A fuel cell MEA (4 cm^2 active area) was installed in the fuel cell fixture to function as an oxygen sink and oxygen transport rate monitor. There was no change to the anode side of the cell.

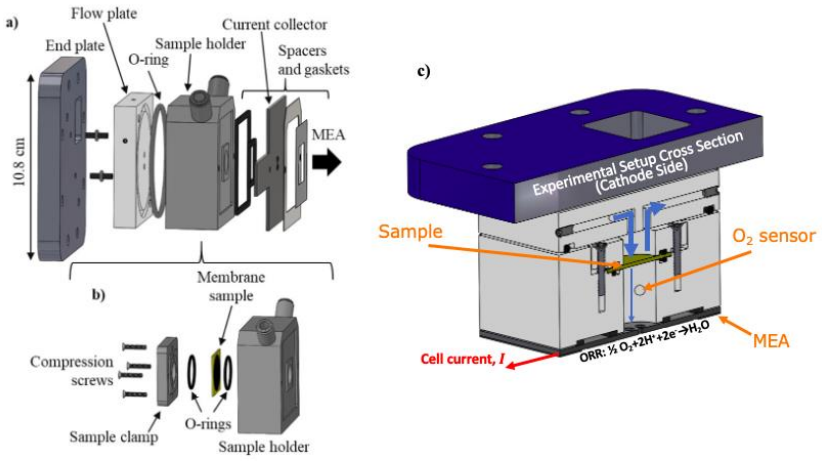

Figure 7: Schematic of (a) the cathode side of the fuel cell fixture (b) the sample holder with a freestanding membrane sample, and (c) the cross-section view of the cathode side of the cell.

We connected the fuel cell fixture to a Scribner fuel cell test stand (Southern Pines, NC), which can regulate the gas flow rate and temperature. We used a BioLogic VSP potentiostat (Seyssinet-Pariset, France) to measure the oxygen reduction current of the MEA. We first heated the ionomer-on-AAO-on-Kapton sample to 50°C while flowing un-humidified nitrogen gas through both the cathode and the anode. Once the sample reached 50°C, we increased the relative humidity (RH) of both inlets to 29%, creating a dry stable environment for the sample. At the same time, we introduced 1% hydrogen/99% nitrogen gas to the anode at 1 atm and 0.2 l/min. On the cathode side, we alternated the inlet gas between air and pure N_2 with the same pressure and flow rate as the anode inlet. We operated the MEA in the test cell under the limiting current condition with a 0.3 V hold to ensure the O_2 concentration decreased to zero at the interface of CCL and PEM in the MEA [23]. Figure 8 shows the ORR currents measured under alternating air and N_2 flows as well as the oxygen concentration measured below the ionomer-on-AAO-on-Kapton sample. We smoothed the ORR current data by using the 25-point moving average technique.

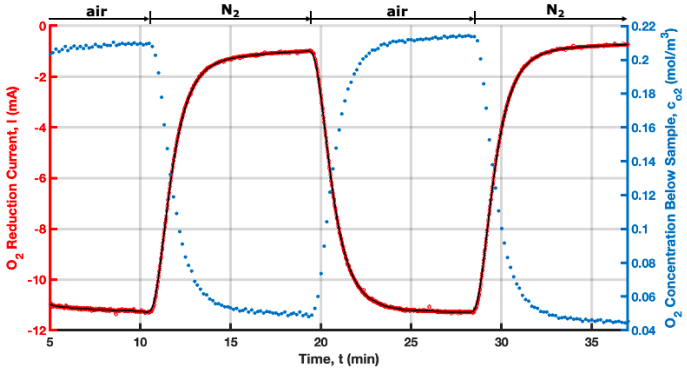

Figure 8: Plot of ORR currents and O_2 concentration measured below the ionomer sample under alternating air and N_2 flows.

3.5.3 Ionomer Thin Film Thickness Measurement

After testing, we took the sample out of the fuel cell hardware and placed the sample in the vacuum oven at 80°C for 24 hours to dry off any water in the ionomer or AAO membrane. As shown in Figure 9a, we used a diamond scribe to scratch off a small area of the ionomer thin film at three different locations of each sample. With the help of the CMU Nanotechnology Laboratory, we used a KLA profilometer (Milpitas, California) to measure the height across the entire sample. The thickness of the ionomer thin film was the difference between the height of the un-scratched and scratched areas, shown in Figure 9b.

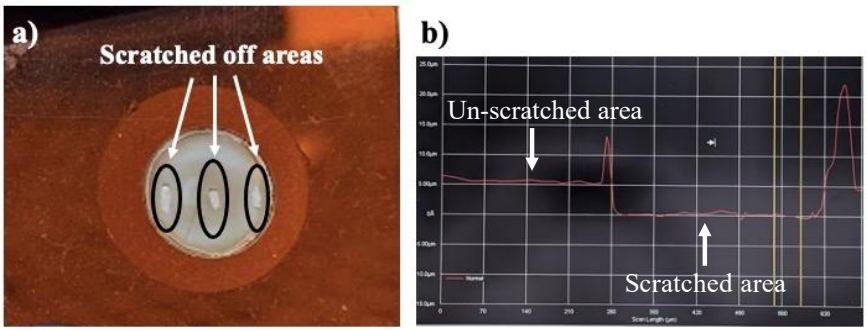

Figure 9: Picture of (a) a sample prepared for thickness measurement and (b) a profilometer profile of a sample.

3.5.4 Oxygen Concentration Correction and Oxygen Permeability Calculation

As shown in Figure 10, the oxygen sensor was located 8.9 mm below the sample. Because there was an oxygen concentration gradient between the sample and CCL of the MEA, we performed data extrapolation to determine the values of O_2 concentration right below the sample. As mentioned above, the O_2 concentration reached zero at CCL under the limiting current condition. With the measured oxygen resistance (R_{O2}) between the gas diffusion layer (GDL) and CCL, we can calculate the O_2 concentration at GDL as:

$$c_{O2,GDL} = c_{O2,CCL} + \Delta c_{O2,GDL-CCL} = 0 + R_{O2}\, J_{O2} = R_{O2}\, J_{O2} \tag{2.1}$$

where J_{O2} is the oxygen flux and can be determined from Faraday's law of electrolysis [24]:

$$J_{O2} = \frac{I}{nF} \tag{2.2}$$

where I is the ORR current of the MEA, n is the number of electrons transferred during ORR (4 in this case), and F is the Faraday's constant.

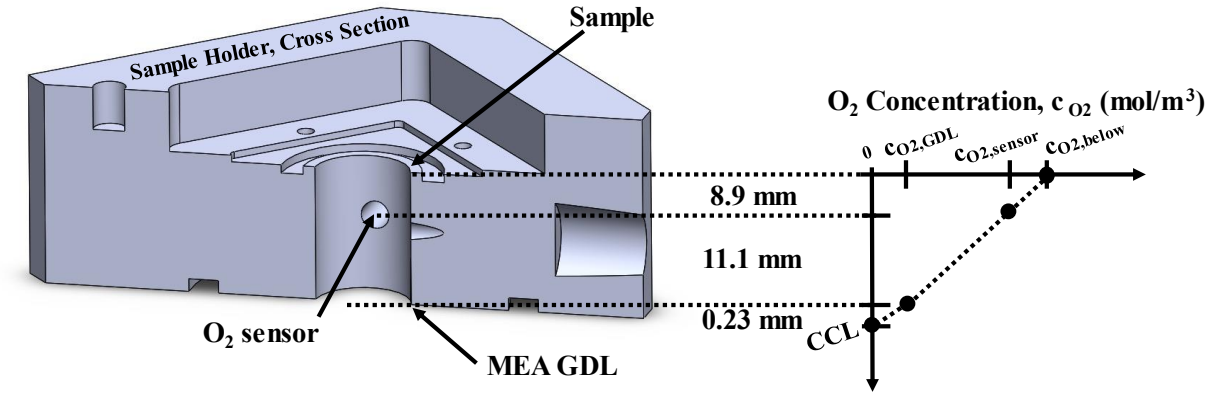

Figure 10: Illustration of the oxygen concentration gradient between the sample and CCL.

With the known values of O_2 concentration at GDL and the sensor as well as their distances from the sample, under a constant oxygen flux flowing through the sample holder channel, we determined the oxygen concentration right below the sample by linear

interpolation. We then calculated the O_2 concentration drop across the ionomer-on-AAO-on-Kapton sample as the difference in concentration between directly on top of (21% O_2 in air) and right below the sample. The oxygen permeability of the ionomer was calculated by using the equation below:

$$\varepsilon_{O2} = \frac{Il}{nAF\Delta C_{O_2} RT} \tag{2.3}$$

where ε_{O2} is the oxygen permeability, *l* is the thickness of ionomer thin film, A is the circular area of the sample, ΔC_{O_2} is the oxygen concentration drop across the ionomer thin film sample, *R* is the universal gas constant, and *T* is the sample temperature.

3.5.5 Results

Multiple samples were fabricated and tested for both Nafion™ D2020 ionomer and HOPI. Figure 11 shows the oxygen permeability measurements for both ionomers. Despite some variability in the data due to the small sample size, the majority of HOPI measurements exhibited higher oxygen permeability when compared to Nafion™ D2020 ionomer. Although the thickness of the ionomer thin films varied between samples, no correlation was observed between the thickness and the oxygen permeability.

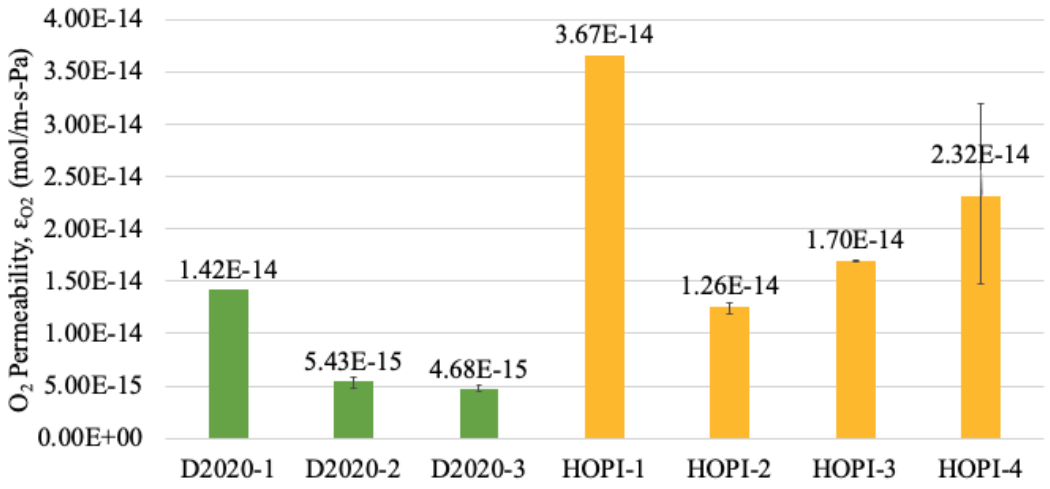

Figure 11: Various oxygen permeability data of Nafion™ D2020 ionomer and HOPI with error bars representing the variation in ionomer thin film thickness.

Additionally, we applied the Student's *t*-distribution to both data sets. Figure 12 shows the averaged O_2 permeability values of both ionomers with an 80% confidence interval. We compared our Nafion™ D2020 oxygen permeability of 8.10E-15 mol/m-s-Pa to the published data of between 4E-17 and 4E-15 mol/m-s-Pa, indicating that our measurements were valid [14]. The HOPIs had approximately three times the O_2 permeability than Nafion™ D2020 ionomers. These ionomers were measured without a

Pt charged interface suggesting the oxygen permeability increase was more likely to be a bulk effect than an interface effect.

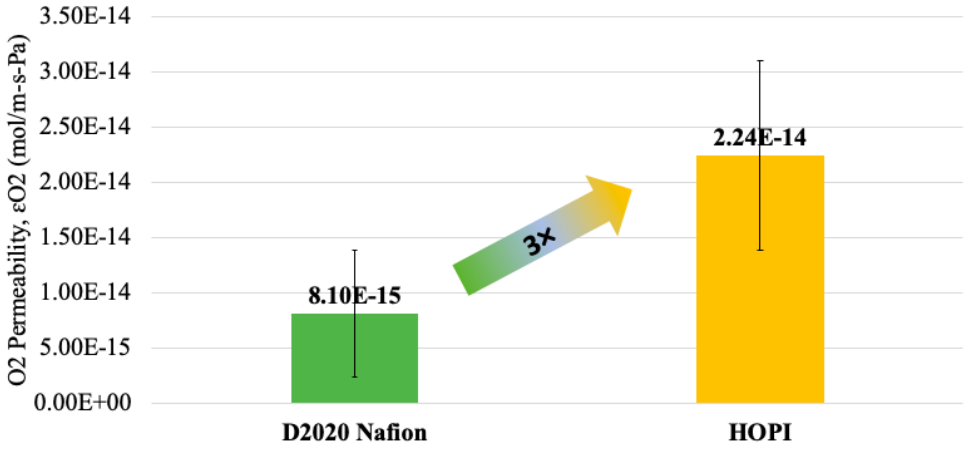

Figure 13: Averaged O_2 permeability measurements of both ionomers with an 80% confidence interval.

4 Molecular-scale Modeling of Ionomer and Interfaces (Task 2)

CMU has focused on the refinement of a molecular dynamics model for examining density profiles and oxygen transport properties of ionomers on a platinum surface. The model has been used to evaluate production D2020, D2020 with a shortened side-chain (D2020 SSC) and HOPI.

Figure 1 shows visualizations of D2020, D2020 SSC and HOPI systems. Equivalent weights for D2020, D2020 SSC and the HOPI are 1140, 883 and 771 g/mol, respectively. For all simulations, mass of ionomer per unit surface area of platinum was held constant. The HOPI exhibits slightly greater thickness compared to D2020 and D2020 SSC, indicating a larger void volume fraction in the HOPI consistent with the higher oxygen permeability. Additionally, both the HOPI and D2020 exhibit reduced clustering of sulfur compared to D2020 SSC.

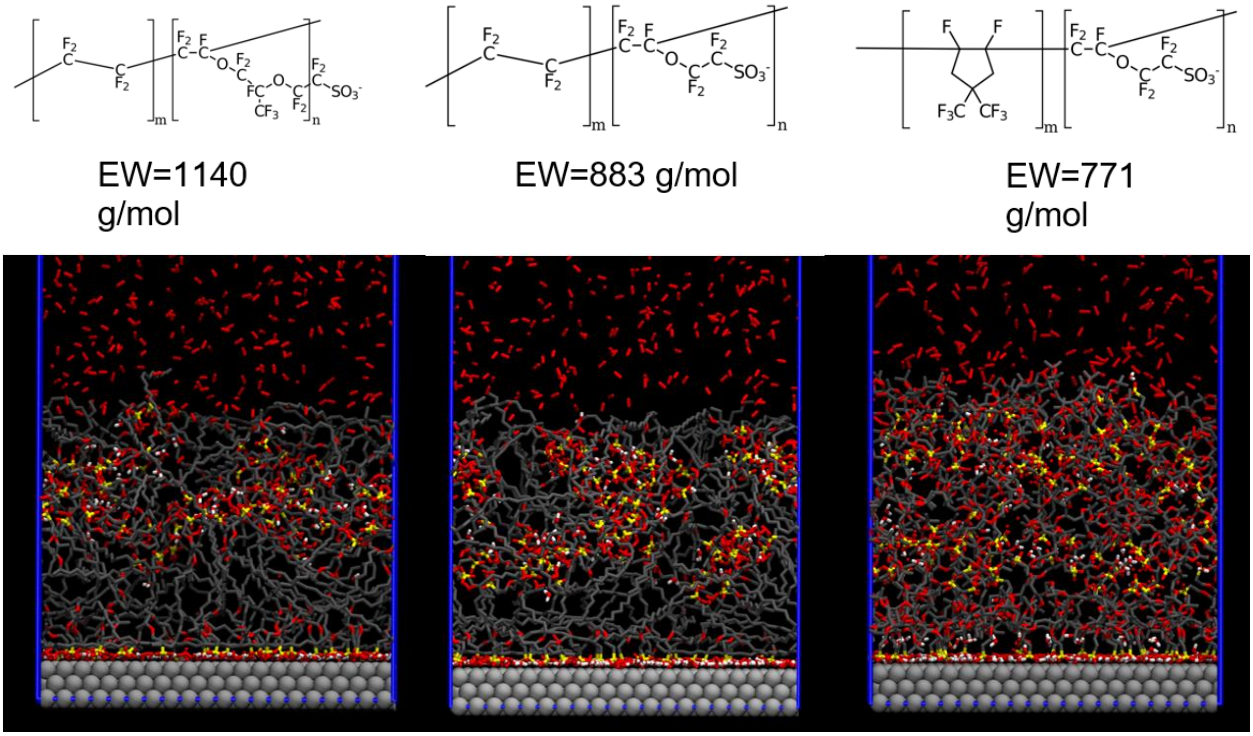

Figure 1: Visualizations of equilibrated structures for D2020, D2020 SSC, and the HOPI. Red indicates oxygen, gray indicates CF_2 groups, white indicates hydrogen and yellow indicates sulfur.

Figure 2 shows the density of the ionomer layer with respect to the height of the simulation box in Figure 1. The HOPI provided a ~42% decrease in density at the platinum-ionomer interface compared to D2020. This should lead to improved oxygen permeability at the platinum-ionomer interface for the HOPI compared to D2020. D2020 SSC exhibits greater density at the platinum-ionomer interface compared to D2020, likely because backbone structure is identical, but equivalent weight is lower. More ionomer molecules are required to maintain the same mass to platinum surface area ratio as D2020, and so more high-platinum affinity sulfur groups are present and able to adsorb to the platinum surface. This

should lead to reduced oxygen permeability at the platinum-ionomer interface for D2020 SSC compared to D2020 when using the same ionomer loading (I/C). In the next quarter, we will specifically investigate oxygen transport properties of the HOPI, D2020 and D2020 SSC. We will calculate oxygen diffusivity, solubility and conduct free energy analysis on oxygen dissolved in the ionomer.

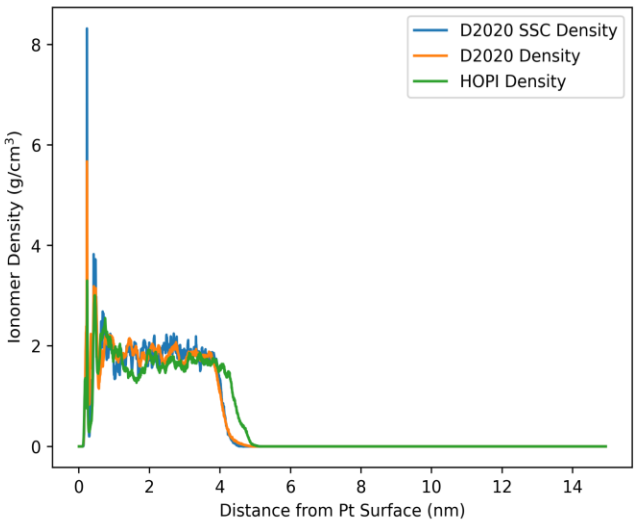

Figure 2: Density of ionomer with respect to height of the simulation box.

CMU evaluated the O_2 self-diffusion coefficient as a function of water number, calculated via molecular dynamics (MD) models, highlighting the effects of bulk morphology on the self-diffusion coefficient. Figure 3 gives diffusivity data for D2020, and a HOPI chemistry. At high water contents, the O_2 self-diffusion coefficient for D2020 is significantly larger than for HOPI. We expect that this is largely attributable to size and continuity of hydrophilic domains.

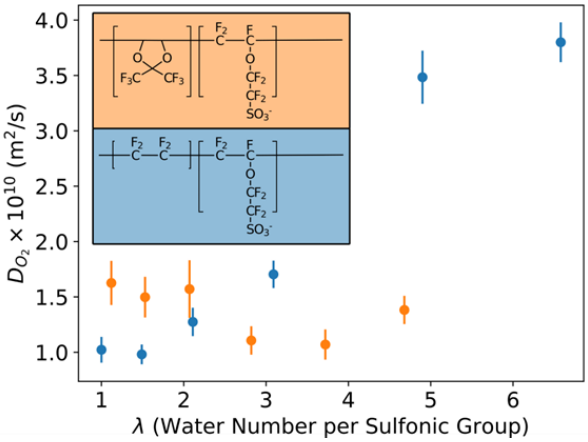

Figure 3: O_2 self-diffusion coefficients at various water numbers for D2020 (blue) and HOPI (orange).

Figure 4 is a visual representation of hydrophilic clustering in the D2020 and the HOPI. A particle is part of a cluster if it is within an arbitrary cutoff distance (in this case, 3 Angstroms) of any other particle in that cluster. D2020 contains large, continuous clusters while the HOPI contains small, fragmented clusters. 18 hydrophilic clusters were counted for D2020, compared to 34 for HOPI. Sources indicate that O_2 preferentially orients at the boundaries between hydrophilic and hydrophobic domains, and we believe that the fragmented domains in the HOPI are confining O_2 and inhibiting the rate of diffusion relative to D2020.

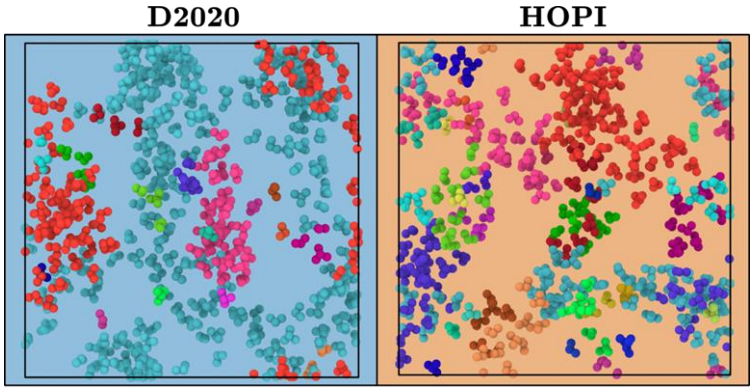

Figure 4: Hydrophilic clustering for D2020 and the HOPI. Particles of the same color are part of the same cluster.

Figure 5 presents solubility and density data for HOPI and D2020. O_2 solubility for the HOPI is higher at all water numbers, which we expect is due to a slightly lower bulk density. Figure 6 gives probability distributions for locating oxygen at a given distance from the catalyst surface.

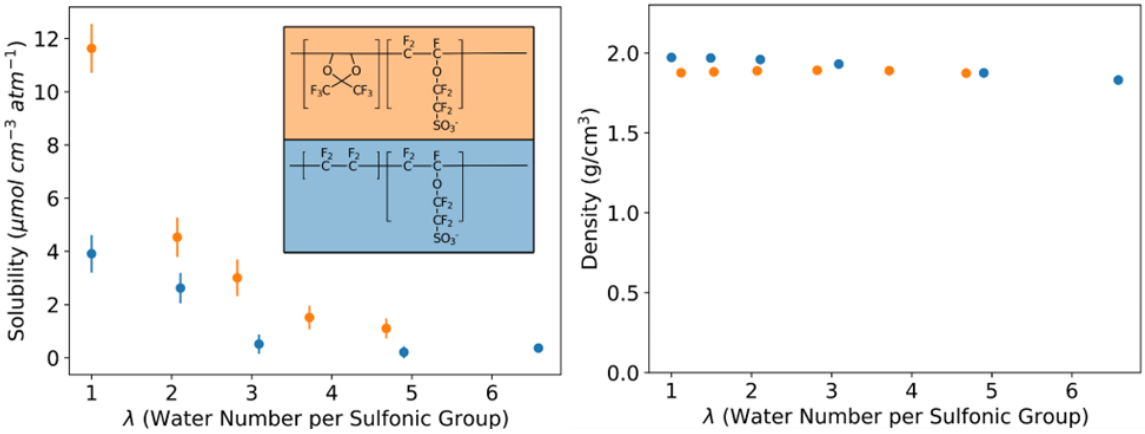

Figure 5: (Left) solubility data for O_2 at different water numbers and (right) bulk density for D2020 and HOPI at different water numbers.

As shown in Figure 6, the majority of O_2 is concentrated close to the catalyst, especially at low humidities. As humidity increases, the peak shifts up. We expect that this is due to the formation of a water monolayer at the catalyst surface. Strong enthalpic interactions cause water to irreversibly adsorb to the platinum, precluding O_2 adsorption. Figure 7 corroborates this, showing a distinct water monolayer in the HOPI at 85% humidity. This same monolayer does not form at 53% humidity, and O_2 is free to adsorb to the catalyst.

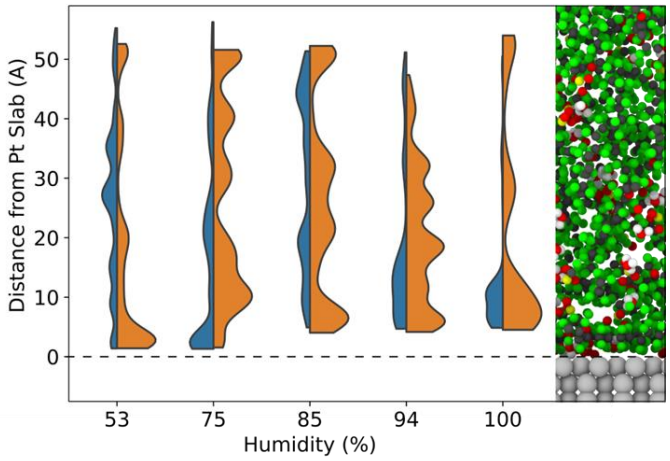

Figure 6: Kernel density estimations for oxygen distributions at different humidities for the HOPI (orange) and D2020 (blue). Distributions at the same humidity share a common scaling.

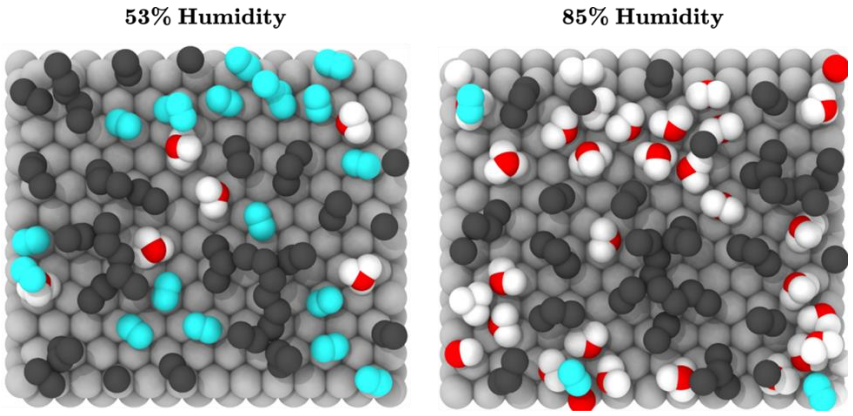

Figure 7: Visual representations of HOPI interfacial region at two water numbers. All atoms shown are within 7 Angstroms of the platinum surface. At low humidity, a large number of O_2 molecules are adsorbed. At high humidity, O_2 is at least the distance of the water monolayer from the surface.

Figure 8 shows the results for permeability, which is a combination of diffusivity and solubility values. The results show the significant increase of permeability across the range of water contents and the very large increase at lower water content. The solubility results indicate that the higher permeability observed in the HOPI is attributable to solubility effects. Solubility for the HOPI is much higher overall, but the majority of O2 is concentrated at the interface between the ionomer and catalyst.

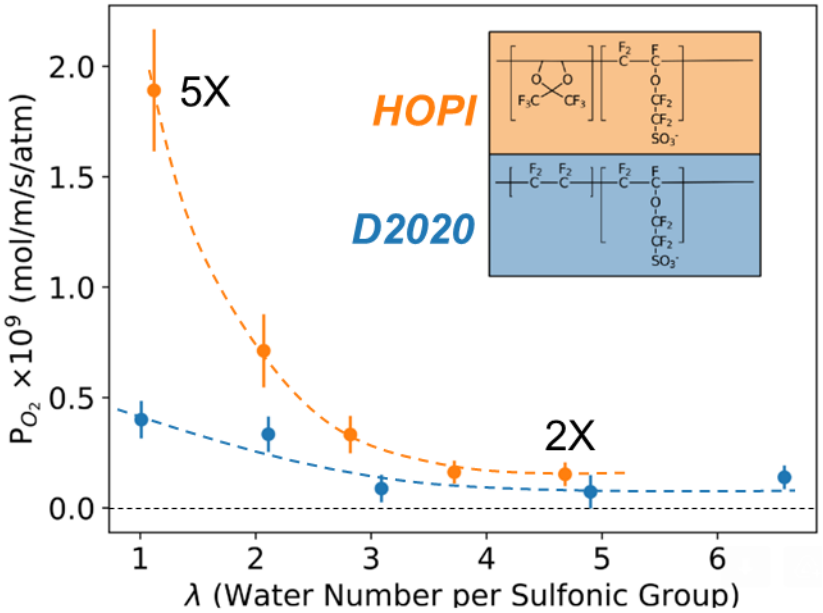

Figure 6: Permeability for O_2 at different water contents for D2020 and HOPI at different water numbers.

5 MEA-scale Modeling of HOPI Impact on PEMFC Performance and Durability (Task 2-4)

Related to Subtask 1.2.4, CMU performed MEA modeling of the impact of HOPI. The CMU model is a PGM version of the model developed in their prior PGM-free ElectroCat project. The model is updated for Pt/C catalysts and their electrode morphologies. It is a multiphase, non-isothermal model with a detailed oxygen and water transport formulation. As Figure 1 shows, the equation for the ORR rate separately includes the solubility and diffusivity of the ionomer. It accounts for ionomer poisoning of the catalyst and the local resistance of ionomer densification at Pt interfaces. The 3X O_2 permeability of the HOPI is implemented through equally increased solubility and diffusivity. Figure 1 shows the effect of loading on the polarization curves with different Pt loading with baseline D2020 ionomer and the polarization curves for 0.025 and 0.2 mg Pt/cm^2. The curves show the enhanced performance over the entire polarization curve, not just the mass transport region. The increased solubility has the impact of increasing the apparent activity because of the higher oxygen concentration in the ionomer.

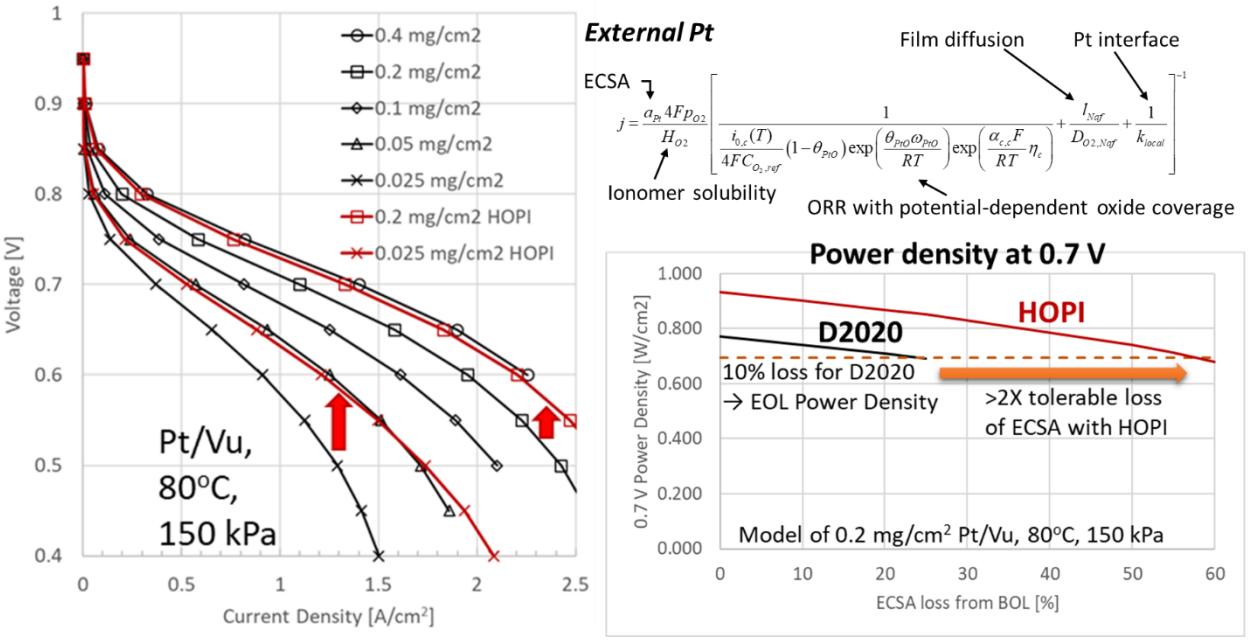

Figure 1. MEA modeling as a function of loading and baseline ionomer versus HOPI with an equation for the Pt area-specific ORR. The 0.7 V power density as a function of % ECSA loss for D2020 and HOPI.

Figure 1 also shows the results of an analysis of HOPI on the 0.7 V power density as a function of the amount of ECSA lost versus the baseline D2020 ionomer. An end-of-life power density is based on the power density when the D2020 value has decreased by 10%. As the plot shows, the amount of tolerable ECSA loss increases from 25% to 56% when using HOPI because of the increased activity. Figure 2 shows a similar effect when looking at the voltage efficiency, as ECSA is lost with each ionomer when there is a constant power density of 0.7 W/cm^2. For that power, the HOPI yields a 3.3% increase in voltage efficiency. The increases above in power density and voltage efficiency are both due primarily to the modeled increase in solubility. The impact of the greater O_2 diffusivity

with HOPI is apparent in the maximum power density plot in Figure 2, which shows a 13% increase in maximum power density when using the HOPI. This model was implemented for a catalyst like Pt on Vulcan carbon black, where the Pt is primarily in contact with ionomer. Future work will expand the model to include internal Pt on HSC catalyst.

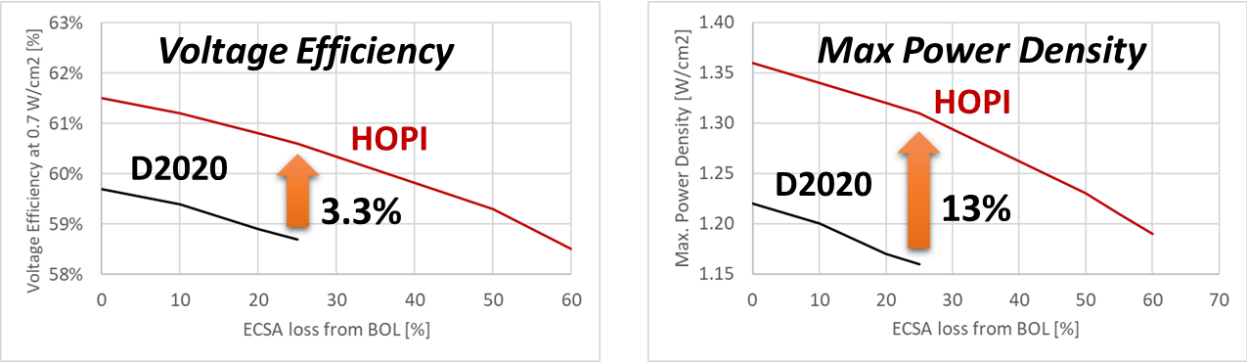

Figure 2. Modeling of voltage efficiency and maximum power density of baseline D2020 and HOPI.

6 HOPI-enhanced Cathode Fabrication and Testing (Task 2)

This section describes the development of a conventional ionomer baseline (Nafion D2020) and the development of a cathode fabrication process for HOPI. Four ionomers have been evaluated in this study, the baseline D2020, the lower EW Nafion DE2029 (880 EW), and the two HOPIs (NDP 5001 and NDP 5006). The DE2029 ionomer was included in the study since it has a lower EW, similar to the HOPIs.

The first set of experiments with HOPI was with NDP 5001, which was the original variant that was not chem-stabilized. The first study done with NDP 5001 was an I/C study, where prepared electrodes with I/C ratios of 0.4, 0.6, and 0.9. The catalyst was the HiSPEC 4000 Pt on Vulcan support (40% Pt/C).

Figure 1 shows the SEMs of the electrodes at the I/C ratios. The images at high resolution show a good dispersion of the catalyst aggregates with no apparent large agglomerates of ionomer. The larger field of view images show the cracking, which is evident with HOPI and the increasing degree of cracking with higher I/C. In the next quarter, we will investigate solvents to reduce cracking.

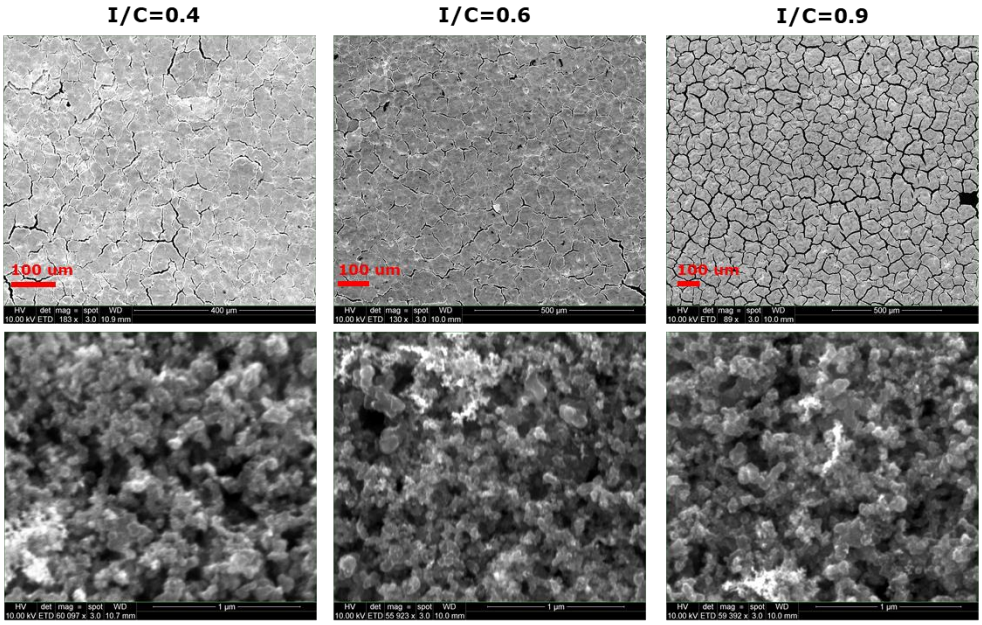

Figure 1. SEM images of NDP 5001 HOPI electrodes prepared with three different I/C ratios.

Figure 2 shows the polarization curves for oxygen and air testing of the HOPI NDP 5001 ionomer at 80°C, 150 kPa, and 100% RH. The loading of the electrodes were 0.26 mg_{Pt}/cm^2 ± 0.01 mg_{Pt}/cm^2, based on weighing and verified by ECSA. For both oxidant gases, the I/C of 0.6 provides notably higher performance, approaching 0.7 V at 1 A/cm^2 with air. The I/C of 0.9 showed spuriously low performance relative to expectations. It could be a result of excessive electrode cracking.

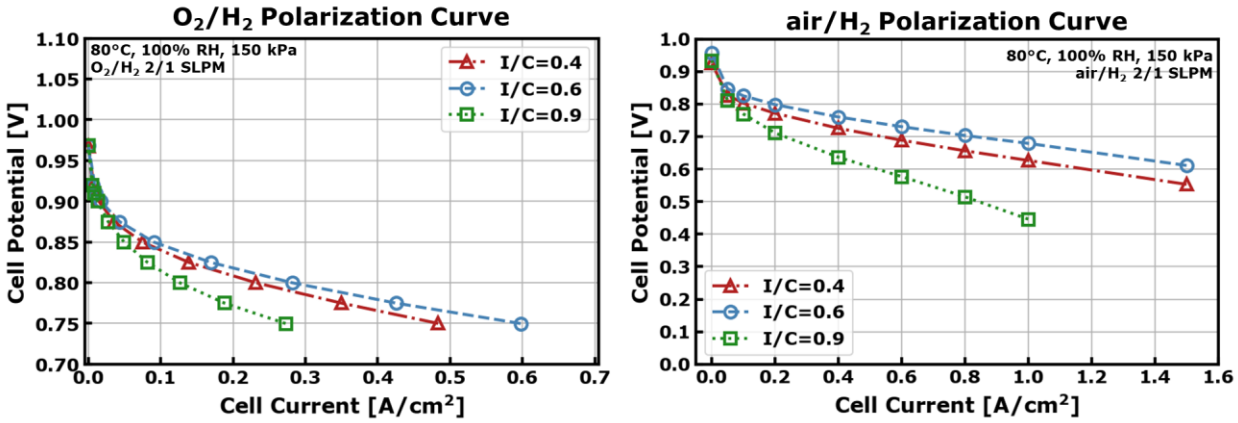

Figure 2. Oxygen and air polarization curves for HOPI NDP 5001 at three I/C ratios.

Figure 3 shows the total oxygen transport resistance at 75% RH as function of pressure, which is used to evaluate the pressure independent resistance (non-Fickian). The non-Fickian resistance (R_{NF}) is largely an outcome of ionomer films around the catalyst. As expected, the lower I/C ratios provided reduced R_{NF} as shown in the table in Figure 3. Similar to the polarization curves, the I/C of 0.9 showed a spurious result of very high oxygen transport resistance. Again, the I/C of 0.9 should be revisited in future work.

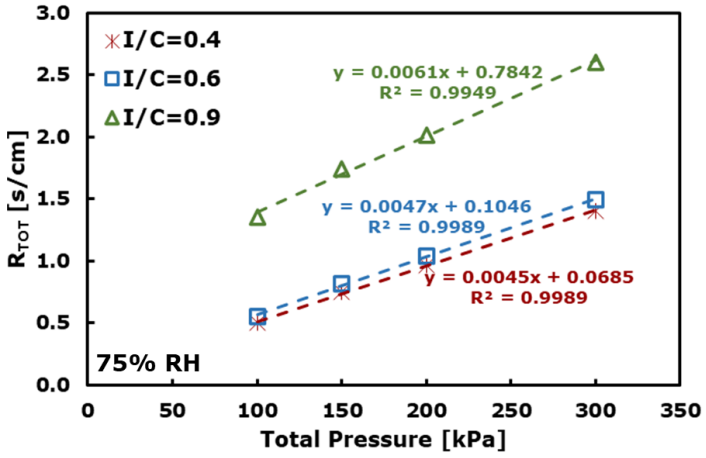

I/C	Intercept	Slope	R_{NF} [s/cm]
0.4	0.0685	0.0045	0.13
0.6	0.1046	0.0047	0.16
0.9	0.7842	0.0061	0.86

Figure 3. Oxygen transport resistance analysis for the three I/C ratios at 75% RH.

Using the I/C of 0.6 optimum from the HOPI NDP 5001 I/C study, we performed a comparison of four ionomers with this I/C. The four ionomers were HOPIs NDP 5001 (EW ~840) and NDP 5006 (EW ~870), D2020 (EW ~1000), and DE2029 (EW ~880). Figure 4 shows a SEM comparison of the D2020 and HOPI NDP 5001 electrodes at three levels of magnification. The images show a similar microstructure in the 75X images, however, the HOPI NDP 5001 electrode shows a notable degree of greater cracking.

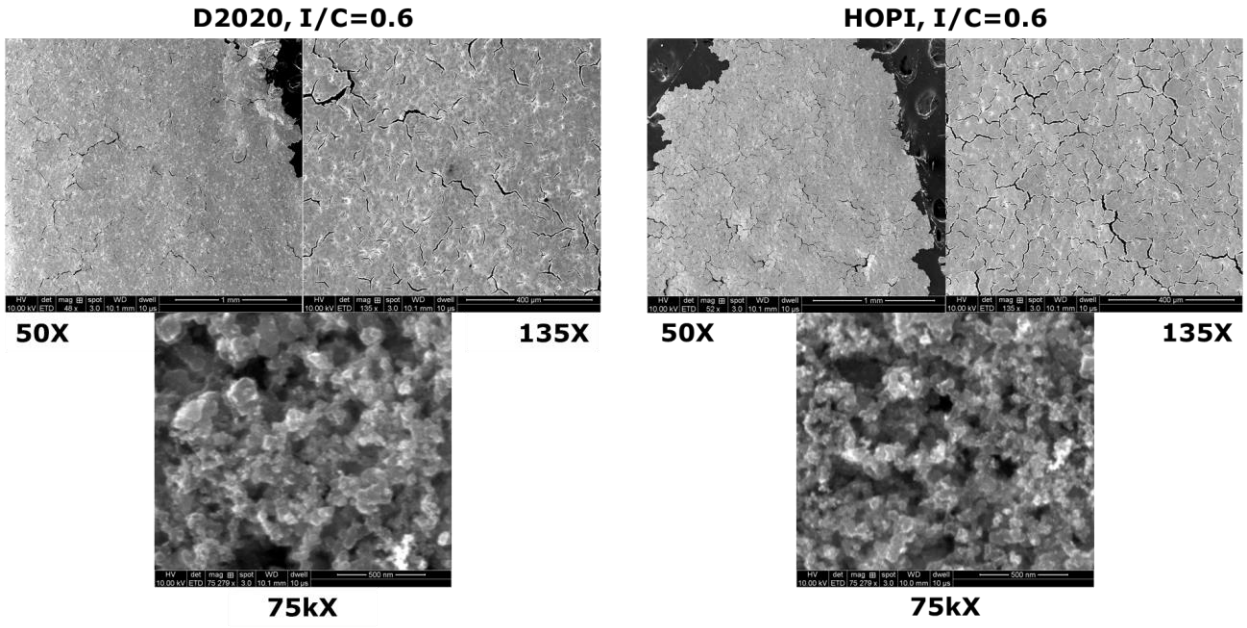

Figure 4. SEM comparison of electrodes prepared with D2020 and HOPI.

Figure 5 shows the oxygen and polarization curves for the four ionomers tested at an I/C of 0.6. The loadings for the electrodes were 0.215 mg_{Pt}/cm^2 ±0.015 mg_{Pt}/cm^2 based on weighing and verified by ECSA, which is ~20% lower than the loading in the I/C study. Both HOPIs outperformed the Nafion D2020 and DE2029 electrodes. The DE2029 showed similar mass activity to D2020 in oxygen but exhibited greater mass transport losses at 1.5 A/cm^2 with air. The NDP 5006 HOPI showed the highest performance of all the ionomers with significantly increased mass activity. Versus D2020, the chem stabilized HOPI NDP 5006 provided a ~25% increase in current density at 0.7 V with air. The present hypothesis for the increased mass activity is a greater solubility of oxygen in the HOPIs.

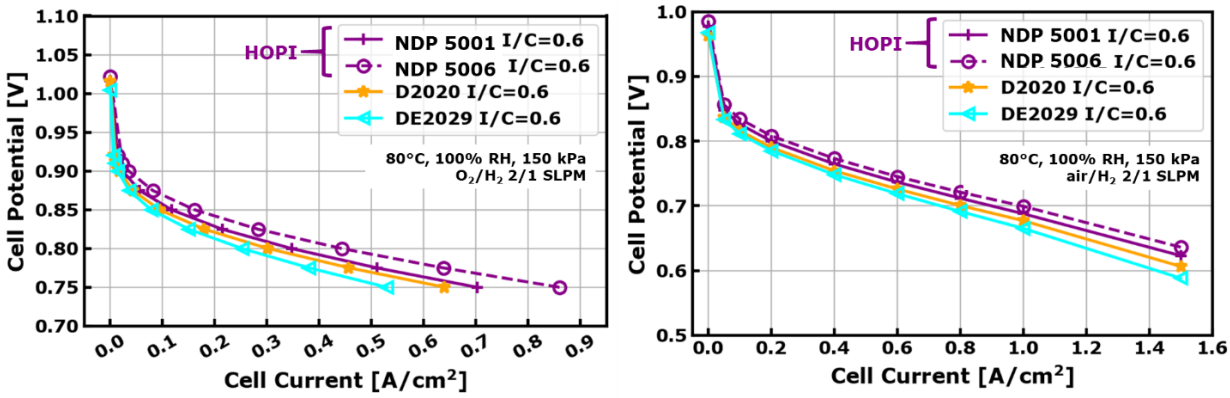

Figure 5. Oxygen (left) and air (right) polarization curves for the four different ionomers.

Figure 6 shows a comparison of the pressure independent resistances of the four ionomers. At these range of RH values, the HOPIs exhibit lower R_{NF} values compared to D2020 and D2029. In general, the R_{NF} increase at low RH is attributed due to the collapse of the ionomer films due to dehydration and these results are consistent with that behavior for all ionomers. However, the HOPIs exhibit significantly lower sensitivity to RH compared to D2020 and D2029. At 25% RH, the HOPI RNF is roughly half that of D2020, suggesting more dramatic impacts on performance in drier conditions versus the 100% RH conditions tested up to this point. The reduced sensitivity of the HOPI R_{NF}'s is likely the effect of the bulk units in the backbone reducing the compaction of the ionomer with dehydration.

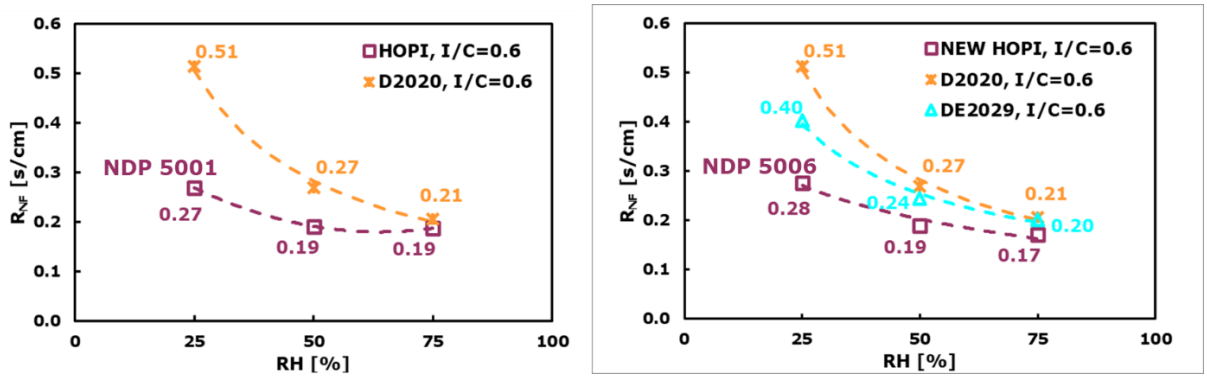

Figure 6. Non-Fickian (pressure-independent) oxygen transport resistances of the four ionomers as a function of relative humidity.

6.1 Ink Optimization Studies

CMU performed catalyst ink optimization studies with the HOPI NDP 5006. This study included a transition to using slower drying n-propyl alcohol (nPA) instead of iso-propyl alcohol to reducing cracking. Figure 7 shows the effect of varying the nPA:water ratio on the polarization curves and pressure independent oxygen transport resistance. The results show a minor effect, with the high water content inks showing slightly increased

oxygen transport resistance. Figure 8 shows the SEMs of the electrodes prepared with the different solvents. The SEMs show the significant cracking with the high water content (1:1) solvent as well as evidence of greater ionomer agglomeration. The cracking likely arises to the lower mobility of the ink during drying due to the more agglomerated ionomer.

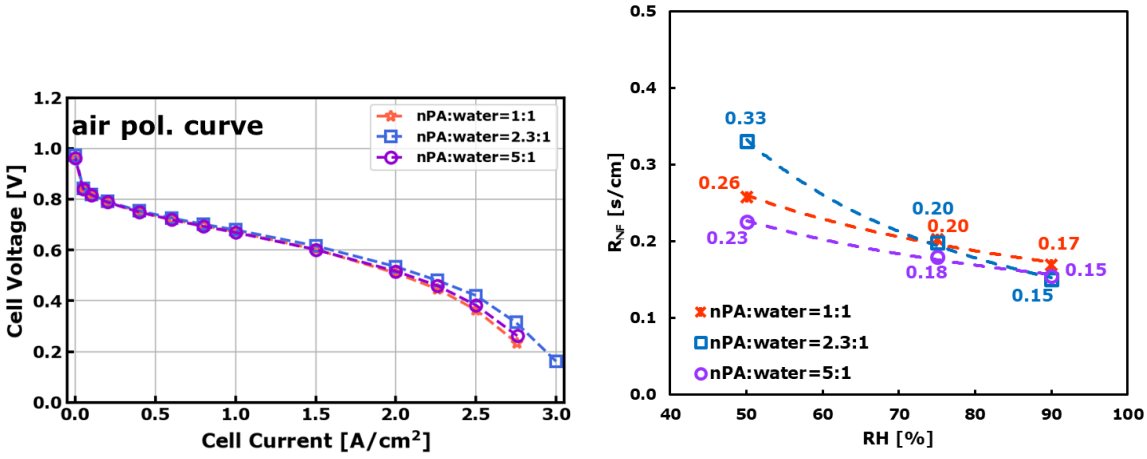

(a) (b)

Figure 7. Effect of catalyst ink solvent nPa to H_2O ratio. (a) Polarization curves (air, 150 kPa, 80°C, 100% RH). (b) Pressure independent oxygen transport resistance.

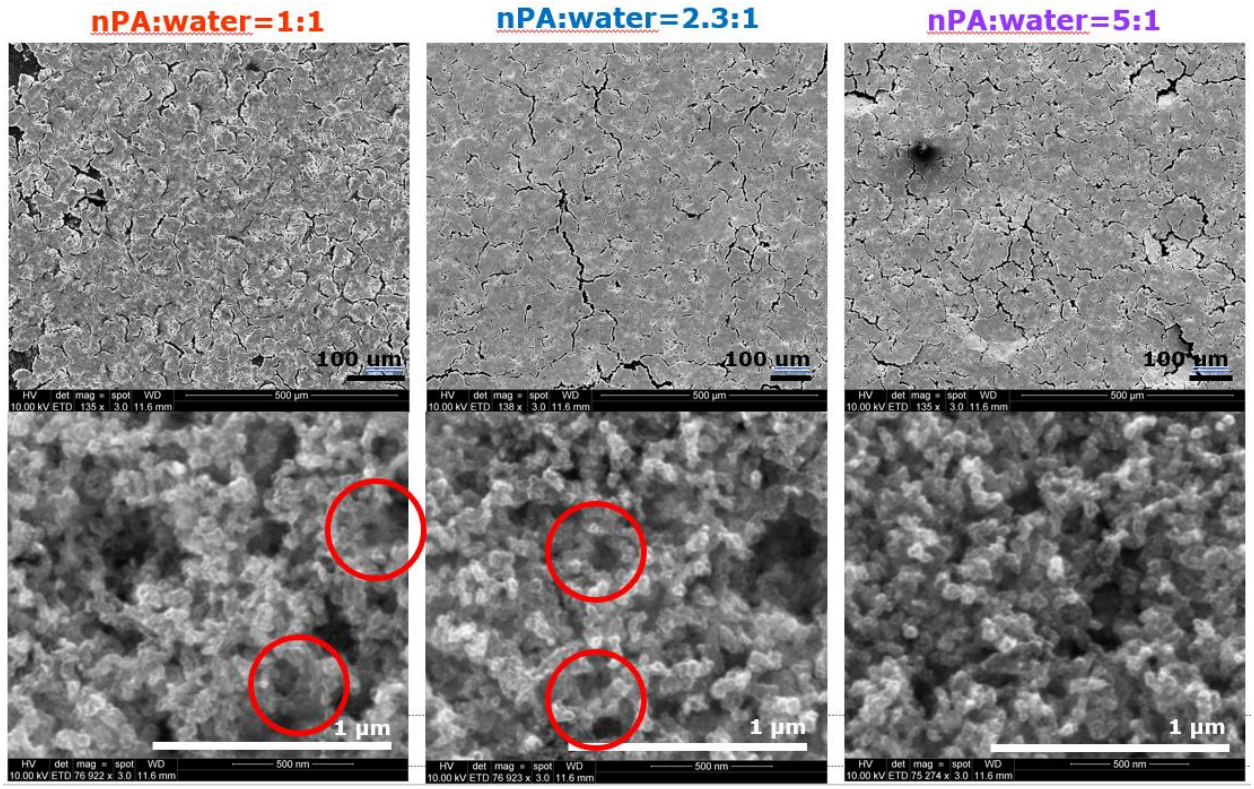

Figure 8. SEMs of the HOPI cathodes prepared with varying solvent ratios.

Figure 9 shows the results of a study on the ionomer to carbon ratio (I/C) for the HOPI NDP 5006 MEAs at CMU. I/C ratios of 0.4, 0.6, and 0.9 were studied. The I/C of 0.6 MEA showed substantially higher performance across the entire polarization curve. The I/C of 0.6 and 0.9 MEAs showed slightly higher mass activity and the I/C of 0.6 MEA had substantially lower oxygen transport resistance than the I/C of 0.9 MEA. Figure 10 shows the SEMs of the electrodes, where it can be seem that the high I/C ratio of 0.9 leads to greater cracking and ionomer agglomeration.

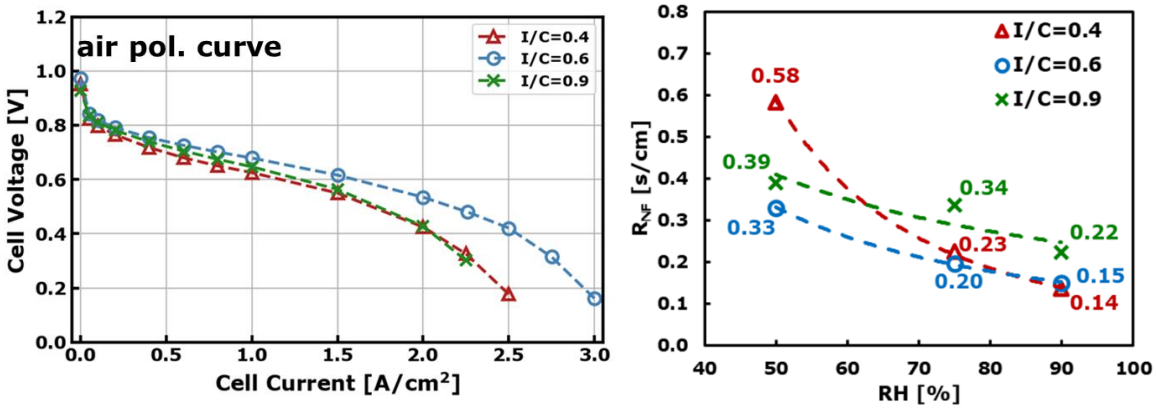

(a) (b)

Figure 9. Effect of ionomer to carbon ratio. (a) Polarization curves (air, 150 kPa, 80°C, 100% RH). (b) Pressure independent oxygen transport resistance.

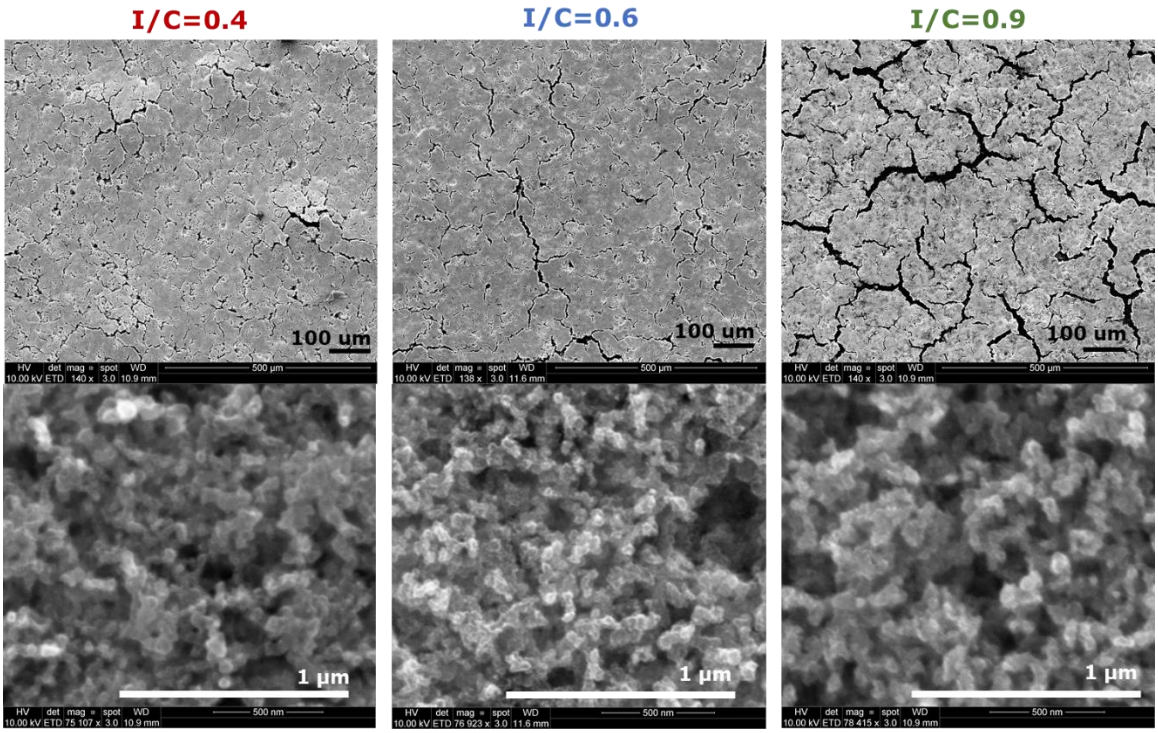

Figure 10. SEMs of the HOPI cathodes prepared with varying I/C ratios.

Nano-CT of CMU Prepared Cathodes

Nano-CT characterization of the CMU-prepared electrodes with HOPI was conducted. The goal of nano-CT imaging is to understand the impact of HOPI on the 3D structure of the electrode. Figure 11 shows a nano-CT image of decals prepared with the Pt/LSAC catalyst (TKK EA50) and the Chemours HOPI and the corresponding electrode with D2020 for the same I/C ratio and ink composition. The imaging was done with the absorption and Zernike phase contrast optics and 65 nm voxels. The MEAs were ion-exchanged with cesium to investigate the dispersion of ionomer in the electrodes when imaged by absorption contrast. The Zernike phase contrast imaging highlights the pore and crack structure. The comparison of the HOPI and D2020 electrodes shows the significantly greater cracking of the HOPI electrode. Furthermore, the Cs+ stained absorption images show more significant heterogeneity in the ionomer density with the HOPI ionomer.

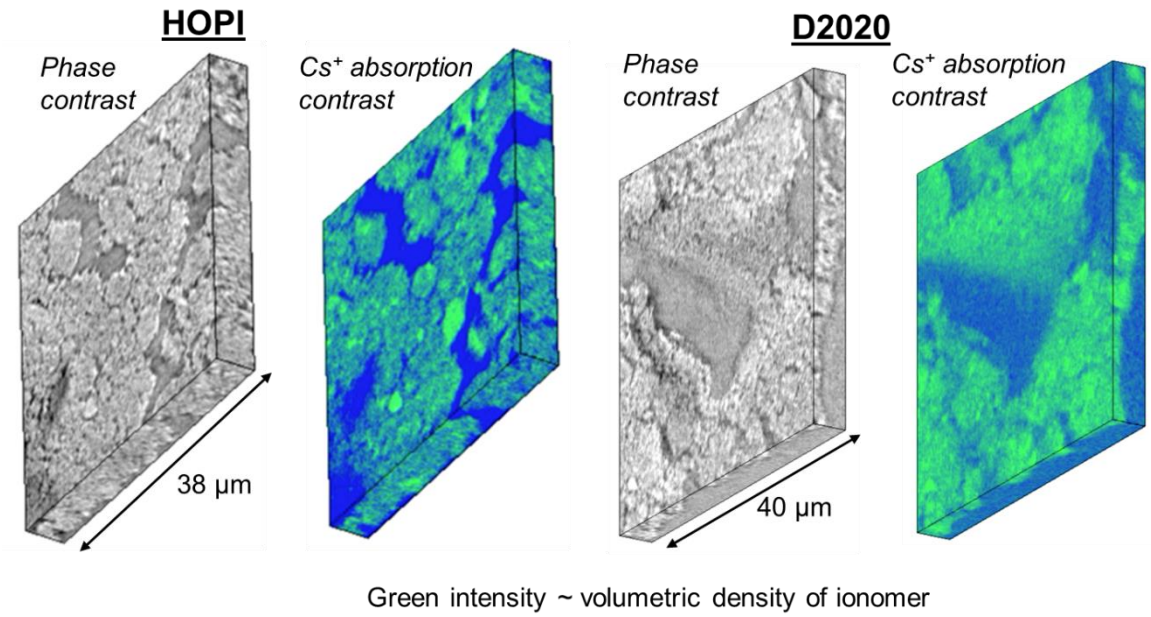

Figure 11. Nano-CT phase contrast images and absorption contrast images of cathodes prepared with Pt/LSAC catalyst and HOPI and D2020. The voxel size is 65 nm.

7 Effect of Carbon Support for HOPI-enhanced Cathodes (Task 2)

In this study, we performed a comparative analysis of using D2020 and HOPI with catalysts having a low surface area carbon support (Pt/LSC) or high surface area carbon support (Pt/HSC). Our primary objective is to evaluate and compare the electrochemical performance when employing these ionomers and catalyst combinations. As shown in Figure 1c, HSC-supported catalysts typically have a significant portion of Pt particles embedded in these internal micropores. In contrast, less porous carbon supports such as medium surface area carbon (MSC) (e.g., Vulcan XC-72R) or low-surface-area carbon (LSC) exhibit minimal internal porosity, resulting in the majority of Pt particles being on the external surface of the carbon.

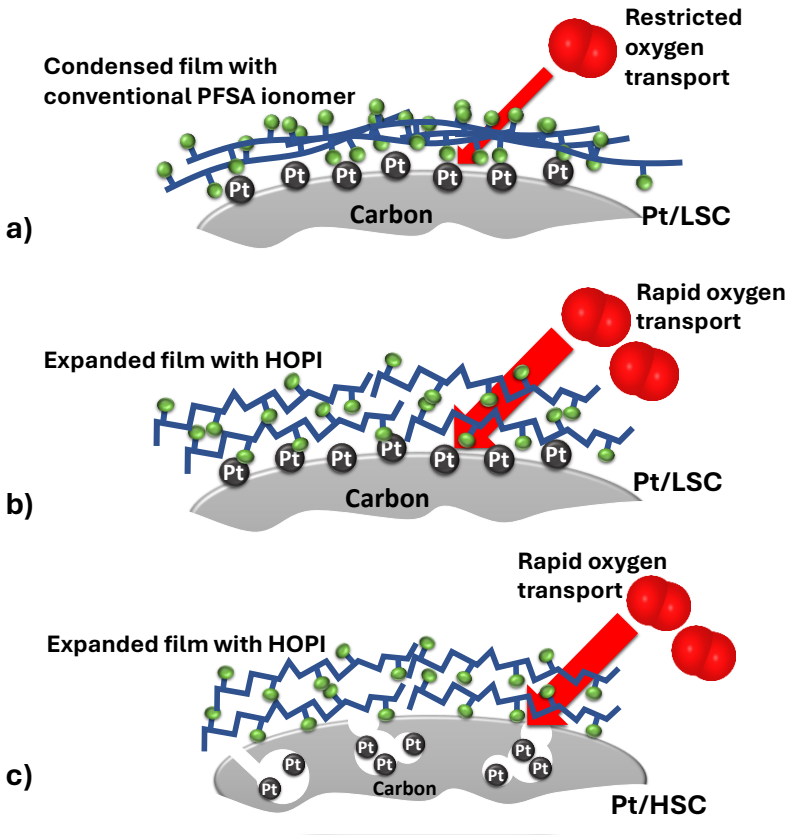

Figure 1: Illustration of oxygen diffusion mechanisms through ionomer films in PEMFC CCLs featuring Pt/LSC and Pt/HSC morphologies.

7.1 Experimental

7.1.1 Ionomers and catalysts

As a baseline comparison, the study utilized Nafion™ D2020, a commercially available ionomer dispersion that follows the standard polymer chemistries of Nafion™, supplied by the Chemours Company. Additionally, Chemours has developed and synthesized a high oxygen permeability ionomer (HOPI).

The catalysts used were a 45.6 wt % Pt on low surface area carbon (Pt/LSC) (TKK EA50) and a 47 wt % Pt on high surface area carbon (Pt/HSC) (TKK TEC10E50E). Pt/LSC can maximize the Pt/ionomer interfacial area, while Pt/HSC is a porous support with a majority of Pt observed within interior carbon pores and with relatively constrictive openings.

7.1.2 MEA fabrication

To prepare the CCL inks, the carbon-supported Pt was mixed with a combination of de-ionized water, n-propanol alcohol (nPA), and ionomer dispersion. The composition of the catalyst ink was meticulously calibrated by weighing each component to obtain precise ratios of solvent (nPA to water), ionomer to carbon (I/C), and the percentage of solids by weight. For blending the ink, a vortex mixer (IKA Lab Dancer, Staufen, Germany) was utilized, gradually incorporating each ingredient. To enhance the uniformity of the ink mixtures, a tip sonicator (Branson SFX250, Brookfield, CT) was employed at 15% intensity for a brief ten-second period. This was followed by a longer thirty-minute sonication bath. Throughout the sonication process, the mixtures were kept in thermal balance using an ice water bath to avert the detachment of platinum particles and to preserve the electrochemically active surface area (ECSA).

Subsequent to the bath sonication, the inks were carefully applied onto a microtextured silicone decal substrate (from 3M Company, Saint Paul, MN). This substrate was then set upon a wet film coater (from MTI Corporation, Richmond, CA), equipped with a film applicator (100 or 150 µm depending on the solids weight percent of the ink), which was guided across the substrate at a low shear rate of 11 mm/s. After the catalyst layers were dried, a 5 cm^2 area of the decal-backed CL was cut out and hot-pressed onto the pre-manufactured anode catalyst-coated membranes (CCMs) (from Ion Power, New Castle, DE). These CCMs featured a Nafion™ HP membrane and an anode catalyst layer (ACL) with a platinum loading of 0.3 mg_{Pt}/cm^2 for Pt/LSC samples and 0.1 mg_{Pt}/cm^2 for Pt/HSC samples spread over an area measuring 2.6 cm by 2.6 cm. The hot press process was performed at a pressure of 2.7 MPa and a temperature of 130°C for a total duration of 8 minutes. The assembly was rotated every two minutes to ensure uniformity. During the hot pressing, a silicone sheet of considerable thickness was placed beneath the membrane electrode assembly (MEA) to ensure even pressure distribution across the entire 5 cm^2 area. Following the 8-minute pressing period, the microtextured silicone decal backing was peeled off while the MEA remained heated, resulting in a consistently complete transfer of the catalyst layer to the membrane.

The constructed MEA was enclosed on each side using adhesive-backed Kapton sheets that were 4 mils (100 µm) thick (from McMaster Carr, Elmhurst, IL). These sheets were attached to the uncovered parts of the membrane along with a 3-mil PTFE gasket (from Fuel Cell Store, College Station, TX), which was not fixed. Sigracet 22 BB Gas Diffusion Layers (GDLs) (from SGL Carbon, Wiesbaden, Germany) were employed, resulting in an approximate GDL compression of 20%. The MEAs underwent testing in standardized fuel cell hardware (from Scribner Associates Inc., Southern Pines, SC). This hardware included a 5 cm^2 single-channel serpentine flow plate for the anode and a custom-designed differential-style graphite flow plate with 21 parallel channels used for the cathode.

7.1.3 Electrochemical testing

We employed comprehensive break-in procedure with voltage recovery (VR). For our experimentation, we implemented an initial sequence of wet (100% RH) and dry (32% RH) voltage cycling at 80°C, followed by VR cycles consisting of low-temperature (40°C) holds at high relative humidity (150%) and under low voltage conditions. After completing the conditioning protocol, MEAs with Pt/LSC underwent testing procedures. We warmed up the cell with Pt/HSC MEAs to 80°C and first performed limiting current measurements at 75% RH to calculate the R_{NF}'s. Then we brought up the RH to 100% to take the cyclic voltammograms (CVs) and electrochemical impedance spectroscopy (EIS) measurements. We finished the performance testing with anodic air and O_2 polarization curves using 4 min holds at each current density (for the air polarization curve) and voltage (for the O_2 polarization curve).

7.2 Results

During the catalyst ink fabrication, the ionomer to carbon ratio (I/C) was maintained at a consistent value of 0.6, a level that has been established as optimal for the D2020 with Pt-on-Vulcan combination. We also held the nPA to water ratio constant at 2.3:1, which has shown to have the best fuel cell performance for the HOPI with Pt/LSC system. The solids weight percentage of inks varied from 10% to 15%, and by varying the wet film thickness, the Pt loadings of the Pt/LSC and Pt/HSC MEAs were 0.20 ± 0.02 mg_{Pt}/cm^2 and 0.30 ± 0.01 mg_{Pt}/cm^2, respectively.

We first conducted a CV analysis measured with a Pt/HSC MEA with HOPI at various RHs, ranging from dry (15%) to wet (100%). As shown in Figure 2, this approach allows for the calculation of Pt ECSA and utilization across various RH levels for the Pt/HSC catalyst. Unlike the Pt/LSC catalyst with a 100% Pt-Ionomer coverage and no ECSA dependence on RH, the Pt particles in the Pt/HSC catalyst are located within carbon pores, which are not accessible to the ionomer. As we increase the RH, capillary-condensed water pathways to the internal Pt are formed, thus increasing the Pt utilization. By calculating the ECSA at each RH and normalizing it to the ECSA at 100% RH, we observed that, at low RH level, the fraction of the external Pt is approximately 38%.

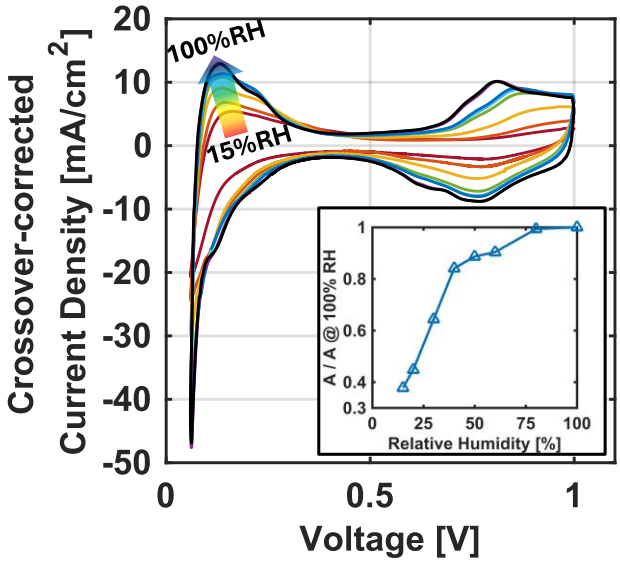

Figure 2: CVs of HOPI with Pt/HSC at 80°C, 150 kPa_{tot}, N_2/H_2 at 0.05/0.1 SLPM, and a sweep rate of 50 mV/s with inset Pt utilization for various RH levels.

Figure 3a shows the CVs for the D2020 and HOPI-based CCLs with Pt/LSC and Pt/HSC catalysts. Pt/LSA MEAs with Pt loadings of 0.2 mg_{Pt}/cm^2 have an average RF value of 104 ± 2%, and with higher Pt loadings of 0.3 mg_{Pt}/cm^2, the Pt/HSC MEAs have a higher average RF value of 165 ± 1%. The CVs displayed minimal disparity among the ionomers, with no noticeable changes in peak positions or their relative sizes. In both Figures 3b and 3c, the HOPI ionomer appears to outperform the D2020 ionomer over the range of current densities presented, irrespective of the catalyst used. Furthermore, the difference in performance between the ionomers appears more pronounced at higher current densities, suggesting that HOPI may be better suited to maintaining performance under the increased demands of higher power output, which could be critical for applications that require fuel cells to operate at higher loads.

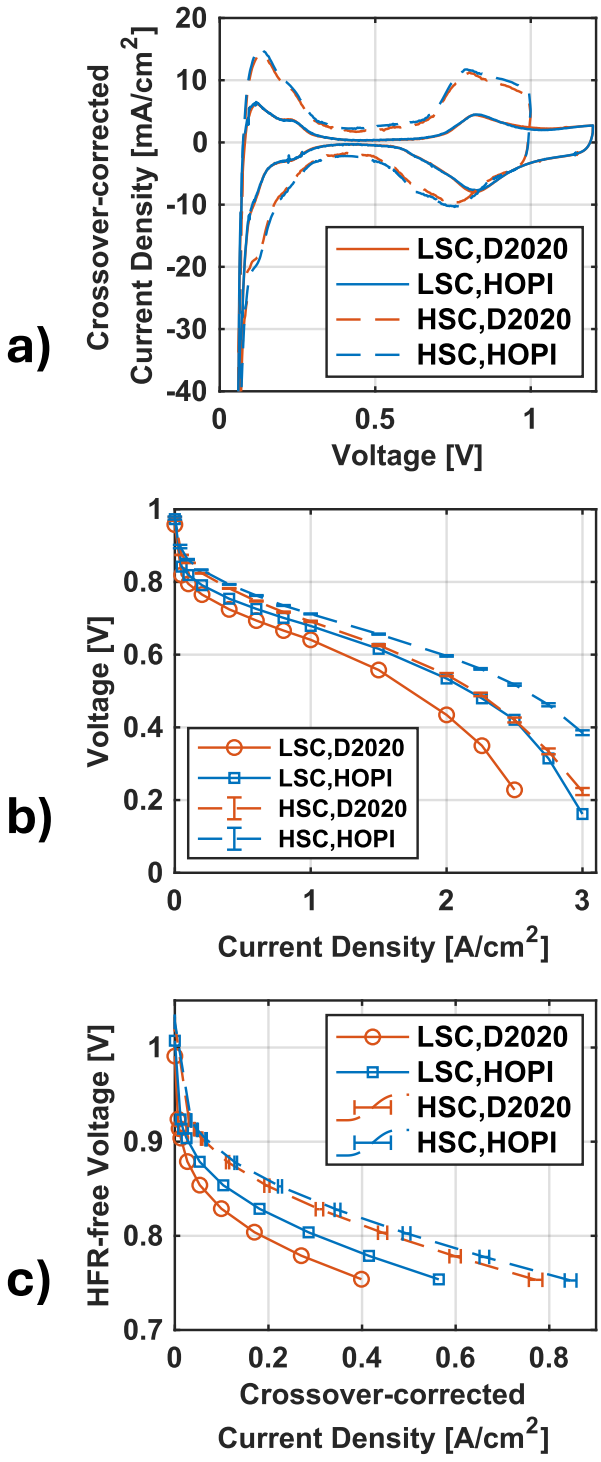

Figure 3: Characterization of D2020 and HOPI-based CLs with Pt/LSC (0.20 ± 0.02 mg_{Pt}/cm^2) and Pt/HSC (0.30 ± 0.01 mg_{Pt}/cm^2). (a) CVs at 80°C, 100% RH, 150 kPa_{tot}, and N_2/H_2 at 0.05/0.1 SLPM with a sweep rate of 50 mV/s. (b) air/H_2 polarization curve and (c) O_2/H_2 polarization curve at 80 °C, 100% RH, and 150 kPa_{tot} under flow rates of 2/1 SLPM.

In evaluating the normalized performance of MEAs incorporating HOPI and D2020 ionomers with Pt/LSC and Pt/HSC catalysts, a distinct trend emerged. When assessing voltage at 2 A/cm² (Figure 4a), both Pt/LSC and Pt/HSC samples with the HOPI ionomer exceeded the baseline established by D2020, with Pt/LSC slightly outperforming Pt/HSC. Upon examining the current at 0.8 V (Figure 4b), Pt/LSC with HOPI demonstrated superior performance, achieving more than 150% of the D2020 baseline, while Pt/HSC with HOPI showed just slightly higher than 100%. This indicates that HOPI, when paired with LSC, facilitates enhanced ionomer-catalyst interactions due to 100% external Pt.

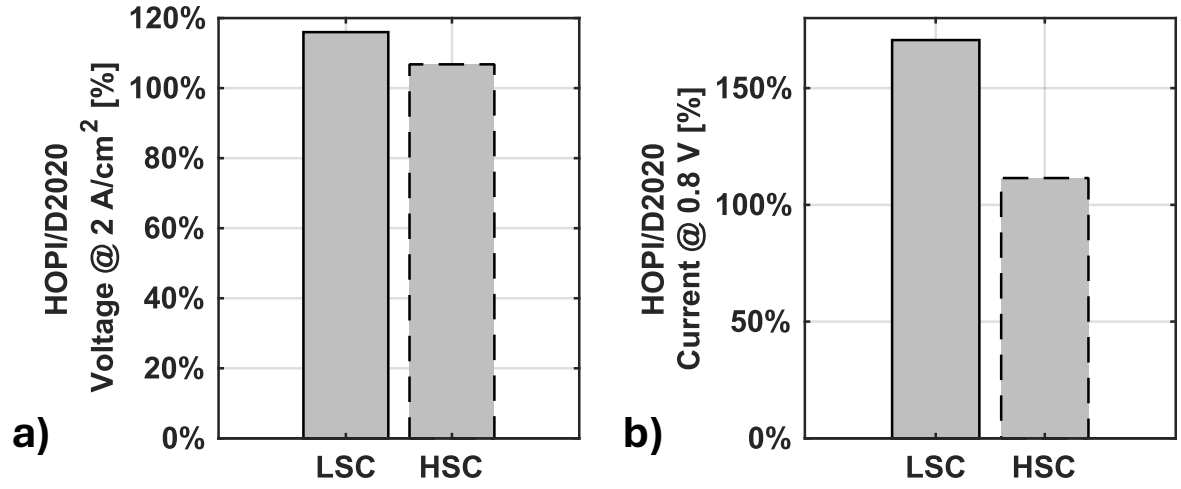

Figure 4: Comparative analysis of MEA performance using Pt/LSC vs. Pt/HSC with HOPI and D2020 ionomers. (a) Normalized voltage at 2 A/cm², and (b) normalized current at 0.8 V, with respect to D2020 ionomer as the baseline.

Further insights were obtained from the specific activity (SA) comparison (Figure 5a), where Pt/LSC with HOPI maintained an SA almost 200% that of the D2020, reaffirming the catalytic advantage of LSC with HOPI. In contrast, Pt/HSC with HOPI exhibited an SA closer to 100% of the D2020 reference, underscoring a less pronounced benefit from the high surface area carbon in the presence of HOPI.

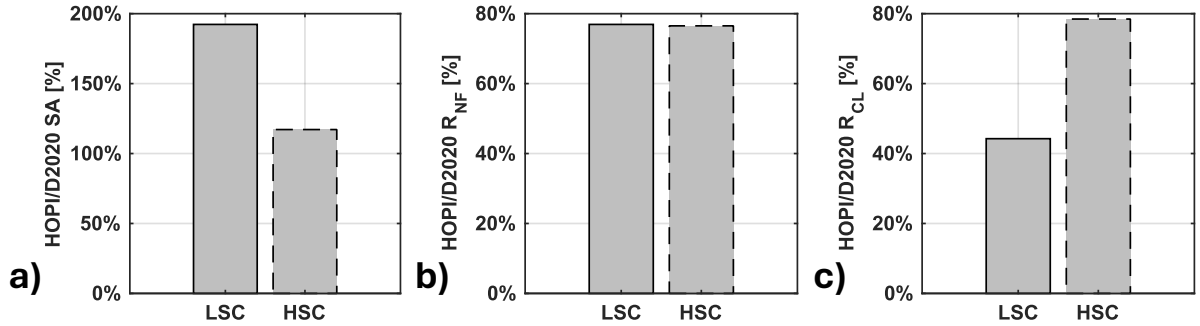

Figure 5: Comparative analysis of MEA properties using Pt/LSC vs. Pt/HSC with HOPI and D2020 ionomers. (a) Normalized specific activity (SA), (b) normalized non-Fickian O_2 transport resistance (R_{NF}), and (c) normalized electrode resistance (R_{CL}), all with respect to the D2020 ionomer as the baseline. All experimental data are included in the *Supplemental Information*, Table S1.

Figure 5b compares the normalized non-Fickian O_2 transport resistance (R_{NF}) when using the HOPI ionomer versus the D2020 ionomer across both Pt/LSC and Pt/HSC catalysts. The film diffusion, which is the transport of oxygen through the ionomer film, is a significant component of local transport resistance to both internal and external platinum sites. Figure 5b shows a reduction in R_{NF} for both catalysts with HOPI, suggesting that the improved O_2 transport due to HOPI's bulk properties (approximately two to three times greater than D2020) benefits catalysts with both types of carbon supports. However, the decrease was not significantly different between Pt/LSC and Pt/HSC. This indicates that the reduction in R_{NF} with HOPI is not merely due to a densification effect at the platinum interface but is a bulk property of the ionomer that enhances O_2 transport across the entire catalyst layer.

Figure 5c shows the electrode resistance (R_{CL}) in CCLs using HOPI and D2020 ionomers paired with Pt/LSC and Pt/HSC catalysts. The bar chart shows that for both catalyst types, HOPI achieves a substantially lower R_{CL} compared to D2020. This improved performance with HOPI is largely due to its lower equivalent weight (EW) of 856, compared to D2020's EW of 1000. The reduced EW results in a greater concentration of sulfonate groups per volume, enhancing proton conduction pathways and, consequently, increasing overall ionic conductivity. Notably, the Pt/LSC with HOPI exhibits significantly less electrode resistance than with D2020, suggesting enhanced charge transfer facilitated by the HOPI ionomer. This could be due to better ionomer-catalyst interactions with Pt/LSC, leading to more efficient charge transfer processes.

8 Scale-up of HOPI Pt/LSC Cathodes and Durability Testing (Task 3)

This section reports the initial scale-up study performed at Ballard, using a Pt/LSC catalyst. The CCM fabrication and evaluation at Ballard uses their equipment for larger-scale MEA fabrication and testing. This scaled-up fabrication process enabled the team to produce results reflecting expected performance if HOPI is implemented by industry. The scale-up fabrication also enabled testing of various loadings and large r format MEAs. Whereas CMU used a 5 cm^2 cell, Ballard uses a custom 45 cm^2 differential cell. The MEAs prepared by CMU and Ballard both used and I/C of 0.61. Figure 1 highlights the parametric study performed by Ballard using the baseline D2020 and TKK EA50 Pt/Vulcan catalyst (Pt/LSC). The studies included a parametric analysis of loading and temperature and the characterization of optimal temperature and relative humidity (RH). The D2020 and NDP 5006 HOPI were used to fabricate MEAs at Ballard and testing in their roughly 50 cm^2 cell hardware.

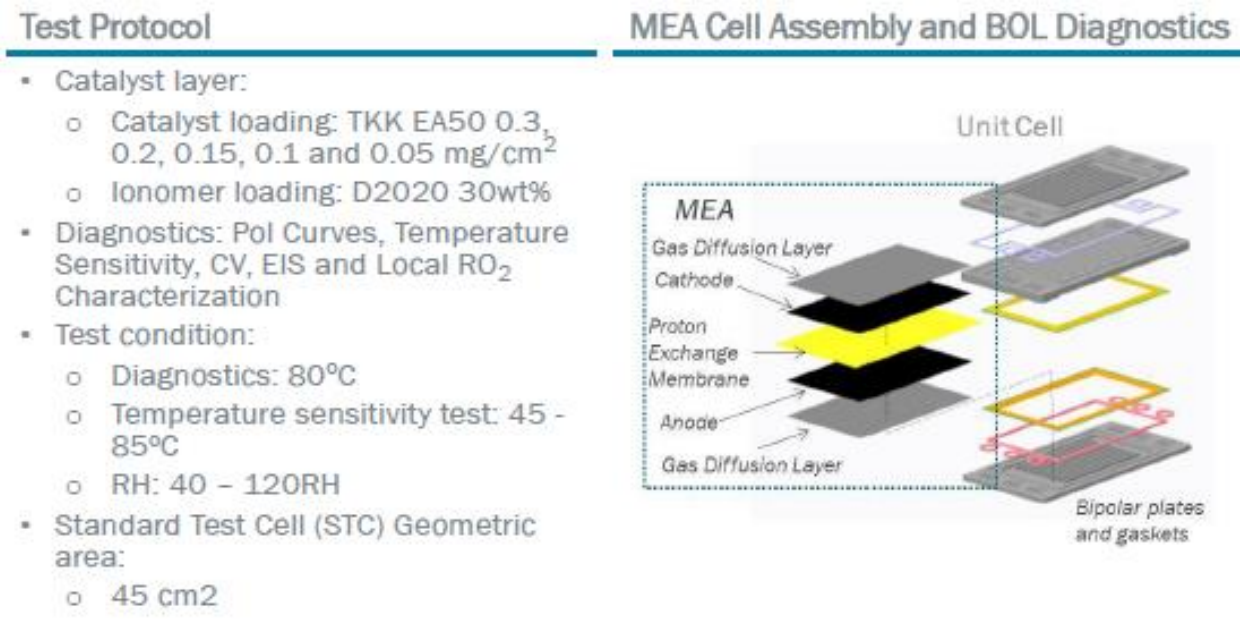

Figure 1. Protocol, test conditions, and hardware used by Ballard.

Figure 2 shows the roughness factor (ratio of Pt surface area to electrode area) versus loading. The plot shows the expected linear scaling, with D2020 and the HOPI yielding similar electrochemical activity surface areas for a given Pt loading. Given the more fundamental importance of roughness factor (*rf*) to the HOPI performance, many results are presented in terms of roughness factor rather than loading.

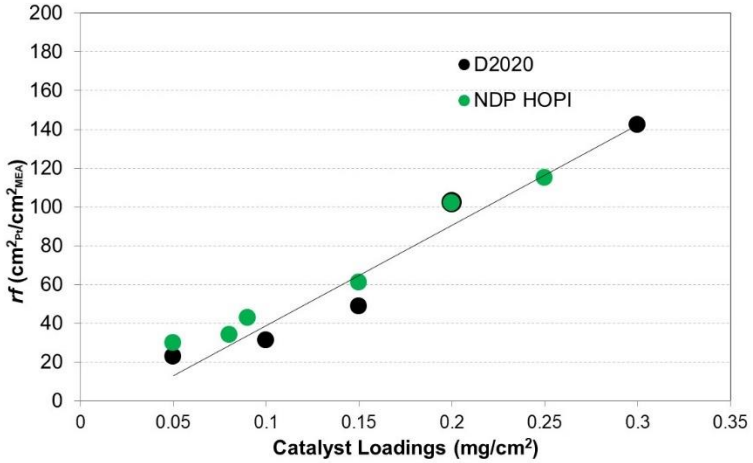

Figure 2. HOPI and D2020 cathode roughness factors versus Pt loading.

Figure 3 shows results from testing the MEAs at 80ºC and 250 kPa (1.5 barg) with high and low relative humidity (RH). The MEAs with 0.2 mg Pt/cm^2 are compared and the D2020 0.1 mg Pt/cm^2 MEA is compared with the 0.05 mg Pt/cm^2 HOPI because of their similar roughness factor. The results are consistent with the small-scale HOPI testing at CMU from last quarter, where the HOPI shows increased performance over the entire polarization curve. There is a significant increase in current density even at high voltages, indicating a clear increase in mass activity (>60% in CMU's evaluation) and fuel cell efficiency with the HOPI. In addition, the HOPI cathode with a 0.05 mg Pt/cm^2 loading significantly outperforms the D2020 cathode despite the D2020 cathode having twice the Pt loading. The improvements in oxygen mass transport are evident when comparing the lower loadings at 100% RH. The consistent and large increase in mass activity with the HOPI is a very promising result, highly relevant to the efficiency increases required for heavy duty fuel cell trucks.

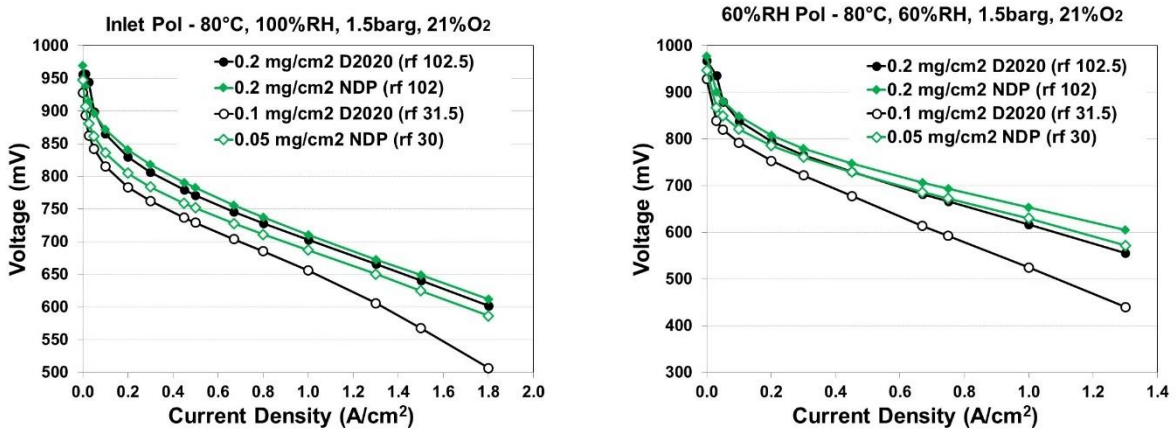

(a) (b)

Figure 3. Polarization curves for the D2020 and HOPI cathodes at 100% RH (a) and 60% RH (b). The 0.1 mg Pt/cm^2 D2020 cathode is compared to the 0.05 Pt/cm^2 NDP HOPI cathode because of the similar roughness factor.

Figure 4a shows that at loadings below 0.2 mg Pt/cm^2 the HOPI electrode has the same cathode protonic resistance as the D2020 electrode. There is a divergence between the HOPI and D2020 at higher than 0.2 mg Pt/cm^2, which is attributed to the increasing crack density with HOPI at higher Pt loadings (Figure 4b), which is one of the issues this project addressed in later work.

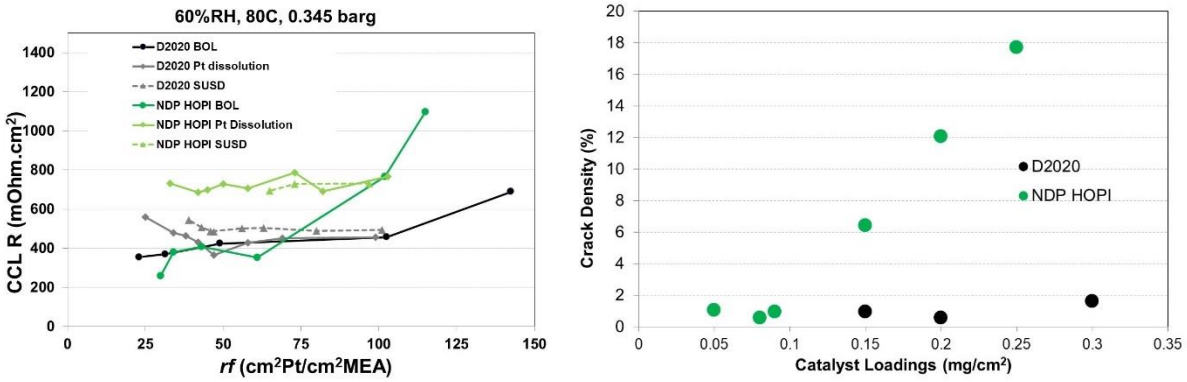

(a) (b)

Figure 4. Cathode protonic resistance versus roughness factor (a) and cathode crack density versus loading (b).

Figure 5a shows the pressure independent oxygen transport resistances extracted from measurements of limiting currents at varying pressure versus the electrode roughness factor. The pressure independent resistance largely reflects the diffusion through the ionomer films, but there is also a contribution from the small pores of the microporous layer and catalyst layer due to Knudsen diffusion as well as permeation through liquid

water. The rate of change of this resistance with respect to the roughness factor yields an estimate of the local resistance at the Pt-ionomer interface. The plot shows the substantial, roughly 50%, reduction in the pressure independent resistance with the HOPI versus D2020 when comparing the BOL values. Figure 5b compares the voltage at 1 A/cm^2 and 60% RH between the D2020 and HOPI as a function of the roughness factor. At higher loadings, the voltage increase is approximately 40 mV, whereas at low loadings/roughness factors, the voltage increase is >100 mV, which entails 20% higher efficiency and power density at 1 A/cm^2.

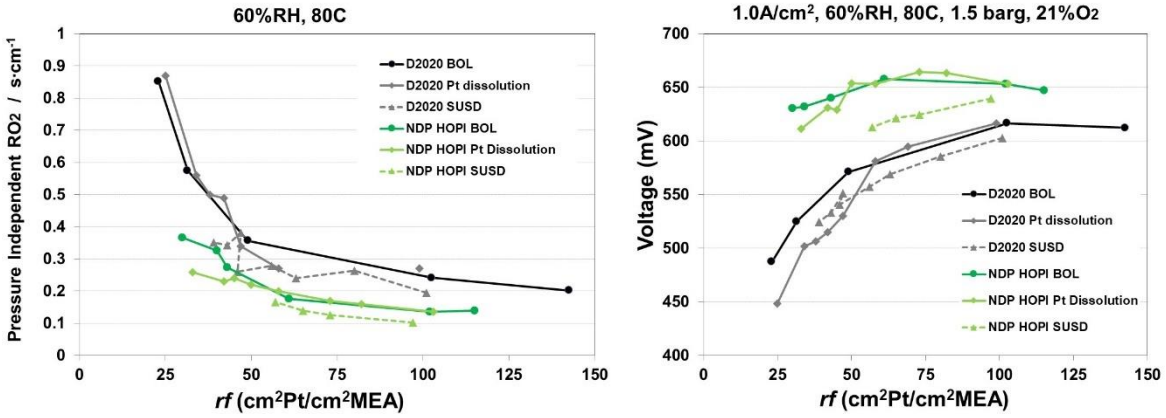

(a) (b)

Figure 5. Cathode pressure independent O_2 transport resistance (a) and cell voltage at 1.0 A/cm^2 (b) versus roughness factor at 60% RH.

Figure 6 shows the local oxygen transport resistances extracted from the relationship between the pressure independent resistance and the roughness factor. These results come from both the loading study above to vary roughness factor as well as durability studies that used a Pt dissolution AST and a startup/shutdown (SUSD) carbon corrosion AST to incrementally reduce the roughness factor of MEAs. The results are for 60% RH; evaluations at 100% RH yield even lower resistances. At 60% RH, the HOPI met the Budget Period 1 Go/No Go Decision Point goal of 9.0 s/cm, whereas with D2020 it is almost 100% higher at 16 s/cm. For reference, General Motors' application of this local oxygen transport analysis method on Pt/Vulan catalyst yielded a local oxygen transport resistance of 12 s/cm at 60% RH. Thus, the Ballard methodology and measurements are conservative and not under-estimating the resistance. At 100% RH, the local resistance with the HOPI is 5.8 s/cm, whereas with the D2020 it is 7.2 s/cm. The local resistance based on roughness factor reduction by ASTs shows even lower oxygen transport resistances when using the HOPI.

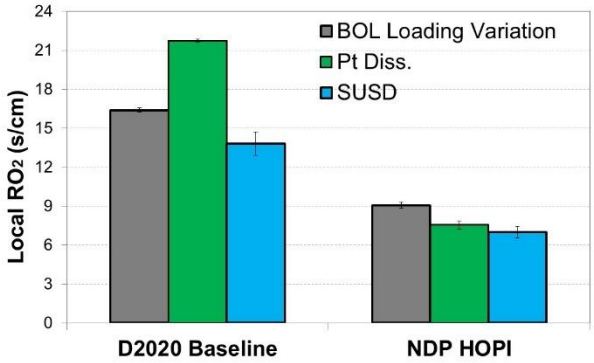

Figure 6. The local Pt oxygen transport resistance for D2020 and HOPI at 60% RH based on roughness factor variations by a loading study and two ASTs.

In addition to polarization curve measurements, Ballard performed durability assessments in the form of a Pt dissolution AST and carbon corrosion focused start-up/shutdown AST. Separate MEAs with 0.2 mg Pt/cm^2 loadings were prepared for these studies. Figure 7a compares the D2020 and HOPI voltage at 1.0 A/cm^2 versus AST cycle number at both 60% and 100% RH. At all cycle numbers, the HOPI MEA performs better and shows a slower degradation rate, as shown in Figure 7b. The HOPI MEAs demonstrated an average of a 70% reduction in the degradation rate during the Pt dissolution AST despite similar losses in roughness factor due to Pt surface area loss.

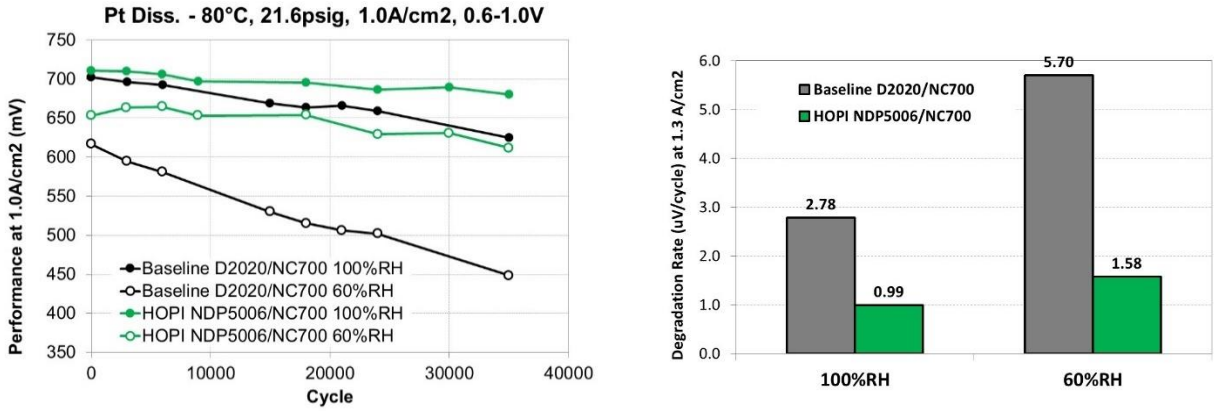

(a) (b)

Figure 7. Pt dissolution AST results. (a) Performance at 1.0 A/cm^2 for D2020 and HOPI versus AST cycle number. (b) Degradation rates after 35K AST cycles at 1.3A/cm^2.

Figure 8 shows the results of the startup/shutdown carbon corrosion AST in terms of the loss in roughness factor and the voltage at 1.0 A/cm^2. The D2020 and HOPI show similar losses in roughness factor with this AST, while the performance remains higher with the HOPI.

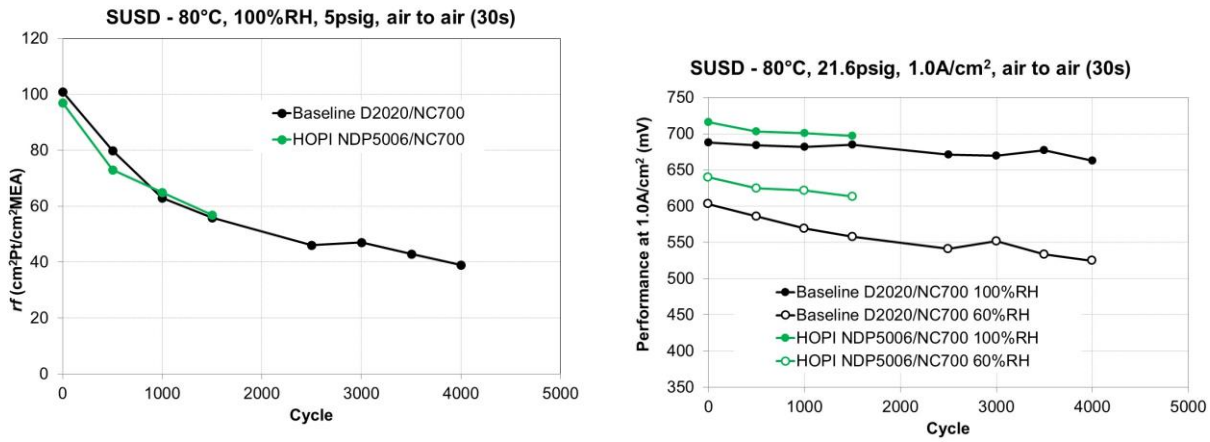

(a) (b)

Figure 8. Startup/shutdown AST results. Roughness factor (a) and performance at 1.0 A/cm2 (b) for D2020 and HOPI versus startup/shutdown AST cycle number.

The CMU group used their nano-CT to image the Ballard BOL and post-AST samples for the Pt/LSC cathodes to understand the redistribution of Pt in the AST and impact that HOPI has on the Pt dissolution and redeposition. The imaging used CMU's Xradia Ultra XRM-L200 nano-scale resolution X-ray CT. The normalized absorption contrast 3-D images of MEA samples integrated with Pt/LSAC and either D2020 ionomer or HOPI in CCLs are displayed in Figure 9. The images reveal a transfer of Pt into the membrane from the beginning of life (BOL) to the end of life (EOL), resulting in the formation of a Pt band on the cathode side of the reinforcement layer in the EOL samples.

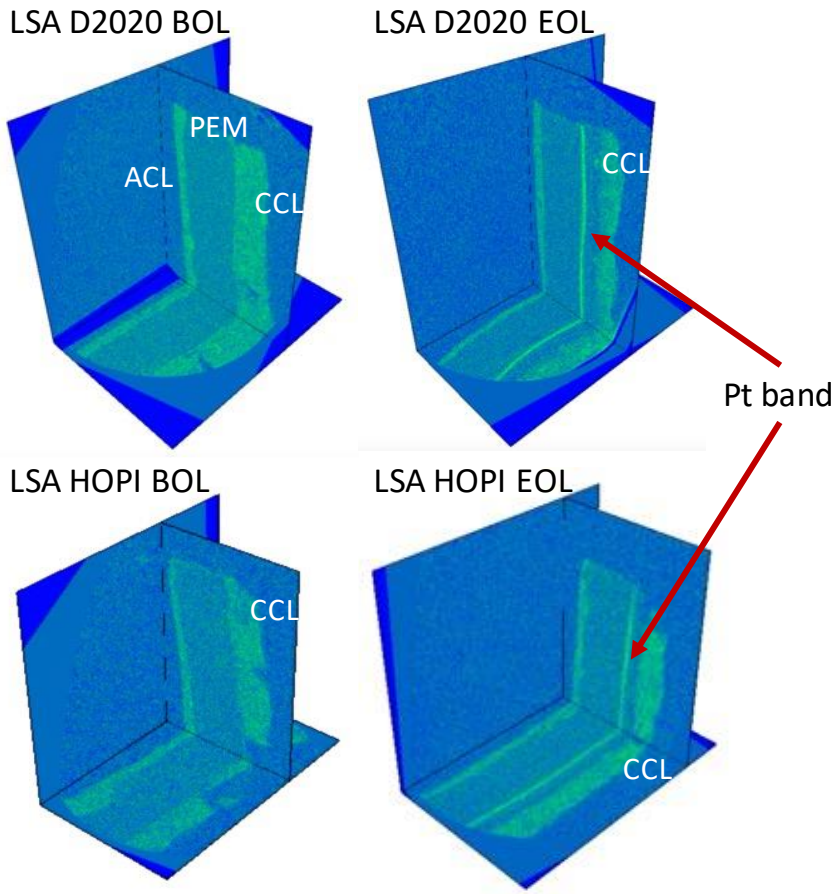

Figure 9: Normalized nano-CT absorption contrast images of the D2020 and HOPI MEAs with the Pt/LSAC catalyst before (BOL) and after (EOL) cycling.

Figure 10 shows the distribution of Pt at the BOL for the Pt/LSAC catalyst, where we see a nearly uniform Pt distribution in the cathode. After the AST, a new peak corresponding to the formation of a Pt band is observed in Figure 10b, along with the depletion of Pt in the CCL near the membrane. To quantify the Pt amount, we calculated the area under the intensity curve in the BOL cathode (A1), EOL Pt band (A2), and EOL cathode (A3) regions, as seen in Table 1. Our results demonstrate that the D2020 ionomer leads to a greater loss of Pt in the cathode, with approximately 21% less Pt being lost to the Pt band with HOPI, resulting in improved durability.

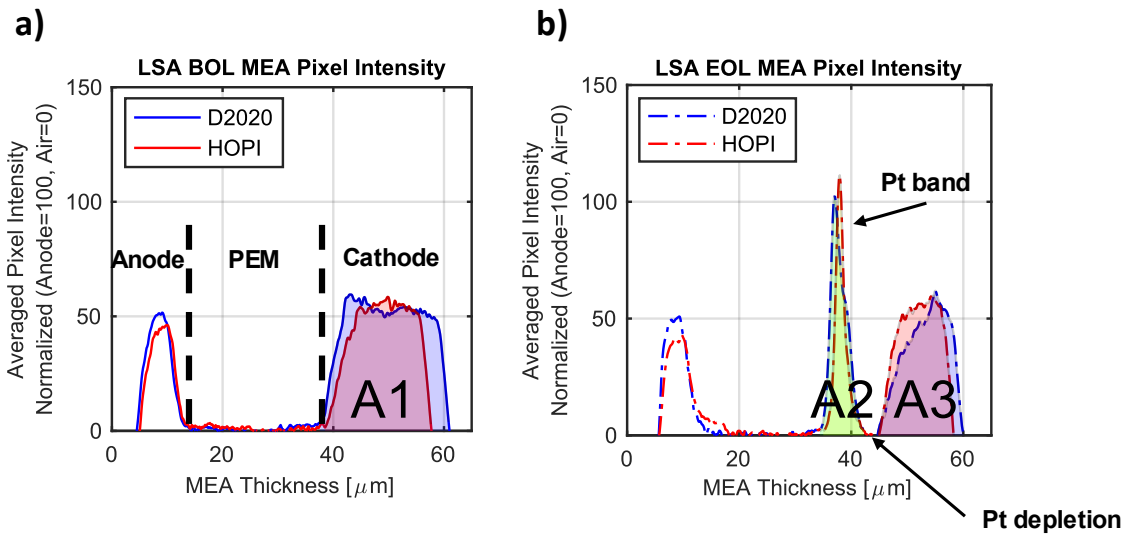

Figure 10: X-ray absorption distributions due to Pt density in MEA samples with Pt/LSAC catalyst with D2020 and HOPI at (a) BOL and (b) after a Pt dissolution AST.

Table 1: Calculations of the area under the intensity curve for various regions with Pt/LSAC catalyst.

Ionomer	BOL Cathode A1	EOL Pt Band A2	EOL Cathode A3	EOL Total Pt in Cathode A2+A3	Pt Lost A2/(A2+A3)
D2020	1070	324	564	888	36.5%
HOPI	825	231	572	803	28.8%

9 Impact of Catalyst on PEMFC Performance with Scaled-Up HOPI MEAs (Task 3)

In addition to the CMU study of Pt/LSC versus Pt/HSC, Ballard completed several studies comparing the performance and durability of HOPI-enhanced cathodes with different catalysts (Pt/LSC, Pt/HSC, and PtCo/HSC). The Pt/HSC catalyst used by Ballard was different than CMU, with Ballard using Umicore ElystPt50 0550.

Figure 1 shows the results for Ballard's testing of Pt/HSC using ionomer loadings of 23, 30, and 36 wt% at 100% relative humidity. For both the HOPI and D2020, the ionomer loading does not have a significant impact. For each ionomer, the differences in ionomer loading only yields a maximum of 15 mV difference. Figure 2 shows the same study, but when operating the cells at 60% relative humidity. In this case, the HOPI electrode shows substantially better performance with low ionomer loading than D2020. This could be a combination of the much higher O2 transport with HOPI at low relative humidity, as well as the higher conductivity of the lower EW HOPI.

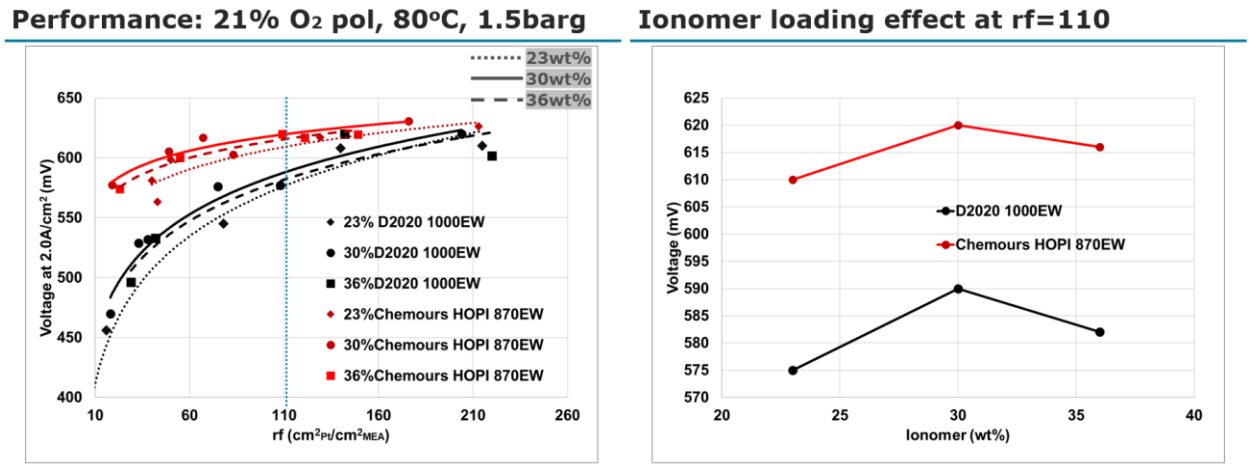

Figure 1. Impact of ionomer loading on performance at 100% RH with Pt/HSC catalyst.

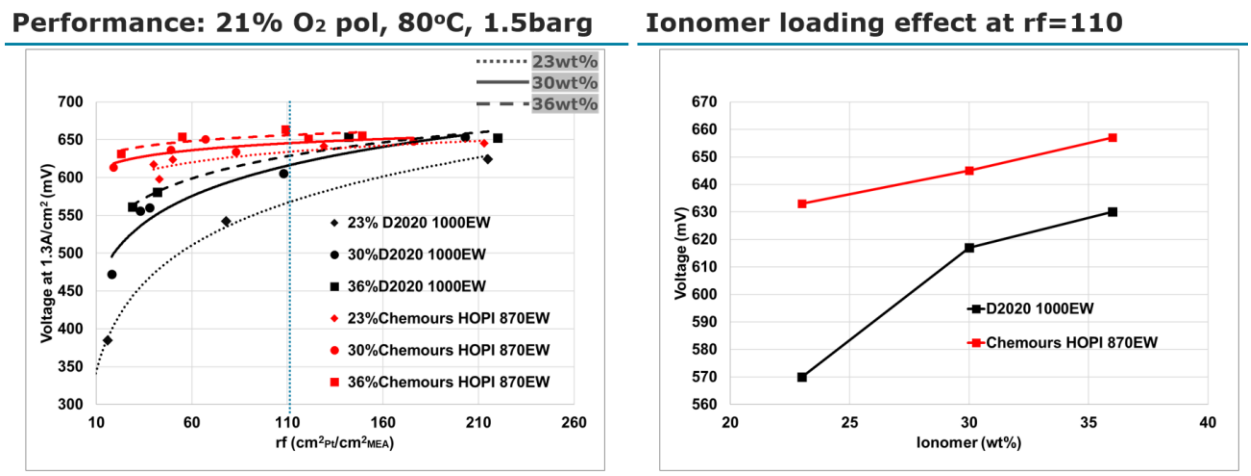

Figure 2. Impact of ionomer loading on performance at 60% RH with Pt/HSC catalyst.

Figure 3 shows the results of startup/shutdown testing of D2020 and HOPI. The cells went through 2000 SUSD cycles that target cathode carbon corrosion. As the left-side plot of Figure 3 shows, the HOPI and D2020 electrodes show the same trends and magnitudes of roughness factor loss. Thus, the ionomer does not seem to affect the catalyst degradation. This is similar to Pt dissolution AST results. However, as the right-side plot shows, the HOPI significantly reduces the impact of the catalyst degradation. This plot also shows the fuel cell performance versus the roughness factor as it reduced throughout the AST. For a given roughness factor, the HOPI yielded significantly higher voltages at 1.5 A/cm^2. The difference becomes >200 mV towards the end of the ASTs.

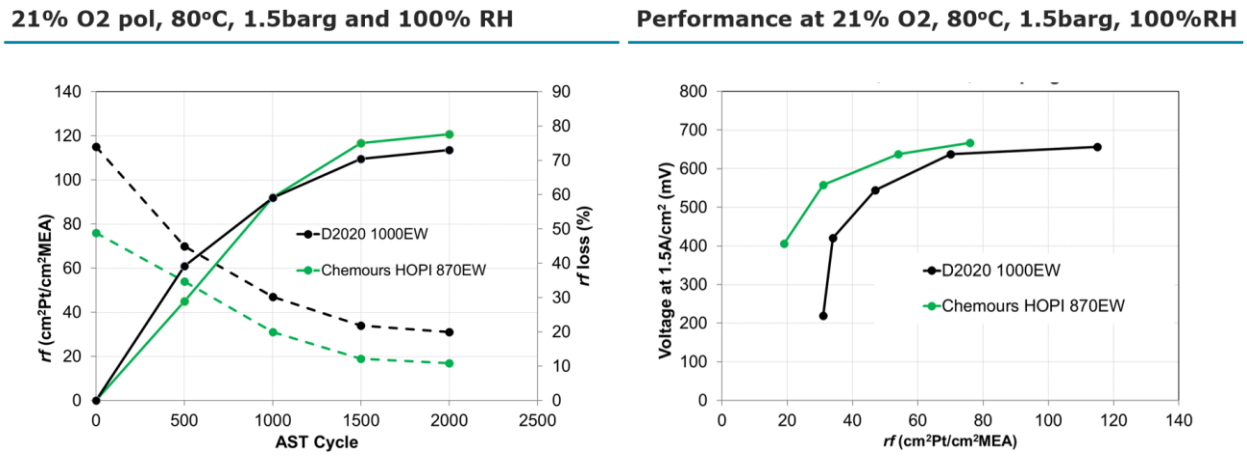

Figure 3. Startup/shutdown AST testing of Pt/HSC catalyst with D2020 and HOPI. The Pt/HSC loading was 0.2 mgPt/cm^2 and 30 wt% ionomer loading.

Ballard also completed the evaluation of HOPI's impact on the performance of PtCo/HSC catalyst. As Figure 4 shows, the HOPI yielded an increased performance, but it was less of an increase compared to that for Pt/LSAC and Pt/HSC. At low roughness factors, the high current density voltage was significantly increased using HOPI for PtCo/HSC. At low current density, the highest voltages were obtained with HOPI using the PtCo/HSC catalyst. However, at high current density, the highest voltages were obtained with the Pt/HSC catalyst with HOPI. At the higher roughness factors, the reduction in the non-Fickian oxygen transport resistance was less with PtCo/HSC than Pt/HSC, which may be the reason for the reduced performance enhancement with HOPI for PtCo/HSC.

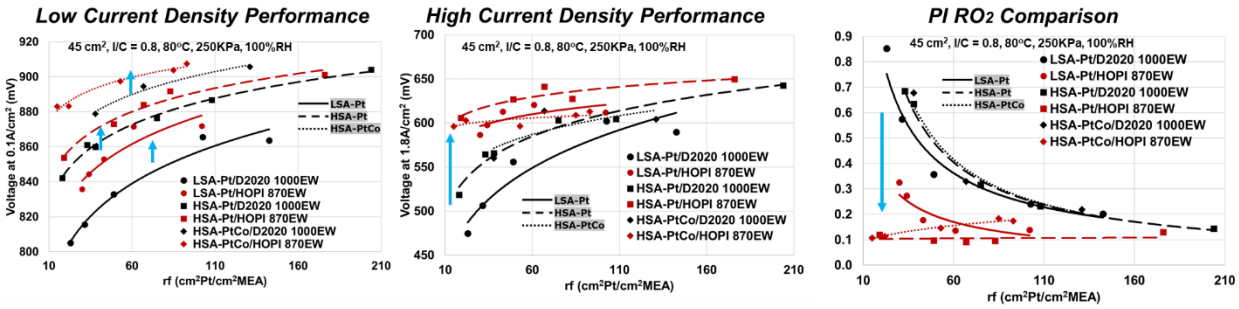

a) b) c)

Figure 4. Effect of catalyst for Pt/LSAC, Pt/HSC, and PtCo/HSC for HOPI and D2020.

Figure 5 shows the impact of the catalyst type on the degradation rate. The plots show the previously reported significant reductions in the degradation rate for Pt/LSAC and Pt/HSC catalysts despite similar ECSA losses. This lower performance degradation rate has been attributed to the higher specific activity and lower local oxygen transport resistance with HOPI. For PtCo/HSC, there was significant 23% reduction in the degradation rate at 0.1 A/cm^2. However, at the higher 1 A/cm^2 point, the degradation rate was higher with HOPI than for D2020. This difference may be attributed to the higher crack density with HOPI or additional polarization effects due to dissolved Co^{2+}.

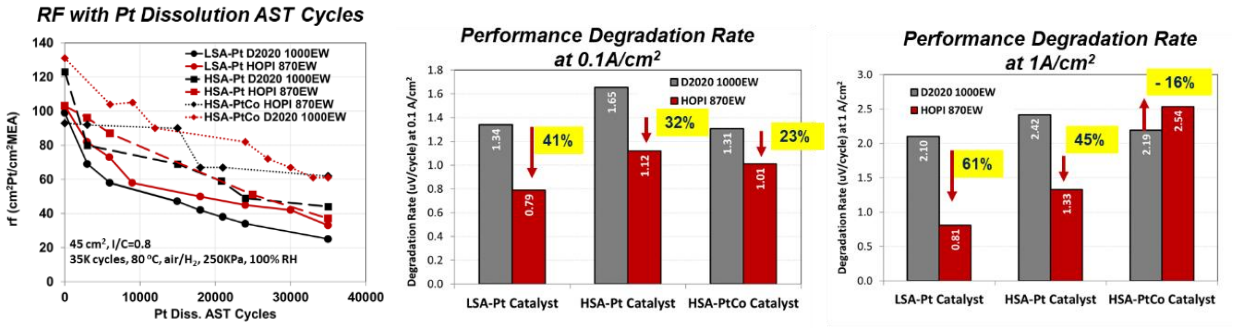

a) b) c)

Figure 5. Degradation comparison for different catalysts. a) Roughness factor versus Pt dissolution AST cycles, b) degradation rate at 0.1 A/cm^2, and c) degradation rate at 1 A/cm^2.

10 Electrode Ionomer Stability AST (Task 4)

CMU developed and performed an ionomer AST to determine if HOPI exhibited any problematic chemical stability challenges. The preliminary AST follows from the typical membrane chemical AST of holding the cell at OCV at elevated temperature and low relative humidity, while also minimizing characterization steps that would degrade the catalyst and confound the analysis of ionomer degration. In this case, the OCV condition during the AST was held for 130 hr at 90°C with a relative humidity of 30%. A higher than typical loading for this project of 0.4 mg_{Pt}/cm^2 (TKK Pt/HSC) was used and improved the quality of electrode H+ resistance measurement by EIS. The AST was performed on cathodes made with both D2020 and HOPI.

Figure 1 shows the polarization curves, electrode resistance, and the pressure-independent oxygen transport resistance as measured by a limiting current study. The polarization curves show no additional degradation in performance versus the durable D2020 standard. It is worth noting that at these high loadings, the benefits of HOPI are minimized relative to D2020. Figure 1 also shows the N_2/H_2 Nyquist plots for HOPI and D2020 cathodes before and after the AST. The shift of the Nyquist plots transitions from 45 degrees to vertical to lower real impedance indicates similarly increased conductivity for both HOPI and D2020, indicating no problematic loss of conductivity for both ionomers. Figure 1 further shows the change in the pressure-independent oxygen transport resistance, which is typically attributed to the local resistance of the ionomer at the Pt interface. The results show that there is no increase oxygen transport for HOPI and it remains significantly lower than that of D2020, particularly at low relative humidity. To summarize, this testing has shown that the current HOPI has the same stability as the standard D2020 and exhibits no loss of function during this preliminary AST.

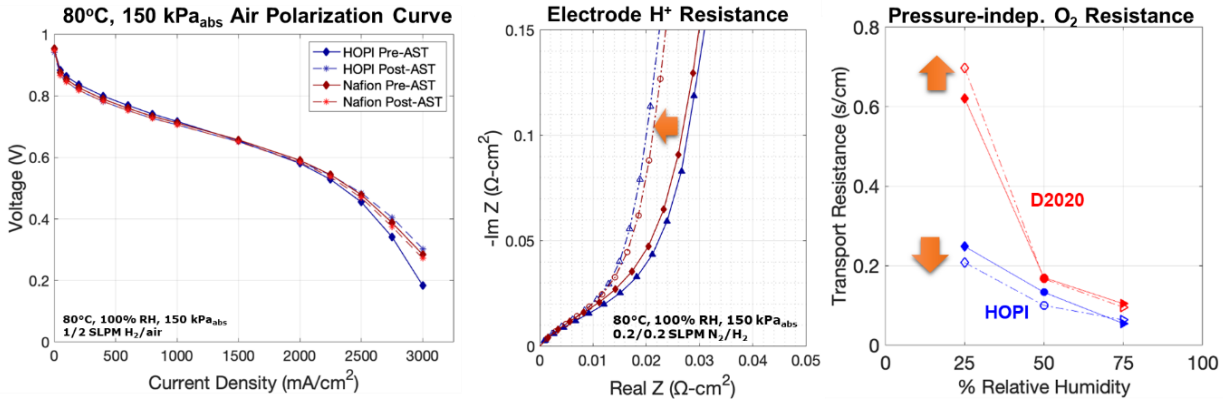

Figure 1: Results of the ionomer AST – polarization curves, N2/H2 Nyquist plots, and pressure independent oxygen transport resistance.

11 Evaluation of HOPI Chemistry Variation on Performance and Durability (Tasks 3 & 4)

Over the course of the project, HOPIs with varying chemistry (A, B, and C) and EW were delivered to CMU and Ballard for evaluation. Figure 1 shows the results from Ballard in testing a higher EW variant of the HOPI A chemistry (1036 EW vs. 870 EW). Overall, the 1036 EW HOPI exhibited lower performance across the polarization curve. This lower performance is likely attributable to the similar oxygen transport resistance of D2020 (1000 EW) but the substantially higher proton conduction resistance.

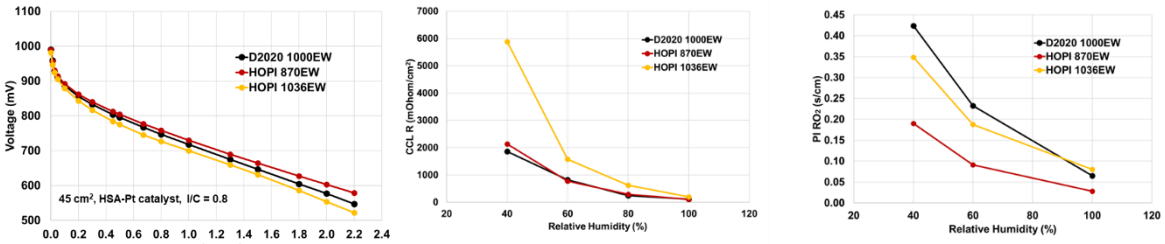

a) b) c)

Figure 1: Evaluation of HOPI with 1036 EW vs. 870 EW HOPI and D2020. a) Polarization curves, b) proton conduction resistance, and c) pressure-independent oxygen transport resistance.

Ballard evaluated a promising alternative HOPI chemistry 'HOPI B' using the Pt/HSC catalyst. Figure 2 shows the catalyst layer properties relevant to the ionomer. Figure 2a shows the catalyst layer resistance for proton transport across the cathode, where the new HOPI B chemistry presents a lower resistance than other variants and the D2020 baseline – even with the lower I/C of 0.6. Figure 2b shows pressure independent resistance that primarily reflects the oxygen transport across the ionomer, but also within primary particles and across the MPL and catalyst layer. The results indicate a slightly higher resistance than HOPI A, but still a substantial reduction versus the D2020 PFSA baseline.

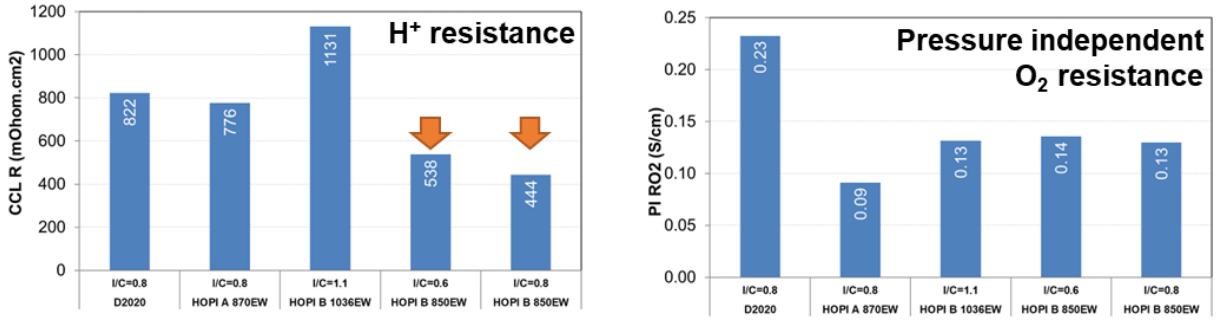

a) b)

Figure 2. HOPI B catalyst layer properties comparison with other ionomers. (a) Cathode catalyst layer proton conduction resistance. (b) Pressure independent oxygen transport resistance.

Ballard evaluated the performance and durability of cathodes with HOPI B having EWs of 850 and 1036 EW and variation of I/C (0.6 and 0.8). Figure 3a shows the air polarization curves for D2020 and the HOPI variants. Although the HOPI A shows slightly higher currents and activity at voltages above 0.9 V, below voltages of 0.8 V, the HOPI B variant with a lower I/C of 0.6 matches or outperforms the HOPI A MEA with an optimized I/C of 0.8. Likewise, Figure 3b shows that the HOPI B variant shows the same trend as HOPI A when evaluating the voltage at 2 A/cm^2 versus roughness factor (i.e., Pt loading). The voltages match the best HOPI A performance and shows the substantial increase in voltage versus D2020 as the roughness factor is reduced. The enhanced performance with HOPI B versus D2020 or HOPI A with optimized I/C ratios is summarized in Figure 10, which plots the voltage at 1.3 A/cm2 versus roughness factor.

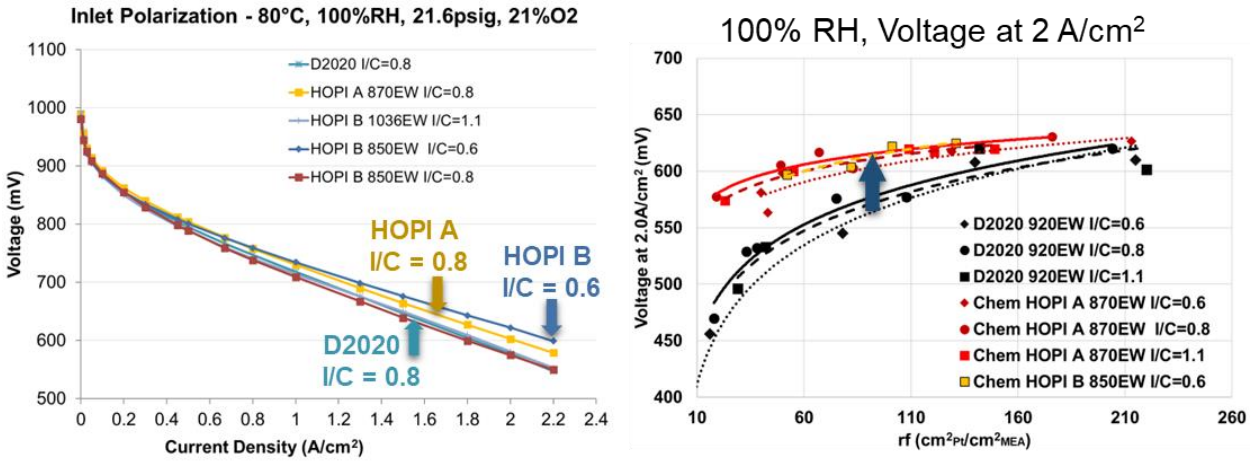

a) b)

Figure 3. HOPI B performance comparison. (a) Air polarization curves . (b) Voltage at 2 A/cm^2 versus roughness factor.

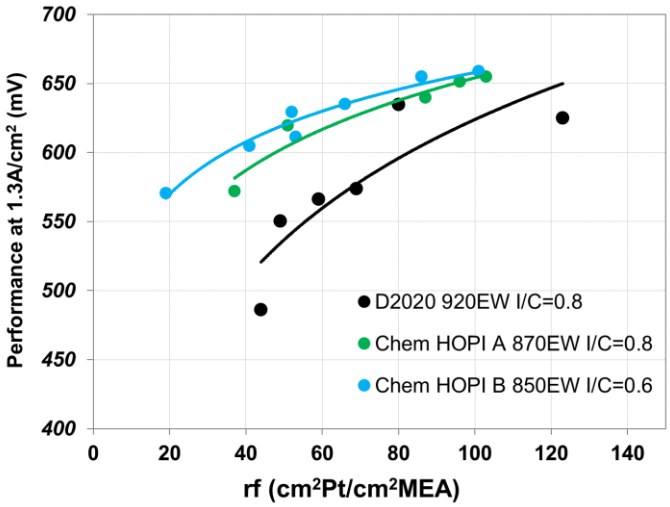

Figure 10. Comparison of optimized D2020, HOPI A, and HOPI B cathodes based on voltage at 1.3 A/cm^2 versus roughness factor.

Figure 11 shows the results of the Pt dissolution AST for D2020, HOPI A, and HOPI B. As Figure 11a shows, the rate of loss in roughness factor between HOPI A and HOPI B is very similar across all numbers of dissolution cycles, but both HOPI A and B do not show the initial large loss in roughness factor exhibited by D2020. After 10,000 cycles, the rate of roughness factor loss is similar between the HOPIs and D2020. Figure 10b shows the voltage loss versus dissolution cycles, where HOPI B shows a similar low degradation rate relative to D2020 as HOPI previously demonstrated. Specifically, HOPI A showed a 48% reduction in the performance (i.e., voltage) degradation rate, while HOPI B showed a still significant 38% reduction.

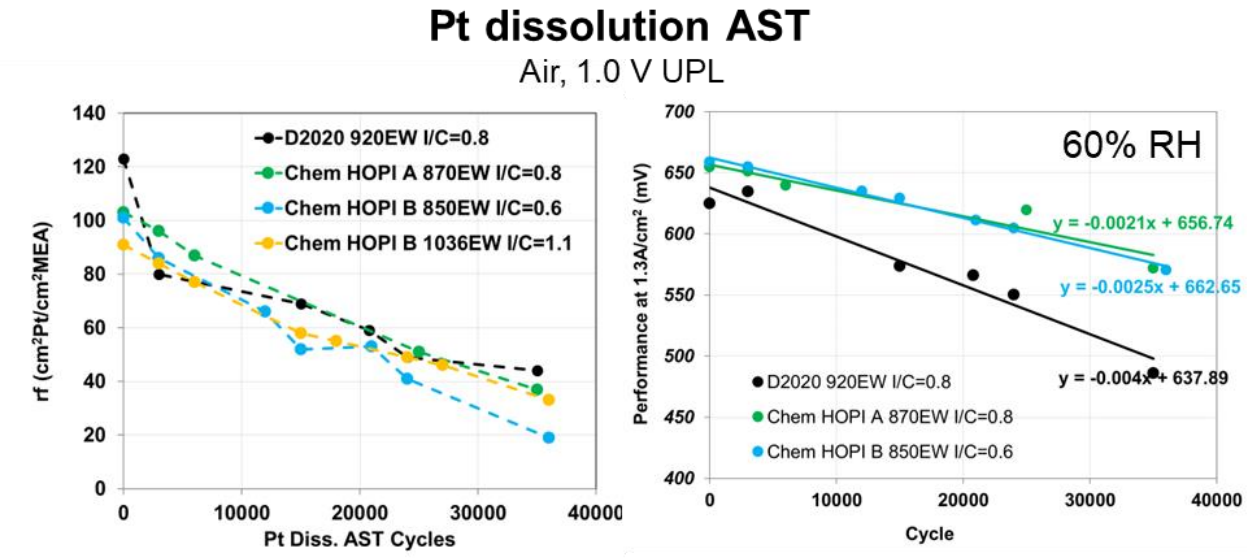

a) b)

Figure 11. Pt dissolution AST results with 1.0 V UPL with air for D2020, HOPI A, and HOPI B. a) Roughness factor versus dissolution cycles. b) Voltage at 1.3 A/cm2 versus dissolution cycles.

Chemours prepared several additional variants of HOPI and delivered them to Ballard for evaluation. One was a HOPI A chemistry of 788EW and two other were HOPI B chemistry with 876 and 925 EW. In comparison to D2020 baseline, both 788EW HOPI A and 876EW HOPI B variants showed:

1. Improvement in proton and oxygen transport properties (Figure 12a) and
2. Improvement of performance in higher loading (Figure 12b) (close to 0.2 mg/cm^2); however, the performance collapses toward the D2020 performance at lower catalyst loadings, potentially due to water sensitivity as evident in RH sensitivity testing.

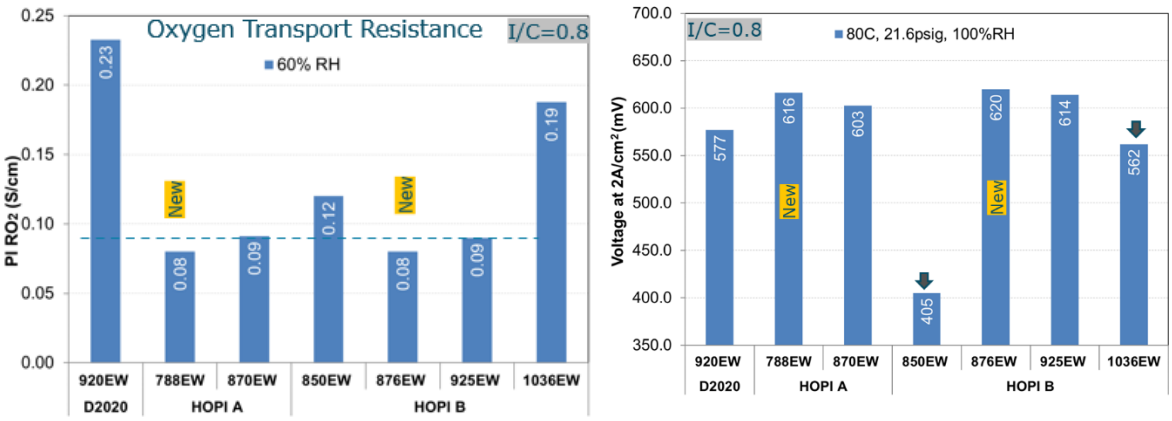

a) b)

Figure 12: Evaluation of ionomer pressure independent oxygen transport resistance (a) and effect of ionomer on fuel cell voltage at 2 A/cm^2 (b) for 0.2 mg Pt/cm^2 loading with Pt/HSC catalyst.

Ballard completed the durability testing of the HOPI A chemistry of 788 EW and the HOPI B chemistry with 876 and 925 EW. As Figure 13 shows, the HOPI A 788 EW cathode showed degradation rates similar to D2020 in the Pt dissolution AST. Nevertheless, it's absolute performance was superior to D2020 throughout the AST in low RH conditions. The HOPI B with 876 EW showed a degradation rate similar to other variants of promise. The HOPI A 870 EW ionomer remained the top candidate when considering both performance and durability.

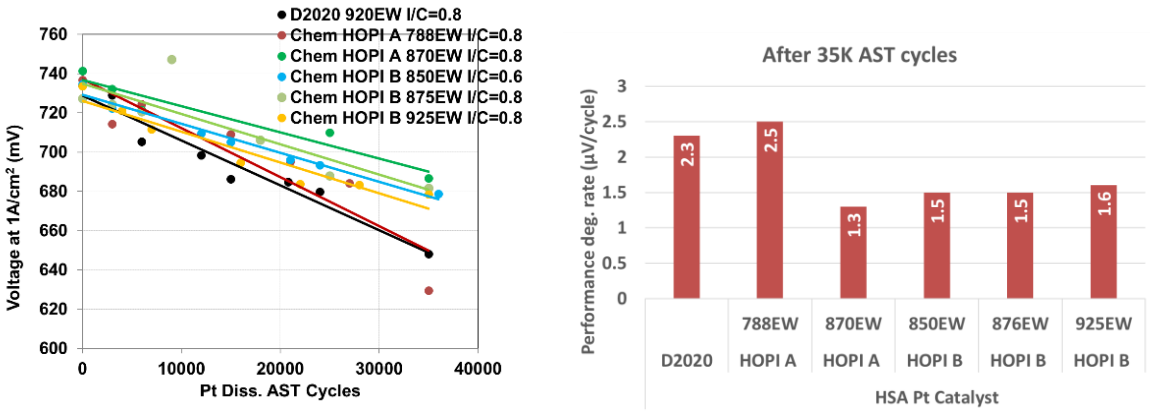

Figure 13. Results of the Pt dissolution AST for 100% relative humidity operation.

Figure 14 illustrates the generalized findings for the impact of the HOPI EW on the degradation rate at 1 A/cm^2. The results in the plot include that of D2020, but also HOPI A, B, and C. The results show the somewhat general result that for both high and moderate relative humidity the optimum EW is in the 850-900 range.

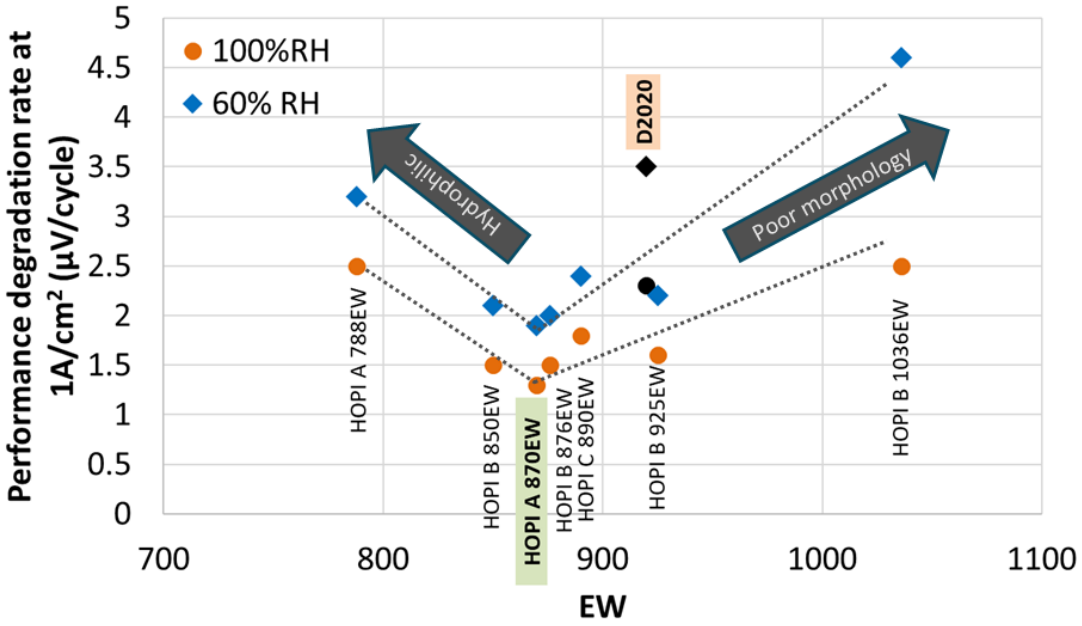

Figure 14. Effect of EW for different HOPIs on performance degradation rate.

12 Model-Based Estimation of HOPI Impact on Lifetime (Task 4)

During the project, the impact of HOPI on PEFC lifetime was evaluated by both CMU and Ballard using model-based approaches, utilizing performance and AST data. CMU evaluated the Pt/LSC cathodes and Ballard performed their evaluations for the Pt/HSC cathodes.

The increased lifetime of the HOPI-enhanced cathode with the Pt/LSC catalysts was evaluated using CMUs MEA model using the rate of platinum surface area loss [i.e., roughness factor (RF)] determined through ASTs at Ballard. The model has been validated for its performance prediction of Pt loading effect, loss of Pt surface area, and HOPI versus D2020 cathode ionomer. In this process, the only fitted parameters were the Pt-area specific exchange current density and the fuel cell Ohmic contact resistance. Those fitted values were kept constant for all simulations presented and individual cases were not fitted. Figure 1 shows that the model accurately predicted the impact of loading for D2020 (Figure 1a) and HOPI (Figure 1b) between roughness factors of 30 (~0.05 mg Pt/cm^2) and 100 (~0.2 mg Pt/cm^2). The impact of HOPI is simulated based on the 3X increase of permeability of the HOPI and an equal balance of 73% increase in solubility and 73% increase in diffusivity of the ionomer film. Figure 1c shows that this approximation accurately captures the increased performance with HOPI.

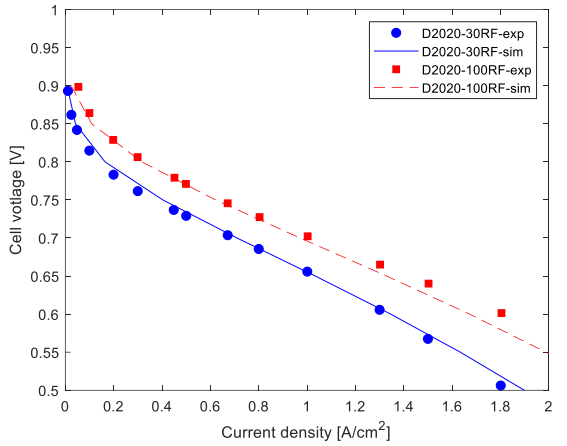

a.

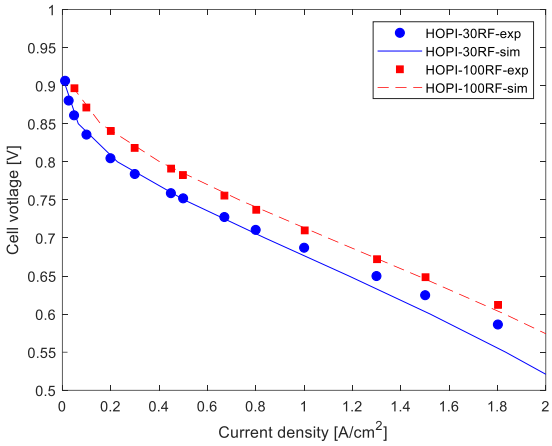

b.

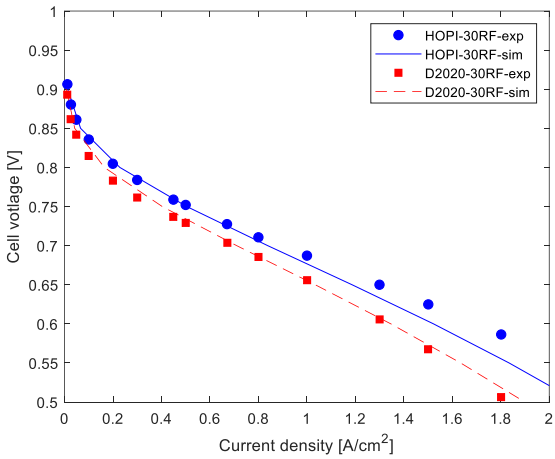

c.

Figure 1. Validation of BOL performance modeling between Ballard result and CMU model for two roughness factors (i.e., loading) of 30 and 100 and the two ionomers: a) D2020 and b) HOPI. c) Experimental and modeled performance increase with HOPI over D2020 for a RF of 30.

Figure 2 shows the model results from the two types of AST performed by Ballard. Figure 2a shows the results of the catalyst Pt dissolution AST for D2020 and HOPI with an RF of 100. The plot also shows the double exponential fits to the degradation, all with R^2 values >0.98. In the Pt dissolution AST, there is an initial quick loss of RF and then a slow decline. The results show that the percent loss of RF is similar in trend between D2020 and HOPI, but the HOPI shows a slower loss of RF, especially over the first 500 cycles of the AST. The carbon corrosion startup/shutdown (SU/SD) AST results in Figure 2a show a much more similar degradation rates and loss of RF for the two ionomers, with the HOPI showing a marginally slower loss of RF. At the end of the experimental Pt dissolution ASTs in Figure 2a, the D2020 cathode had 26% of the BOL RF remaining and the HOPI cathode had 32% of its BOL RF remaining.

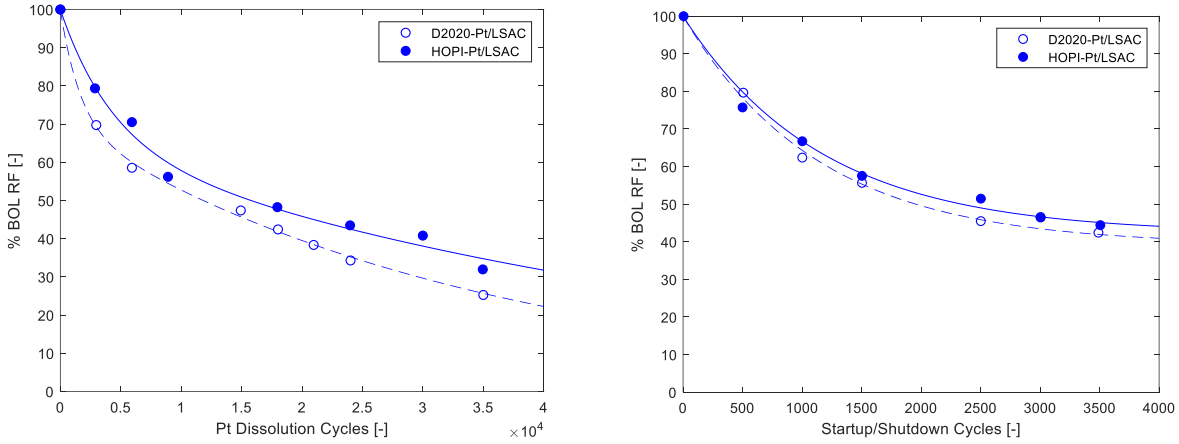

a. b.

Figure 2. Ballard data and CMU fitting to percent RF loss during the a) Pt dissolution AST and b) the SUSD AST. The solid and dashed lines are the fits to the data the HOPI and D2020 data, respectively.

Figure 3 shows the experimental and model BOL and EOL polarization curves for this AST. The experimental results show the significantly greater loss in performance with D2020 following the AST. The lines in the plot are modeled predictions of the polarization curves, where the EOL simulation used a uniform reduction in the Pt surface area based on the 26% and 32% remaining RF from the experimental AST. The simulation results show good agreement, especially for the HOPI cathode. However, the simulation underestimates the loss of D2020 performance at currents >1 A/cm^2. The origin of that difference has not yet been resolved. In any case, the resulting outcome is the forecasting of an increased lifetime with HOPI over D2020 will be underestimated for high current density performance. Thus, the lifetime estimates provided here using the model are conservative.

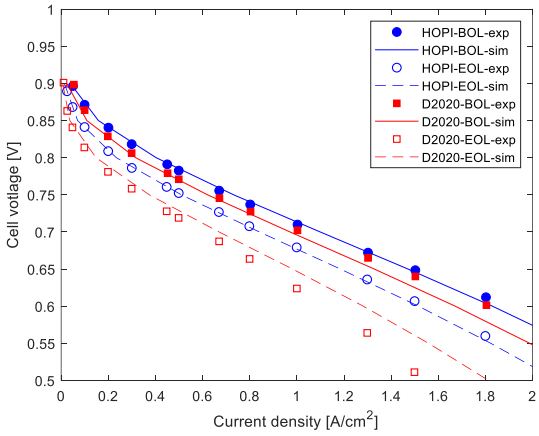

Figure 3. Comparison of BOL and EOL performance between Ballard result and CMU modeling for the Pt dissolution AST and the two ionomers.

Figure 4 shows the estimation of the increased lifetime based on the time to reach the power density equal to a 10% loss from the D2020 BOL power density at 0.7 V. For D2020 this is a decrease from 0.68 W/cm^2 to 0.61 W/cm^2. Figure 4a shows the difference in the RF loss for HOPI versus D2020 based on the fits in Figure 2a. For example, the plots show that when D2020 has incurred a 20% RF loss due to Pt dissolution, the HOPI electrode has only lost 11%. Figure 4b shows the power density at 0.7 V for the two electrodes as a function of the percent RF they have lost. The plot shows that the EOL power density of 0.61 W/cm^2 can be met by the HOPI cathode with roughly twice the roughness factor loss, showing that the HOPI enables a significantly larger amount of catalyst degradation while still meeting power requirements.

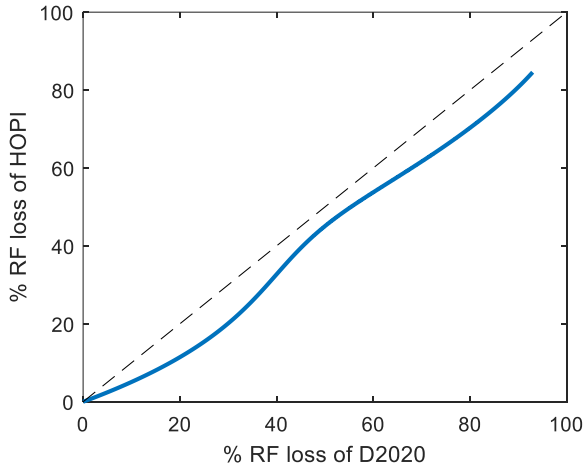

a.

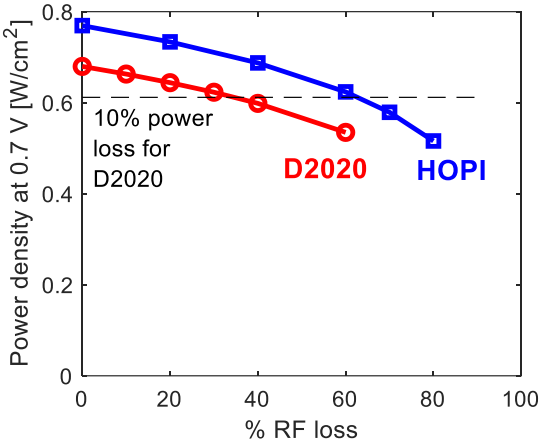

b.

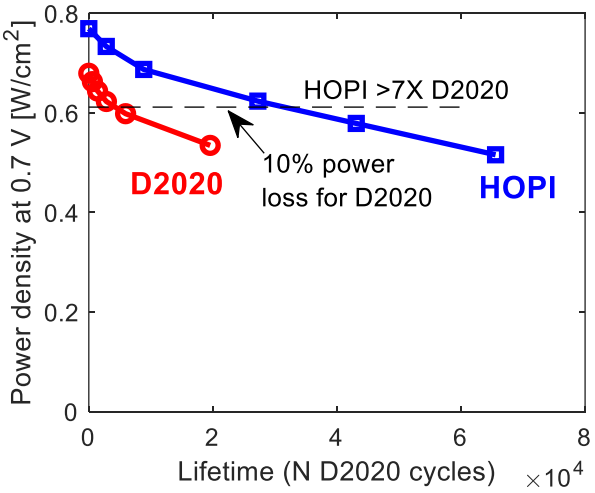

c.

Figure 4. a) Percent loss of HOPI RF versus RF loss of D2020 for the same number of Pt dissolution AST cycles. The dashed indicates equal RF loss and the reduced RF loss per cycle with HOPI versus D2020. b) Power density at 0.7 V versus percent loss of RF for

D2020 and HOPI. c) Power density at 0.7 V versus number of AST cycles that is equivalent to operational lifetime.

Figure 4c shows the 0.7 V power density for the two cathodes versus the number of Pt dissolution cycles that would scale approximately with the operational lifetime of the fuel cell and is used as a proxy for operating hours in this analysis. As Figure 5c shows, the HOPI-enhanced extends the lifetime by a factor of 7.4X based on time for the power density to decrease to 90% of the D2020 BOL level. Thus, the Go/No Go decision point of a 2X increase has been substantially exceeded.

Pt/HSC Lifetime Enhancement with HOPI by Ballard AST and Forecasting

In a separate analysis, Ballard evaluated the lifetime performance of the Pt/HSC electrodes using inputs from their ASTs and their lifetime performance forecasting models. Figure 5 shows the Ballard COMSOL APOLLO model predictions of the BOL performance for two Pt loadings (0.3 mg/cm^2 and 0.05 mg/cm^2). The model incorporates two interfacial resistances, one at the ionomer-gas interface and one at the Pt-ionomer interface. The comparisons with the model show good agreement.

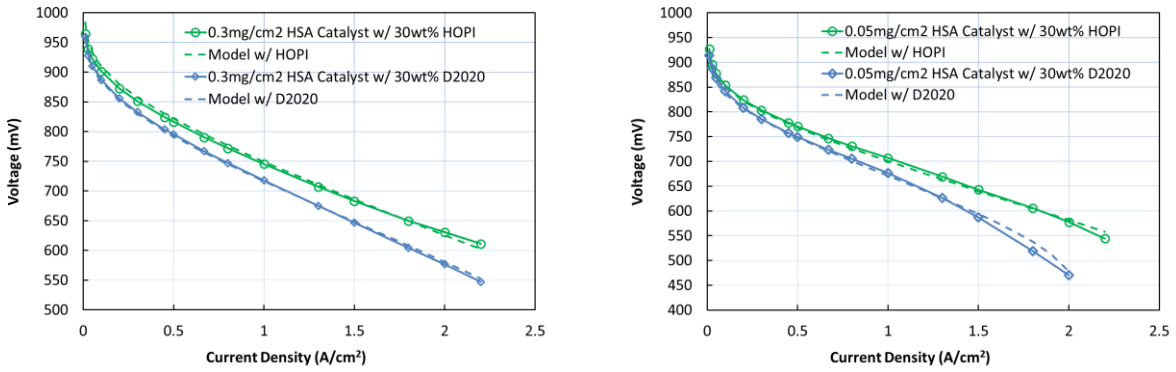

a. b.

Figure 5. Ballard modeling of the Pt/HSC cathodes with D2020 and HOPI ionomer for Pt loadings of a) 0.3 mg/cm^2 and b) 0.05 mg/cm^2.

Figure 6 shows the AST results for Pt dissolution (6a) and startup/shutdown (6b) for the Pt/HSC catalyst with D2020 and HOPI. The Pt dissolution AST indicates a much faster initial decrease in roughness factor with D2020 versus HOPI. The startup/shutdown AST results show a similar percent loss of roughness factor for D2020 and HOPI when the degradation mechanism is related to the corrosion of the carbon support. These findings

are similar to the Pt/LSC results (see Figure 2). However, the slower initial degradation with HOPI is more pronounced with the Pt/HSC catalyst.

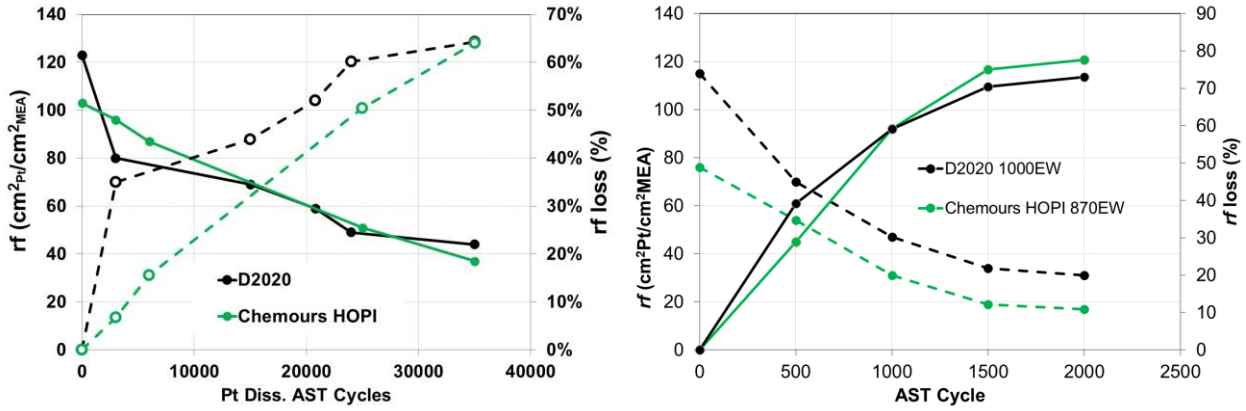

a. b.

Figure 6. Roughness factor loss results for the a) Pt dissolution AST and the b) startup/shutdown AST.

Figure 7 shows the results for the Ballard model forecasting of MEA lifetime using an aggressive drive cycles with inputs from the ASTs for Pt/HSC and the performance modeling. The aggressive drive cycle does not include voltage control for preventing degradation and performance losses for components beside the cathode were not included in order to isolate the impact of the HOPI on cathode lifetime. Figure 7a shows the percent loss of Pt surface area (EPSA) versus operating hours. Those projections show a much more rapid loss of Pt surface area over the first 5000 hours with the D2020 ionomer.

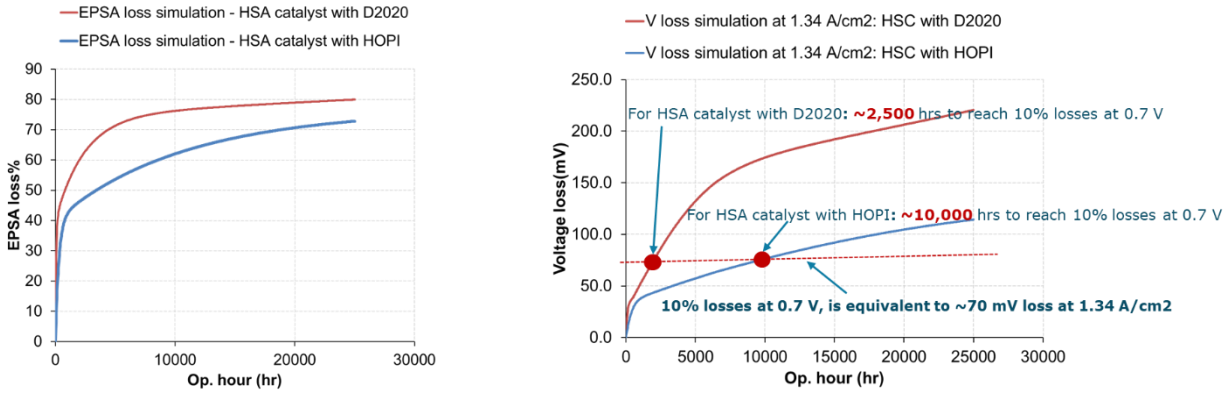

a. b.

Figure 7. Forecasted values versus operating hours for D2020 and HOPI cathodes under an aggressive drive-cycle. a) Pt surface area loss and b) voltage loss at 1.34 A/cm^2.

Figure 7b shows the voltage loss at 1.34 A/cm^2 over a 25,000 hour lifetime using Ballard lifetime forecasting model for an aggressive driving cycle. Using a metric of ~70 mV loss at 1.34 A/cm^2 as an equivalent metric to the 10% power density loss at 0.7 V, an operating lifetime was determined for both D2020 and HOPI cathodes. The D2020 electrode reached the 70 mV loss after approximately 2,500 hours. In contrast, the HOPI reached this criteria after 10,000 hours. After 25,000 hours, the voltage loss at 1.34 A/cm^2 is estimated to be ~120 mV for HOPI versus ~220 mV for D2020. Overhaul, this reflects a >4X increase in lifetime.

13 Cathode Catalyst Layer Cracking Mitigation (Task 3)

The team explored several approaches to reducing cracking in cathodes made with HOPI ionomer. CMU evaluated the effect of ionomer type on the CL film quality by casting CLs with D2020 and HOPI. In addition, the impact of the surrounding air environment was evaluated by casting films under ambient air conditions with a relative humidity of approximately 50% while the second set was performed with applied dry nitrogen flow conditions, resulting in lower local relative humidity of approximately 30%. All catalyst ink mixtures contained the Pt/Vu catalyst, a solvent ratio (nPA:water) of 2.3:1, and an ionomer to carbon (I/C) of 0.9. The solids weight percentage was held constant at 10%, comprising solid ionomer, Pt, and carbon. The CLs were fabricated following the procedure outlined in Section 2.2 and the Pt loadings were determined to be 0.10±0.02 mg_{Pt}/cm^2 through gravimetric analysis.

As Figure 1a shows, under ambient air conditions, the D2020 sample exhibited minimal cracking (less than 0.3% of the total area), while the HOPI sample displayed cracks covering approximately 4% of the area. The crack density was significantly reduced for both ionomers when the RH of the coating and drying environment was lowered. The distribution of individual crack area is shown in Figure 1b. Under both ambient air and a dry N_2 flow environment, the D2020 samples had smaller cracks than the HOPI samples. Figure 1c presents the distribution of the effective diameter of individual cracks for each ionomer under different RH conditions.

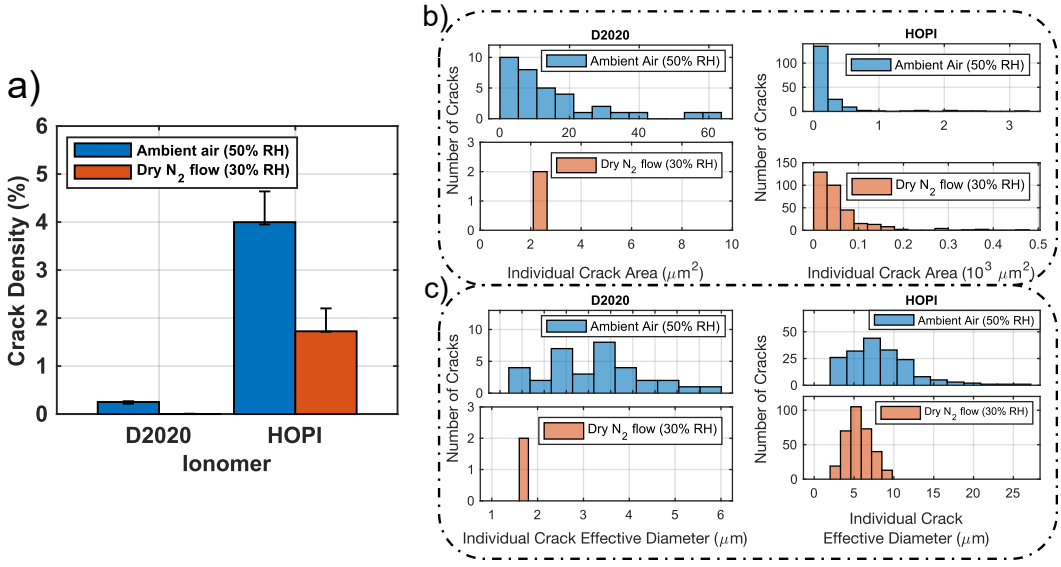

Figure 1: Impact of ionomer-type and relative humidity of coating and drying environment on crack properties. (a) Crack density, (b) individual crack area, and (c) individual crack effective diameter.

Figure 2a shows the crack density of HOPI CLs as a function of the solids weight percent, which varied between 10, 12.5, and 15 wt %. The CL films were prepared using the Pt/Vu catalyst, with a constant nPA:water ratio of 2.3:1 and an ionomer to carbon ratio of 0.9. The results show that the film produced with 10 wt % solids exhibited the lowest crack density. This observation is further confirmed by Figures 5b and c, demonstrating that the decrease in solids weight percent resulted in smaller and narrower cracks.

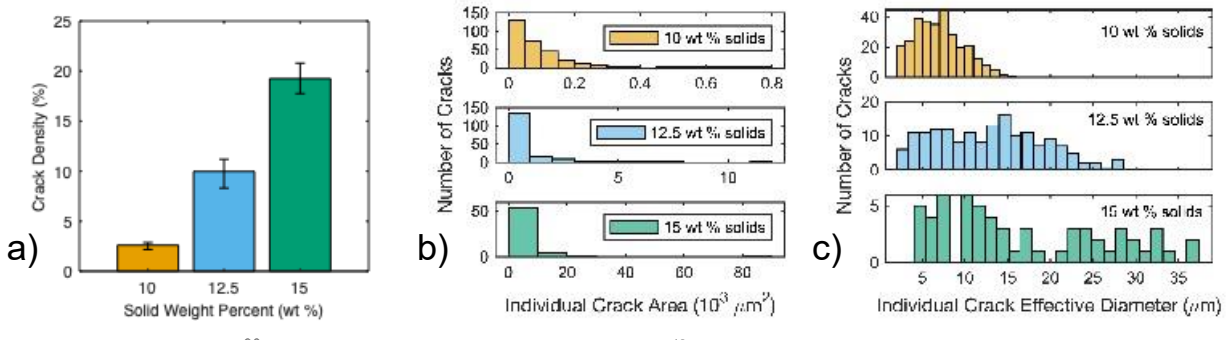

Figure 2: Static and transient analysis of crack formation with various solids weight percentages. (a) Overall crack density, (b) individual crack area, (c) individual crack effective diameter.

Building on the previous study that found the lowest crack density with 10 wt % solids, we conducted a solvent ratio study with three different ratios of nPA to water mass (1:1, 2.3:1, and 5:1). The samples were prepared using HOPI with the Pt/Vu catalyst, and a constant ionomer-to-carbon ratio of 0.9. The results in Figure 3a indicate that the film with a higher nPA content had the lowest crack density. The same trend was also observed in the distribution of individual crack area and the effective diameter of individual cracks, as shown in Figures 3b and c, respectively. The findings suggest that increasing the nPA content leads to smaller and narrower cracks, which, in turn, contributes to a decrease in overall crack density. This outcome is consistent with the conclusions from the previous studies.

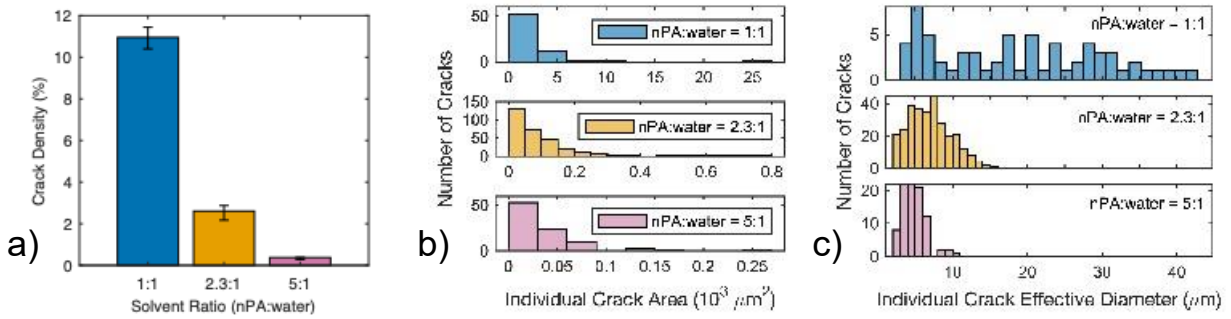

Figure 3: Static and transient analysis of crack formation with various solvent ratios. (a) Overall crack density, (b) individual crack area, (c) individual crack effective diameter.

14 PFSA-HOPI Blended Ionomer Cathodes (Task 3)

This section covers the CMU work on using a combination of HOPI and PFSA ionomer in a blended-ionomer cathode. CMU performed SAXS analysis of HOPI, D2020 PFSA, and PFSA/HOPI ionomer dispersions in CMU's SAXS facility. Studies were performed to determine the degree of ionomer agglomerate mixing and agglomerate size. The CMU team also evaluated the impact of ultrasonication on the degree of ionomer mixing in the agglomerates and the impact of the solvent's alcohol ratio. Figure 1 shows the results for fitting agglomerate radius. Pure HOPI shows a smaller length scale than D2020 PFSA and more sensitivity to the water-to-alcohol ratio (Figure 1a). As Figure 1b shows, the length scale of blend agglomerates scales proportionally with the fraction of D2020 PFSA in the PFSA/HOPI blend and is relatively insensitive to horn ultrasonication. This suggests that the PFSA and HOPI remain as separate populations in the ionomer blend dispersion.

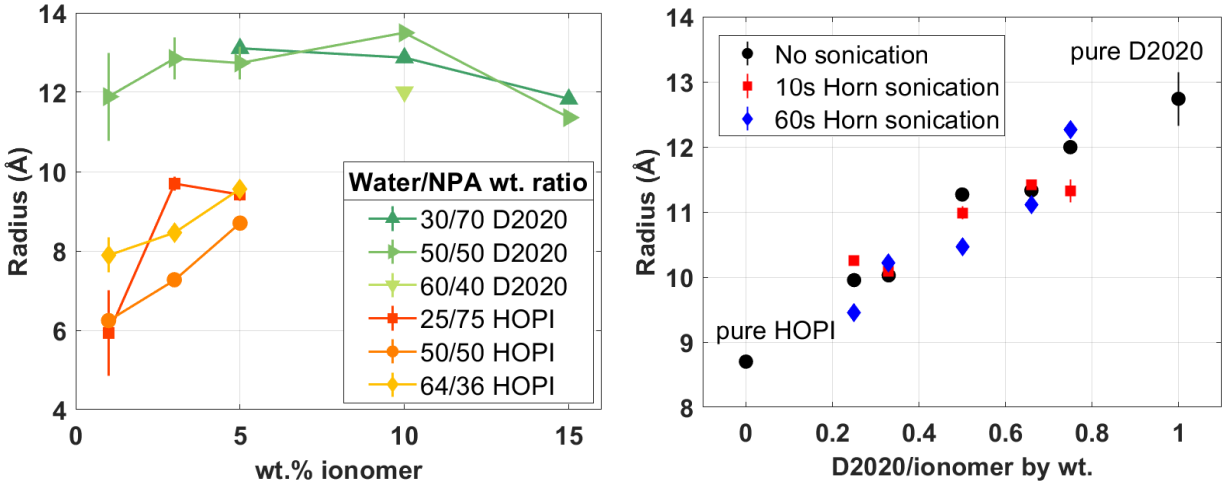

a) b)

Figure 1: a) Effect of water to alcohol solvent ratio on ionomer dispersion length scales for PFSA D2020 and HOPI. b) Ionomer agglomerate length scales as a function of PFSA D2020 weight percent in a PFSA/HOPI blend with varying levels of horn ultrasonication. All mixtures have a total wt.% of 5%.

CMU fabricated and tested CCMs with blended PFSA-HOPI cathodes. Traditional PFSA is employed for its binding and proton conduction properties. This results in superior dispersion, high-quality electrode coatings with minimal cracking, and enhanced mechanical strength for binding. Figure 2 shows the results for various HOPI percentages and their final film crack densities. By optimizing the blend ratio of HOPI and Nafion D2020 on the catalyst surface, significant advancements were observed, notably a more than 50% reduction in cracking with a 25% HOPI concentration (Figure 2a).

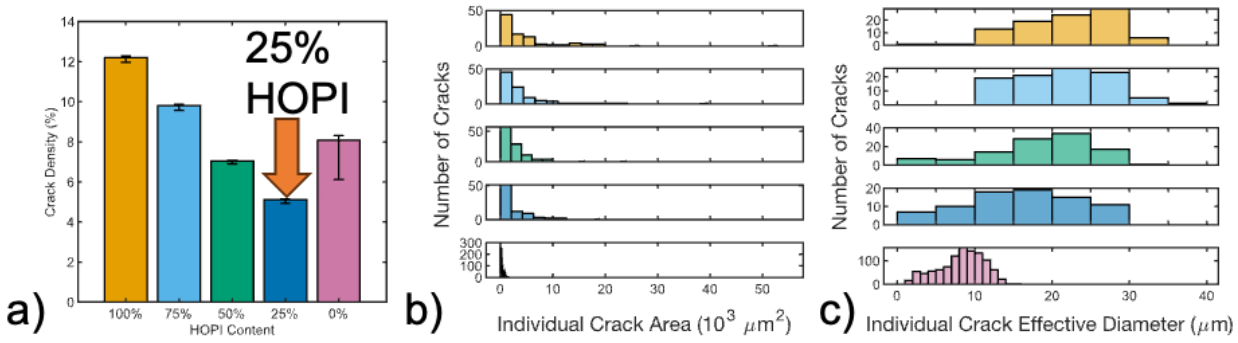

Figure 2: Impact of HOPI and D2020 mixing ratio on crack properties: a. crack density, b. individual crack area, and c. individual crack effective diameter.

CMU has focused on testing the fuel cell performance of blended ionomer, 25 wt. % HOPI with 75 wt. % Nafion D2020, with Pt/HSC catalyst. The study aimed to investigate the impact of mixed ionomer, compared to a single ionomer type in the fuel cell cathode catalyst layer, as well as the sequence of ionomers being added during the ink fabrication. All inks were fabricated with TKK TEC10E50E (47 wt. % Pt on high surface area carbon), 10 wt. % solids, nPA:water = 2.3:1, I/C = 0.6, and HOPI:D2020 = 25:75. Figures 2 and 3 show the fuel cell performance of blended ionomer with adding HOPI to the catalyst ink first, adding D2020 first, and mixing HOPI with D2020 first before adding to the catalyst ink mixture. All results are compared to the 100% HOPI and 100% D2020 data reported in the previous quarterly report.

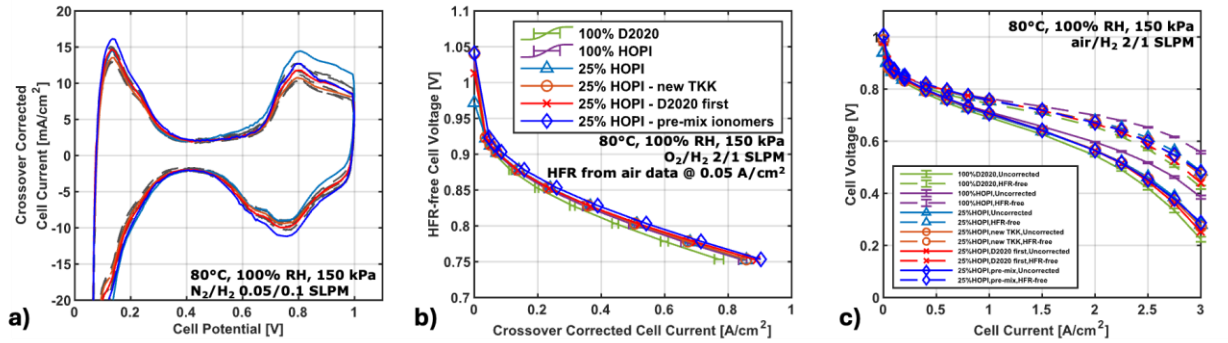

Figure 2: Characterization of blended ionomer-based CLs with total Pt loadings of 0.30 ± 0.01 mg_{Pt}/cm^2. a. CV, b. O_2/H_2 polarization curve, and c. air/H_2 polarization curve.

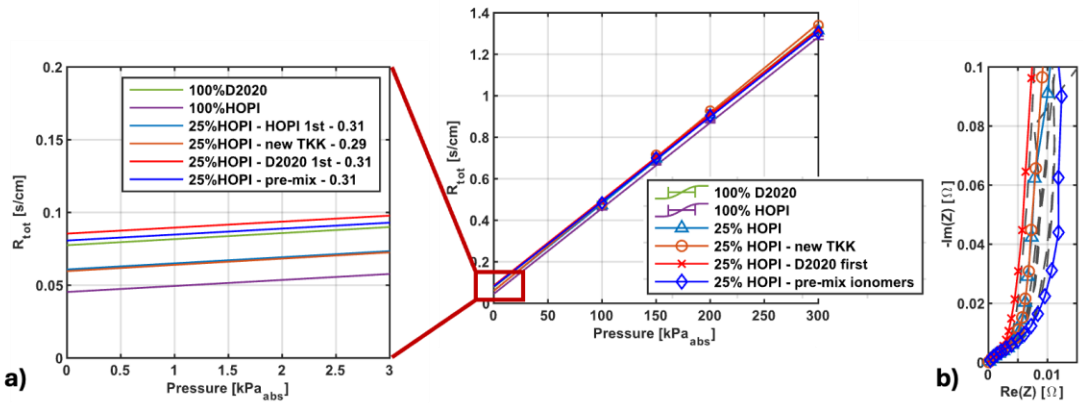

Figure 3: Characterization of blended ionomer-based CLs with total Pt loadings of 0.30 ± 0.01 mg_{Pt}/cm^2. a. oxygen transport analysis at 75% RH, and b. complex-plane impedance.

Table 1 summarizes the performance of all samples, where, compared to 100% D2020, the blended ionomer with adding HOPI first shows a 27% increase in specific activity and a 19% increase in mass activity. When compared to 100% HOPI, the same sample shows an 8% increase in specific activity and a 6% increase in mass activity. The blended ionomer with adding D2020 first shows a 14% increase in specific activity and a 16% increase in mass activity when compared to 100% D2020, and similar performance when compared to 100% HOPI. When ionomers are pre-mixed first, the fuel cell performance is similar to the blended ionomer with adding HOPI first.

Table 1: Summary of fuel cell performance of blended ionomer-based CLs.

Ionomer	Pt Loading [mg_{Pt}/cm^2]	ECSA [m^2/g_{Pt}]	RF	MA [A/mg_{pt}]	SA [A/m^2_{Pt}]	R_{NF} [s/cm]	R_{CL} [$m\Omega$-cm^2]	H_2 Crossover [mA]
100% D2020	0.29	56.6	164	0.198	3.5	0.132	65	28
100% HOPI	0.30	54.8	165	0.223	4.1	0.101	51	22
25% HOPI (HOPI first)	0.31	52.7	163	0.232	4.4	0.117	49	35
25% HOPI (HOPI first, new TKK)	0.29	53.5	155	0.240	4.5	0.116	49	13
25% HOPI (D2020 first, new TKK)	0.31	56.6	175	0.229	4.0	0.140	44	22
25% HOPI (pre-mix, new TKK)	0.31	63.4	196	0.276	4.3	0.136	83	28

Furthermore, CCLs with blended ionomer when adding HOPI to the ink first also show a decrease in electrode H^+ resistance (25% lower than 100% D2020 and 4% lower than 100% HOPI) and non-Fickian oxygen transport resistance (12% lower than 100% D2020). The results show that mixing a small amount of HOPI with D2020 has a positive impact on the fuel cell performance, and the ionomer addition sequence has an impact on the testing results: adding HOPI first in the catalyst ink mixture yields the best fuel cell performance.

15 Project Outcomes

15.1 Special Recognitions and Awards

Project included in 2020 U.S. DRIVE Highlights of Technical Accomplishments report.

15.2 PhD Dissertations

Braaten, Jonathan P. (2021). *Understanding catalyst layer morphologies and degradation and their impact on critical oxygen transport in PEMFC cathodes*, Ph.D. Dissertation, Carnegie Mellon University. (Order No. 28410986). *ProQuest Dissertations and Theses,* , 126. Retrieved from https://www.proquest.com/dissertations-theses/understanding-catalyst-layer-morphologies/docview/2518757230/se-2?accountid=9902

Liu, Jiawei (2024). *Engineering Enhanced Catalyst Layers Through High Oxygen Permeability Ionomers: A Systematic Study of Material Properties, Processing Parameters, and Performance in PEMFCs*, Ph.D. Dissertation, Carnegie Mellon University.

15.3 Peer Reviewed Publications

Braaten, J. P., Kariuki, N. N., Myers, D. J., Blackburn, S., Brown, G., Park, A., & Litster, S. (2022). Integration of a high oxygen permeability ionomer into polymer electrolyte membrane fuel cell cathodes for high efficiency and power density. Journal of Power Sources, 629, 236032. https://doi.org/10.1016/J.JPOWSOUR.2021.230821

Liu, J, Braaten, J. P., & Litster, S. (2025). Impact of catalyst carbon support on the benefits of high oxygen permeability ionomer for proton exchange membrane fuel cells. Journal of Power Sources, 522, 230821. https://doi.org/10.1016/j.jpowsour.2024.236032

15.4 Presentations

S. Litster, “Durable High-Power Density Fuel Cell Cathodes for Heavy-Duty Vehicles,” US Dept. of Energy Annual Merit Review, Virtual, June 9, 2021 (invited).

S. Litster, “The Importance of Polymer Electrolytes in Fuel Cell Electrodes in Meeting Performance and Durability Targets,” AIChE Annual Meeting, Boston, MA, Nov. 11, 2021 (invited).

J. Braaten, J. Liu, Z. White, N. Tiwari, G. Brown, A. Park, D. Paul, Z. Ulissi, S. Litster, “Development of Polymer Electrolyte Fuel Cell (PEFC) Cathodes with High Oxygen Permeability Ionomer (HOPI) for High Performance and Durability,” Fall Meeting of the Electrochemical Society, Virtual, Oct. 13, 2021.

S. Litster, “Durable High-Power Density Fuel Cell Cathodes for Heavy-Duty Vehicles,” DOE Million Mile Fuel Cell Truck (M2FCT) Consortium Semi-annual Meeting, Santa Fe, NM, March 2, 2022 (invited).

S. Litster, “Durable High-Power Density Fuel Cell Cathodes for Heavy-Duty Vehicles,” US Dept. of Energy Annual Merit Review, Virtual, June 8, 2022 (invited).

Shawn Litster, “Advanced Electrode Materials and Architectures to Mitigate the Negative Impacts of Ionomer Binders,” Gordon Research Seminar Keynote, Smithfield, RI, July 23, 2022.

Poster: Next Generation Cathode Catalyst Layer for Heavy Duty Applications Presenter: Devproshad Paul (Ballard Power Systems), Co-Authors: Alan Young (Ballard), Shanna Knights (Ballard), Gerald Brown (Chemours), Andrew Park (Chemours), Shawn Litster (CMU), Gordon Research Conference (GRC), RI, USA, July 24-29, 2022

Poster: Studying Crack Formation in Catalyst Layer Films for Proton Exchange Membrane Fuel Cells, Presenter: Jiawei Liu (CMU), Co-Authors: Shawn Litster (CMU), Gordon Research Conference (GRC), RI, USA, July 24-29, 2022.

S. Litster, “Durable High-Power Density Fuel Cell Cathodes for Heavy-Duty Vehicles,” DOE Million Mile Fuel Cell Truck (M2FCT) Consortium Semi-annual Meeting, Napa, CA, August 30, 2022 (invited).

Jiawei Liu, Jonathan Braaten, Nicholas Tiwari, Xiaoxiao Wang, Scott Blackburn, Gerald Brown, Andrew M Park, Zachary Ulissi, Shawn Litster, “Evaluation of High Oxygen Permeability Ionomer (HOPI) Oxygen Permeability for Proton Exchange Membrane Fuel Cells (PEMFCs),” Fall Meeting of the Electrochemical Society, *Meet. Abstr.* MA2022-02 1514, 2022.

Juan Mesa, Scott Blackburn, Austin Plymill, Gerald Brown, Andrew M Park, Devproshad Paul, Shawn Litster, “Electrode Ionomer Accelerated Stress Test Applied to High Oxygen Permeability Ionomer in Fuel Cells,” Fall Meeting of the Electrochemical Society, *Meet. Abstr.* MA2022-02 1504, 2022.

S. Litster, “Improving Performance and Durability of Polymer Electrolyte Fuel Cell Cathodes with High Oxygen Permeability Ionomer (HOPI),” AIChE Annual Meeting, Phoenix, AZ, November 15, 2022 (invited).

S. Litster, “Durable High-Power Density Fuel Cell Cathodes for Heavy-Duty Vehicles,” DOE Million Mile Fuel Cell Truck (M2FCT) Consortium Semi-annual Meeting, Santa Fe, NM, February 15, 2023 (invited).

S. Litster, “Durable High-Power Density Fuel Cell Cathodes for Heavy-Duty Vehicles,” US Dept. of Energy Annual Merit Review, Washington, DC, June 6, 2023 (invited).

S. Litster, “Durable High-Power Density Fuel Cell Cathodes for Heavy-Duty Vehicles,” DOE Million Mile Fuel Cell Truck (M2FCT) Consortium Semi-annual Meeting, Monterrey, CA, August 22, 2023 (invited).

S. Litster, “Innovations in Proton Exchange Membrane Fuel Cell Cathode Materials and Architectures for High Power Density and Durability,” AIChE Annual Meeting, Orlando, FL, November 8, 2023 (invited).

S. Litster, “Keynote: Advanced Materials Development and Simulation of Polymer Electrolyte Electrolyzers and Fuel Cells for Accelerating Decarbonization,” The 3rd

International Forum on Energy & Informatics, Bali, Indonesia, December 15, 2023 (invited).